

Modeling and simulation of neutron detectors for the transient reactor test
facility

by

Wenkai Fu

B.S., Nanjing Univ. of Aero. and Astro., 2011

M.S., Nanjing Univ. of Aero. and Astro., 2014

AN ABSTRACT OF A DISSERTATION

submitted in partial fulfillment of the
requirements for the degree

DOCTOR OF PHILOSOPHY

Department of Mechanical and Nuclear Engineering
College of Engineering

KANSAS STATE UNIVERSITY
Manhattan, Kansas

2019

Abstract

The Transient REActor Test (TREAT) facility was restarted and will be used to test accident-tolerant fuels to improve nuclear reactor safety. In this work, alternative neutron detectors for use in core and with the hodoscope at the TREAT facility were modeled and simulated using different computational tools to understand the underlying physics.

The Hornyak button scintillation detector used in the original TREAT hodoscope to detect fast neutrons and its variants were evaluated using Geant4 to simulate the coupled nuclear and optical physics. The Hornyak-button model predicted an intrinsic efficiency of 0.35% for mono-directional fission neutrons and strong gamma-induced Cherenkov noise, which agree relatively well with the reported experimental observations.

The proposed variants use silicon photomultipliers to reduce Cherenkov noise and have optimized layered or homogenized scintillation volumes. The layered and homogenized variants with 5-cm length were predicted to achieve neutron-detection efficiencies of 3.3% and 1.3%, respectively, at a signal-to-noise ratio of 100.

Another candidate devices for the hodoscope are the actinide and hydrogenous microstructured semiconductor neutron detectors (MSNDs) evaluated using Geant4 and MCNP. With a sufficient rejection of the gamma noises, the ^{235}U -filled and the hydrogenous MSNDs were predicted to yield neutron-detection efficiencies of 1.2% and 2.5%, respectively, at the length of 2 cm.

The micro-pocket fission detectors (MPFDs) were developed to detect in-core neutrons, and the electron collection process in such devices was evaluated using Garfield++-based computational routine. The high-performance Garfield++ application was developed using the built-in, optimized element-search techniques and a hybrid MPI and OpenMP parallelization scheme. The preliminary results indicated that the averaged deposited energy per fission fragment was 7.15 MeV, and the induced current occurred within 400 ns.

Modeling and simulation of neutron detectors for the transient reactor test
facility

by

Wenkai Fu

B.S., Nanjing Univ. of Aero. and Astro., 2011

M.S., Nanjing Univ. of Aero. and Astro., 2014

A DISSERTATION

submitted in partial fulfillment of the
requirements for the degree

DOCTOR OF PHILOSOPHY

Department of Mechanical and Nuclear Engineering
College of Engineering

KANSAS STATE UNIVERSITY
Manhattan, Kansas

2019

Approved by:

Major Professor
Jeremy A. Roberts

Copyright

© Wenkai Fu 2019.

Abstract

The Transient REActor Test (TREAT) facility was restarted and will be used to test accident-tolerant fuels to improve nuclear reactor safety. In this work, alternative neutron detectors for use in core and with the hodoscope at the TREAT facility were modeled and simulated using different computational tools to understand the underlying physics.

The Hornyak button scintillation detector used in the original TREAT hodoscope to detect fast neutrons and its variants were evaluated using Geant4 to simulate the coupled nuclear and optical physics. The Hornyak-button model predicted an intrinsic efficiency of 0.35% for mono-directional fission neutrons and strong gamma-induced Cherenkov noise, which agree relatively well with the reported experimental observations.

The proposed variants use silicon photomultipliers to reduce Cherenkov noise and have optimized layered or homogenized scintillation volumes. The layered and homogenized variants with 5-cm length were predicted to achieve neutron-detection efficiencies of 3.3% and 1.3%, respectively, at a signal-to-noise ratio of 100.

Another candidate devices for the hodoscope are the actinide and hydrogenous microstructured semiconductor neutron detectors (MSNDs) evaluated using Geant4 and MCNP. With a sufficient rejection of the gamma noises, the ^{235}U -filled and the hydrogenous MSNDs were predicted to yield neutron-detection efficiencies of 1.2% and 2.5%, respectively, at the length of 2 cm.

The micro-pocket fission detectors (MPFDs) were developed to detect in-core neutrons, and the electron collection process in such devices was evaluated using Garfield++-based computational routine. The high-performance Garfield++ application was developed using the built-in, optimized element-search techniques and a hybrid MPI and OpenMP parallelization scheme. The preliminary results indicated that the averaged deposited energy per fission fragment was 7.15 MeV, and the induced current occurred within 400 ns.

Table of Contents

List of Figures	xi
List of Tables	xvi
Acknowledgements	xviii
1 Introduction and Background	1
1.1 Motivation	1
1.2 Transient Reactor Test Facility	2
1.2.1 Core	4
1.2.2 Irradiation Experiment Vehicle (IEV)	5
1.2.3 Operation Modes	7
1.2.4 Pulse Narrowing	9
1.2.5 In-Core Neutron Detectors	11
1.2.6 Reactivity and Transient Control Mechanism	13
1.2.7 Hodoscope	14
1.2.8 Hodoscope Detectors	16
1.3 Modeling of Novel Neutron Detectors for TREAT	17
1.3.1 ZnS(Ag)-Based Scintillation Detectors	18
1.3.2 Fast-Sensitive MSNDs	19
1.3.3 Micro-Pocket Fission Detectors	19
1.4 Organization of the Dissertation	20
2 Neutron Detection Techniques	21

2.1	Converting Reactions	21
2.1.1	Thermal Absorptive Reactions	22
2.1.2	Proton-Recoil Reaction	22
2.1.3	Fission Reactions	23
2.2	Signal-Forming Mechanisms	23
2.2.1	Gas-Filled Detectors	24
2.2.2	Inorganic Scintillation Detectors	28
2.2.3	Semiconductor Detectors	33
2.3	Summary	40
3	Monte Carlo Simulation	41
3.1	Monte Carlo Basis	41
3.2	Flow of Monte Carlo Simulation	43
3.3	Overview of Geant4	44
3.4	Code Structure of Geant4 Application	45
3.4.1	Detector Construction	45
3.4.2	Reference Physics List	47
3.4.3	Action Initialization	48
3.5	Geant4 Optical Physics	48
3.5.1	Optical Absorption Process	49
3.5.2	Optical Boundary Process	51
3.5.3	Scintillation Process	55
3.6	Summary	56
4	Hornyak Button Neutron Detector	57
4.1	Description of the Hornyak Button	57
4.2	Hodoscope Radiation Environment	59
4.3	Hornyak Button Model	61

4.3.1	ZnS(Ag) Grain Randomization	61
4.3.2	Optical Surface Settings	62
4.3.3	Source Planes	63
4.4	Physical Models and Approximations	64
4.5	Tally Method	65
4.6	Detector Response and Efficiency	65
4.7	Results	66
4.8	Summary	67
5	Hornyak Button Variants	69
5.1	Design of the Variants	69
5.2	Layered Detector Results	72
5.2.1	Thickness Optimization	72
5.2.2	Pulse Height Distributions	72
5.2.3	Length Evaluation	74
5.2.4	Gamma Rejection	75
5.3	Homogenized Detector Results	75
5.3.1	ZnS(Ag) Fraction Optimization	75
5.3.2	Pulse Height Distributions	76
5.3.3	Length Evaluation	76
5.3.4	Gamma Rejection	78
5.4	Summary	78
6	Fast-Sensitive MSNDs	80
6.1	Description of the MSND	80
6.2	Cross Section Comparison of the Converters	82
6.3	Modeling Details	83
6.3.1	Neutron Data Library	84

6.3.2	MSND Models for NEPHDs	84
6.3.3	MSND Model for Gamma Event PHDs	84
6.3.4	Physics Settings	86
6.3.5	Source Terms	88
6.3.6	Tally Methods	89
6.4	Assumptions of the Modeling	89
6.5	Evaluation and Results	90
6.5.1	Effects of Parameters	90
6.5.2	Actinide MSNDs	91
6.5.3	Hydrogenous MSNDs	95
6.6	Summary	99
7	Micro-Pocket Fission Detectors	101
7.1	MPFD Physics	101
7.2	Computational Scheme	102
7.3	Gmsh	104
7.3.1	Running Modes	104
7.3.2	Geometry Construction	105
7.3.3	Geometry Meshing	106
7.3.4	MPFD Gmsh Model	107
7.4	Elmer	107
7.4.1	ElmerGrid	108
7.4.2	ElmerSolver	109
7.5	Garfield++	109
7.5.1	MediumMagboltz Class	110
7.5.2	Component Classes	112
7.5.3	Track Classes	114
7.5.4	Electron Transport Classes	117

7.5.5	Parallelization Scheme	119
7.6	MPFD Results	122
7.7	Summary	125
8	Conclusion and Future Work	128
8.1	Conclusions	128
8.1.1	Hornyak Button	128
8.1.2	Hornyak Button Variants	129
8.1.3	Fast-Sensitive MSNDs	129
8.1.4	MPFD	130
8.2	Future Work	131
8.2.1	Testing of the Hodoscope Detectors	131
8.2.2	Expanding the MPFD Modeling	132
	Bibliography	133
A	MCNP and Geant4 Inputs	143
A.1	MCNP Input	144
A.1.1	Surface Cards	144
A.1.2	Cell Cards	144
A.1.3	Data Cards	144
A.2	Geant4 Input	147
A.2.1	Main Function	147
A.2.2	Detector Construction	148
A.2.3	Action Initialization	149
B	ElmerSolver Input	159
C	Electron Tracking in Parallel Plate	162

List of Figures

1.1	Key components of TREAT, from Ref. [1].	3
1.2	Top view of the TREAT core, permanent reflector, and biological shielding, from Ref. [1].	5
1.3	Schematic of the Mark-III sodium loop with three fuel pins loaded, after Ref. [2]. The loop has a capacity of 7 fuel pins.	7
1.4	FWHM of the TREAT pulse and maximum fuel temperature varies with reactivity insertions, after Ref. [3]. Results under total peaking factors 1.82 and 1.6 are shown.	10
1.5	The prompt SPNDs used in TREAT, after Ref. [4].	11
1.6	Schematic of the force directions on the electrons introduced by the space-charge electric field in the SPNDs.	13
1.7	Current layout of the TREAT control rods, after Ref. [3]. T is the transient rods. C is the compensation rod. S is the control/shutdown rod. H represents the slotted hodoscope assembly. TH stands for the test hole.	15
1.8	Schematic of the TREAT hodoscope, from Ref. [5].	15
1.9	Schematic of the Hornyak button fast neutron detector, from Ref. [6].	17
2.1	Kinematics of neutron-proton collision in the laboratory system.	23
2.2	The collected charges vary with applied voltage in the gas-filled detectors irradiated by α , β , and γ particles, after Ref. [7].	25
2.3	Intrinsic and extrinsic scintillation mechanisms, after Ref. [8]. Abbreviations: E_c , conduction band edge; E_v , valence band edge; E_{t0} , activator ground state; E_{t1} and E_{t2} , activator excited states.	30

2.4	A scintillation detector consists of coupled scintillator and PMT, after Ref. [8].	32
2.5	Comparison of SiPM PDEs to quantum efficient of PMTs, after Ref. [9].	33
2.6	Semiconductor doping effects.	36
2.7	Distribution of the electric field in the depletion region of the <i>pn</i> junction, after Ref. [10].	37
3.1	Basic structure of a Geant4 simulation (solid boxes), compared to MCNP input cards (dotted boxes).	46
3.2	An optical photon is reflected or refracted at a polished boundary.	54
3.3	The Lambertian reflection.	54
4.1	Schematic of the Hornyak button as used at TREAT (after [Ref. 11]).	58
4.2	Spectra of the ^{235}U , thermal fission neutrons and gamma rays.	60
4.3	The developed Hornyak button model in Geant4.	63
4.4	One neutron per event was generated uniformly in source plane 1. To evaluate the gamma-induced scintillation noise, 10 gamma rays per event were generated uniformly in source plane 1. To evaluate the gamma-induced Cherenkov noise and the combined Cherenkov-scintillation noise, 69 gamma rays per event were born uniformly in source plane 2.	64
4.5	Results of the original Hornyak button model.	68
5.1	Geometric illustrations of the two new detectors. The cross-sectional area of both scintillation volumes is a rectangle with size 2.51×8.89 mm, which is consistent with the designed channel slit in the TREAT hodoscope.	70
5.2	Performance of the 5-cm long, optimized layered detector.	73
5.3	Neutron-detection efficiency of the layered detector as a function of the detector length. The thicknesses of PMMA and ZnS(Ag) layers were set to 0.18 mm and 12 μm , respectively.	74
5.4	A comparison of two new detectors' gamma-rejection capabilities.	75

5.5	Impacts of the ZnS(Ag) mass ratio in the scintillation volume on neutron-detection efficiency.	76
5.6	Performance of the 5-cm long, optimized homogenized detector.	77
5.7	Homogenized detector's performance as a function of detector length.	78
6.1	Basic design of an MSND, where T is the trench width, and W is the wall width.	81
6.2	Microscopic cross sections of the target reactions [12] and the ^{235}U Watt fission spectrum by thermal neutron.	82
6.3	The developed MSND model for NEPHDs in Geant4. The trench (T) and wall (W) widths were 0.1 cm for illustration.	85
6.4	The developed MSND model for NEPHDs in MCNP6. The trench (T) and wall (W) widths were 0.1 cm for illustration.	86
6.5	The etched silicon region was modeled to compute the NEPHDs in Geant4 and MCNP6. To evaluate the H-MSNDs' responses to the gamma rays in Geant4, the bulk silicon region and the electronic board were added. The neutron and the gamma source generation planes were set correspondingly.	87
6.6	The H-MSND model to calculate the gamma event PHDs in Geant4.	87
6.7	The Geant4-computed neutron-detection efficiencies of the 2-cm long ^{235}U -filled MSNDs with different trench and wall widths at the 5-MeV LLD.	91
6.8	The Geant4-predicted distributions of the energy deposition in silicon by fission fragments of the 2-cm long actinide MSNDs with 20- μm trench and 10- μm wall widths.	93
6.9	Extreme paths of fission fragments in the actinide MSND.	93
6.10	The Geant4-computed intrinsic neutron detection efficiencies of the actinide MSND arrays. The MSNDs had 20 μm trench and 10 μm wall widths. The LLDs were set to 5 MeV.	94

6.11	The Geant4- and MCNP6-computed intrinsic neutron detection efficiencies of the 2-cm long H-MSNDs with different trench and wall widths. A 300-keV LLD was set.	96
6.12	The Geant4- and MCNP6-computed NEPHDs of the 2-cm long H-MSND with 20- μ m trench, 10- μ m wall widths.	97
6.13	The Geant4- and MCNP6-computed neutron detection efficiencies of the H-MSNDs with different lengths. The 300-keV LLD was set. The H-MSNDs were with 20- μ m trench and 10- μ m wall widths.	98
6.14	The Geant4-computed neutron and gamma event PHDs of the 2-cm long H-MSND with 60- μ m trench and 40- μ m wall widths.	99
6.15	The Geant4-computed neutron detection efficiencies of the H-MSNDs vary with length. The H-MSNDs had the optimized 60- μ m trench and 40- μ m wall widths. The LLDs were set to achieve an S/N ratio of 100 based on the gamma event PHDs.	100
7.1	Schematic of the MPFD developed for Idaho National Laboratory. Dimensions are in mm.	103
7.2	The computational scheme to evaluate MPFDs.	104
7.3	The meshed MPFD geometry using Gmsh.	108
7.4	The computed electric field (V/cm) inside the gas volume.	110
7.5	The computed electric weighting field (V/cm) inside the gas volume.	110
7.6	Code structure of a Garfield++ application.	111
7.7	The computed induced current using one and 10 \times 10 cores.	122
7.8	Induced currents by three fission fragments.	123
7.9	The averaged induced currents by two thousands fission fragments.	124
7.10	Correlated total charge and time to collect 95% of the charge.	125
7.11	Distribution of the time to collect 95% of the total charge.	125
7.12	Distribution of the deposited energy to create electron clusters.	126

7.13	Distribution of the collected charge.	126
A.1	An example problem was modeled in Geant4 and MCNP to compare the inputs. All dimensions are in cm.	143
A.2	MCNP input of the simple model.	145
C.1	Drift line and induced current of one electron simulated by the Monte Carlo integration method. Diffusion was not simulated.	163
C.2	Trajectories of five electrons (a) and induced current of 50 electrons (b) simulated by the Monte Carlo integration method taking into consideration of the diffusion process. Using the microscopic tracking method, the trajectories of five electrons (c) and induced current by 50 electrons (d) are similar with the Monte Carlo integration results.	164

List of Tables

1.1	Core design and components of TREAT, after Ref. [13].	4
1.2	Features of the Mark-III sodium loop, after Ref. [14].	7
1.3	Operating characteristics of TREAT, after Ref. [13]. The nominal pulse duration is the full width at half maximum (FWHM).	8
1.4	Details of the SPNDs used in TREAT, after [4].	12
1.5	Reactivity and transient control mechanism characteristics of TREAT, after Ref. [13, 15]. Ref. [13] stats the number of transient rods is one. Ref. [15] reports the number is eight, which is listed here.	14
2.1	Comparison of three thermal neutron absorptive reactions, after Ref. [7]. . .	22
3.1	Summary of the optical properties read by each optical process. Properties with superscript c are constants, and others are functions of optical photo or deposited energy. Data are extracted from the Geant4 source code.	50
3.2	Optical surface finishes in Geant4. Data are extracted from the Geant4 source code.	52
5.1	The neutron-detection efficiencies (%) of a 5-cm long, layered detector under different layer thicknesses.	72
6.1	Comparison of the converter cross sections.	83
6.2	Total deposited energies (MeV) in the trenches per neutron computed by Geant4 and MCNP6 and their differences (relative to MCNP6).	95
6.3	Alpha decays of the 2-cm long actinide MSNDs with 20- μ m trench and 10- μ m wall widths. Data from Ref. [16].	95

6.4	The trench and wall widths of the 2-cm long H-MSNDs that yielded neutron detection efficiencies (in percent) above 2% at the LLD settings that achieved S/N ratio of 100. The LLD settings in MeV are shown in the parentheses. . . .	98
7.1	Field map component classes to read results from different softwares.	112

Acknowledgments

I would first express my sincere gratitude to my advisor, Prof. Jeremy Roberts, for giving me the opportunity to work in his CORPS group and guiding me exploring the scientific-computing world. I learn a lot from his advising, professional skills, enthusiasm, energy, and efficient way to solve problems, which is an invaluable treasure in my life. Especially, I appreciate his explanations when the words are beyond my vocabulary.

I would thank Prof. Douglas McGregor, who is an expert in radiation detection and the main collaborator of the thesis work. I appreciate the opportunity he gave to let me participate the projects and the suggestions to help moving forward. I am looking forward to his state-of-the-art book (co-authored with Prof. Shultis) to be published.

I would thank Prof. Shultis for his abundant experiences and interpolation on what does a Ph.D degree mean, Prof. Dunn for the high-quality lectures and leading the department, Prof. Bindra for the recommendations and the opportunity to calibrate the RTD probes in his laboratory, Prof. Bahadori for the useful comments on giving a talk, and Prof. McNeil for the connections to other institutions. In addition, Prof. Weaver and Prof. Andresen have my appreciations for serving as an out-department committee member and chair, respectively.

I would thank soon-to-be-Dr. Richard Reed for helping me adapt to local life, sharing new softwares and code features, and the daily jokes. He is patient and always ready to answer questions. I enjoy the time spent with other CORPS group members, who are Rabab Elzohery, John Boyington, Leidong Xu, and Ye Cheng, and the S.M.A.R.T. laboratory people, who are Priyarshini Ghosh, Dan Nichols, Dr. Fronk, Dr. Reichenberger, and Dr. Harrison.

I would thank the friends met at K-State, who are Yue Yuan, the Xu's family, and the Hsiao's family for the hot-pot parties and many happy events.

I express my full love to my parents and my sister's family.

I would also like to acknowledge that the presented work is supported in part by the U.S. Department of Energy, Office of Nuclear Energy under Award Number DE-NE0008305.

Chapter 1

Introduction and Background

1.1 Motivation

In December 2010, the United States Department of Energy (DOE) declared a need for a domestic transient testing capability to develop nuclear fuels [17]. Such a capability became more crucial after the Fukushima Daiichi nuclear accident in March 2011. After the accident, development of accident-tolerant fuels (ATFs) used in light water reactors (LWRs) was of high interest [18]. To reintroduce a domestic, transient-testing capability, two reasonable alternatives were reviewed and analyzed: to restart the Transient Reactor Test Facility (TREAT) reactor at Idaho National Laboratory (INL) and to modify the Annular Core Research Reactor (ACRR) at Sandia National Laboratories (SNL) [17]. After evaluation, it was decided to restart the TREAT facility in February 2014 [19].

Transient testing involves placing nuclear fuel or material into the core of a nuclear reactor and subjecting it to short bursts of intense, high-power radiation to simulate accident conditions [1]. Fuel meltdowns, metal-water reactions, thermal interaction between overheated fuel and coolant, and the transient behavior of ceramic fuel for high temperature systems can be investigated [20]. In particular, transient testing of nuclear fuels is needed to improve current nuclear-power plant performance and sustainability, to make next generation reactors more affordable, to develop nuclear fuels that are easier to recycle, and to

20 improve the proliferation resistance of fuel designs [1].

21 TREAT is one of the six nuclear transient reactor facilities worldwide, and the others
22 are the Annular Core Research Reactor (ACRR, USA), the Nuclear Safety Research Reactor
23 (NSRR, Japan), the CABRI (France), the Impulse Graphite Reactor (IGR, Kazakhstan),
24 and the Bystry Impulsny Graphitovy Reaktor (BIGR, Russia) [13]¹. Among these facili-
25 ties, TREAT may be the most versatile [1]. Its extraordinary capability for nuclear-heated
26 transient testing comes from the brilliantly basic design and decades of incremental facility
27 upgrades. TREAT’s wide transient power range, irradiation experiment vehicles (IEVs) that
28 simulate specimen boundary conditions, in-situ instrumentation, and post-transient exami-
29 nation facilities produce a full-capability package able to address data needs for practically
30 any reactor type or accident category [3]. Upon resumption of operations, TREAT can con-
31 tribute to reactor safety by: 1) providing basic data to predict the safety margin of fuel
32 designs and the severity of potential accidents, 2) serving as a proving ground for fuel con-
33 cepts designed to reduce or prevent consequent hazards, and 3) providing nondestructive
34 test data via neutron radiography of fuel samples irradiated in other test reactors [21].

35 1.2 Transient Reactor Test Facility

36 TREAT is an air-cooled, thermal, heterogenous research reactor designed to evaluate the
37 performance of nuclear fuels and materials under conditions simulating overpower and under-
38 cooling situations [13]. It was designed by the Argonne National Laboratory and has been
39 operated from February 1959 to April 1994 at INL, after which it was in a standby shutdown.
40 During this operating period, TREAT was mainly used to test fast reactor fuels [13].

41 The key components of TREAT are shown in Fig. 1.1, which mainly consist of the core,
42 the hodoscope, and the neutron radiography facility. The hodoscope and the neutron radio-
43 graphy facility connect to two slots opened by penetrating the shield wall and the graphite
44 reflector, respectively. The hodoscope slot bridges the in-core channel created by the assem-
45 blies whose fuel region is replaced by the empty zircaloy frame [3]. The hodoscope is used to

¹Ref. [1] states there are four transient facilities, which exclude the ACRR and the BIGR.

46 monitor the specimen's behavior, e.g., melting or vaporization, during transient experiment.
47 The hodoscope collimates and detects fission neutrons emitted by the fuel specimen. The
48 response of the detectors provides time and spatial resolution of fuel motion during transients
49 and in-place measurement of fuel distribution before and after an experiment. The neutron
50 radiography facility is used during steady state operation and can examine specimens up to
51 15 feet in length [1]. During a neutron radiography experiment, optical and gamma camera
52 systems can be used to record the reactive mechanisms [1].

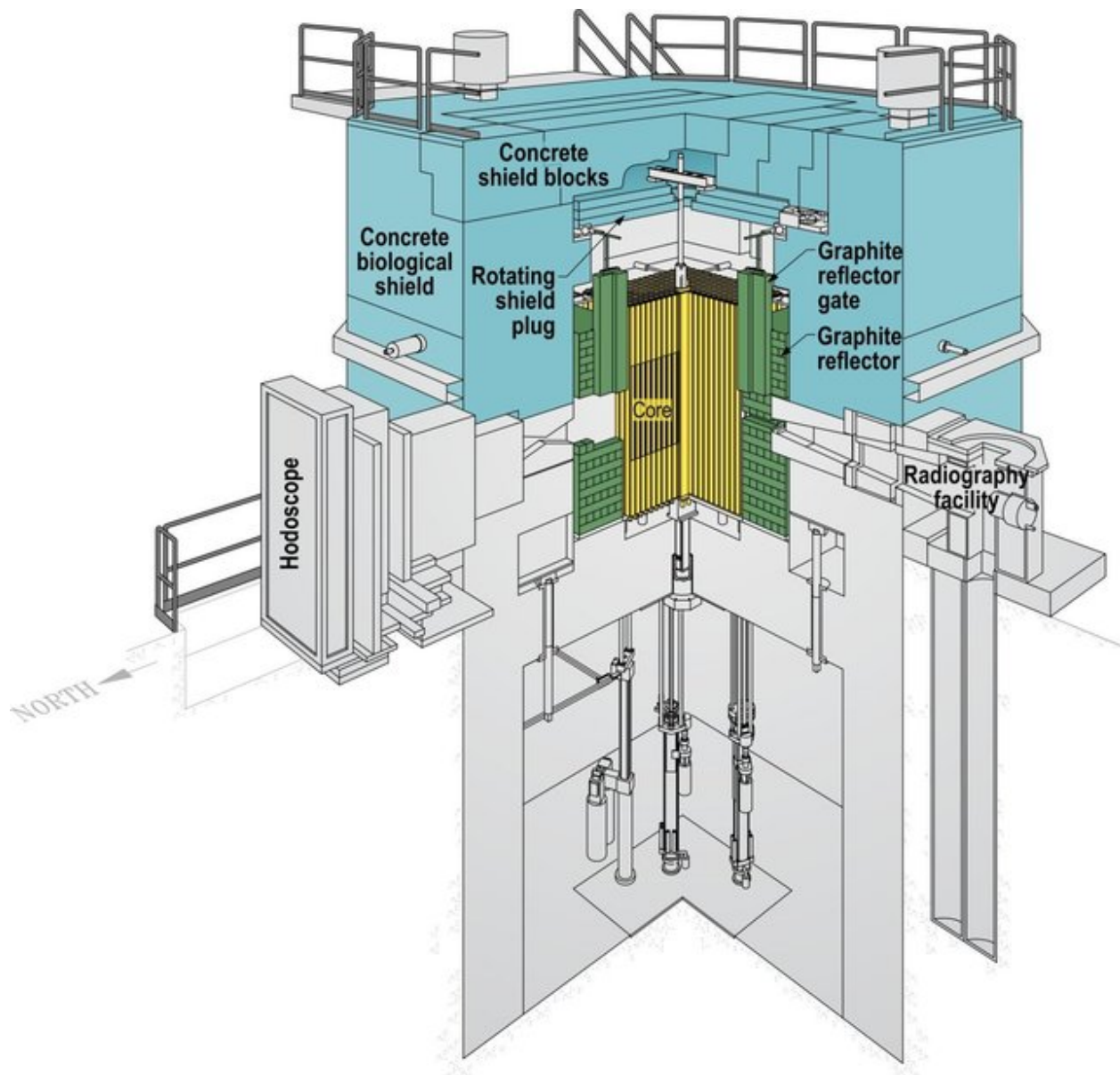


Figure 1.1: Key components of TREAT, from Ref. [1].

53 **1.2.1 Core**

54 Shown in Fig. 1.2 is the top view of the TREAT core, reflector, and biological shielding.
 55 Summarized in Table 1.1 are the characteristics of the core design and components. The
 56 TREAT core consists of 19×19 (361) assemblies arranged in 4×4 -inch² lattice with a
 57 height of 8 feet (about 2.4 m). The 361 assemblies are the control rods, the experiment
 58 assembly (IEV), the graphite reflector assemblies, and the fuel assemblies. The TREAT
 59 core can be configured by loading these assemblies into different positions for desired nuclear
 60 parameters or experimental objectives [3]. The configurable core, together with the versatile
 61 IEV design, represent TREAT’s flexible nature, which enables testing different fuel specimens
 62 in multiple accident scenarios. At the center of the core is a test hole through which the IEV
 63 is inserted. Typically, the IEV replaces one or two assemblies, thus, the irradiated volume
 64 is 4×4 inch² \times 4 feet (one assembly is replaced) or 4×8 inch² \times 4 feet (two assemblies are
 65 replaced). The core is reflected by about 2 ft. of graphite on all sides.

66 The fuel assemblies have 4-feet (1.2 m) active height in the middle. The fuel is 93.1%
 67 enriched high enriched uranium (HEU) of UO₂. The fuel is dispersed in a graphite matrix
 68 (about 1:10000 ²³⁵U/C atom ratio) [1], or 0.2 wt% ²³⁵U in the total fuel mixture [13]. The
 69 dilute distribution of uranium oxide in the fuel blocks rapidly transfers the transient heat
 70 into the graphite heat sink/moderator, which causes a neutron energy spectral shift with
 71 strong negative temperature feedback for safe self-limiting power excursions [3]. As part of
 72 the Materials Management and Minimization program, designing, qualifying, and fabrication
 73 of a new low enrichment uranium (LEU) core to substitute the original 60-year old HEU fuel
 74 core is under investigation [22].

Table 1.1: Core design and components of TREAT, after Ref. [13].

Effective core height (cm)	122	Reactor driver fuel coolant	air
Driver fuel	UO ₂	Enrichment (wt%)	93.1
Driver fuel cladding	zircaloy-3	Driver fuel peak temperature (°C)	820

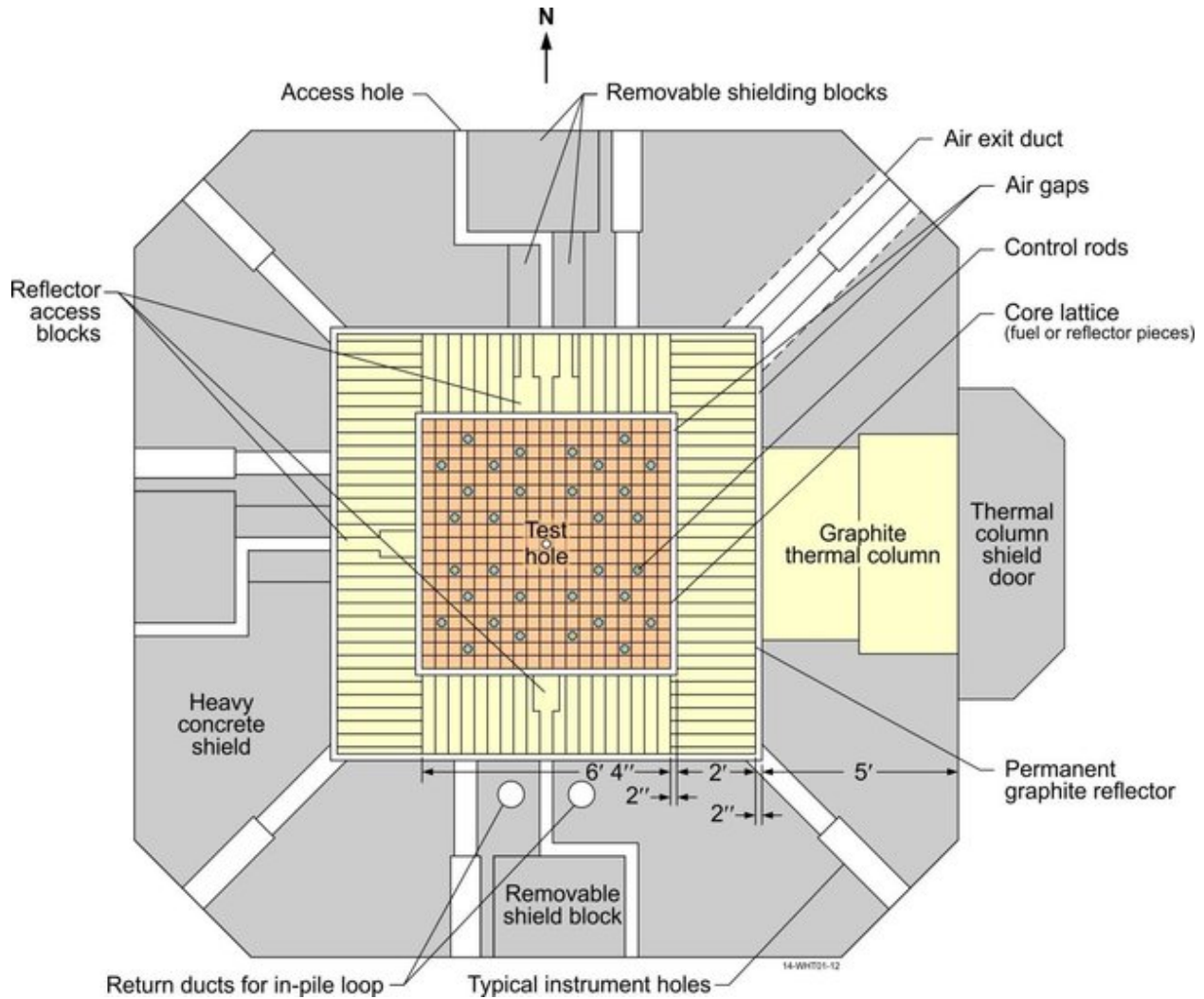


Figure 1.2: Top view of the TREAT core, permanent reflector, and biological shielding, from Ref. [1].

75 1.2.2 Irradiation Experiment Vehicle (IEV)

76 One of the TREAT flexibilities comes from the irradiation experiment vehicles (IEV). In a
 77 transient experiment, the specimen is first loaded into the IEV at the Hot Fuel Examination
 78 Facility (HFEF) at the INL Materials and Fuels Complex (MFC). The loaded IEV is then
 79 transported to TREAT and inserted into the core by replacing one or two TREAT core
 80 assemblies. Thus, the specimen is irradiated in an isolated environment in the IEV. If the
 81 specimen fails in a transient experiment, the IEV prevents the contamination of the TREAT
 82 core. The IEV can be designed to simulate specific environment for the specimen, e.g.,

83 static fluid/moderator or recirculating coolant system. This allows the experiment to use
84 essentially any working fluid (water, sodium, helium, etc.) at desired pressures, temperatures
85 and flow rates [1]. Therefore, TREAT can be used to test different fuels, e.g., light water
86 reactor fuels and sodium-cooled fast reactor fuels, by using different IEVs (currently available
87 or designing new ones) without changing the core configuration. In addition, both irradiated
88 and pre-irradiated fuel specimens can be tested [13].

89 Different IEVs exist, and the Mark-III sodium loop is one of them. The Mark-III sodium
90 loop is used in the historic TREAT transient experiments, and it also provides a basis for
91 the new IEV designs [14]. A schematic of the loop is shown in Fig. 1.3. Two parallel legs
92 of the loop have a height of 3.5 m and are separated by about 0.1 m [2]. In an experiment,
93 the loop is first loaded into a container, then, the container replaces one or two TREAT fuel
94 assemblies to insert into the test hole at the center of the TREAT core, which is shown in
95 Fig. 1.2. One leg of the loop contains a removable test train to load the specimen. The other
96 leg has a pump to circulate the sodium coolant. The sodium is circulated to pass through
97 the specimen in an upward direction, which simulates the coolant environment. Features of
98 the loop are summarized in Table 1.2.

99 Up to seven fuel specimens can be loaded into the test train. Each specimen is posi-
100 tioned in a stainless steel flowtube. At the entrance of each flowtube, a properly-sized orifice
101 is installed to distribute particular amount of the sodium coolant into the flowtube. Ther-
102 mocouples are attached to the outer surfaces of each flowtube at the outlet and along the
103 fuel zone to measure the sodium temperature. To minimize the temperature gradient, the
104 wall of the flowtube is made with thickness less than 0.5 mm. The flowtube is surrounded
105 by a shield tube for isolation. The space between the flowtube and the shield tube is filled
106 with inert gas. If a flowtube fails, the shield tube prevents the debris from damaging the
107 neighbor flowtubes and the test train.

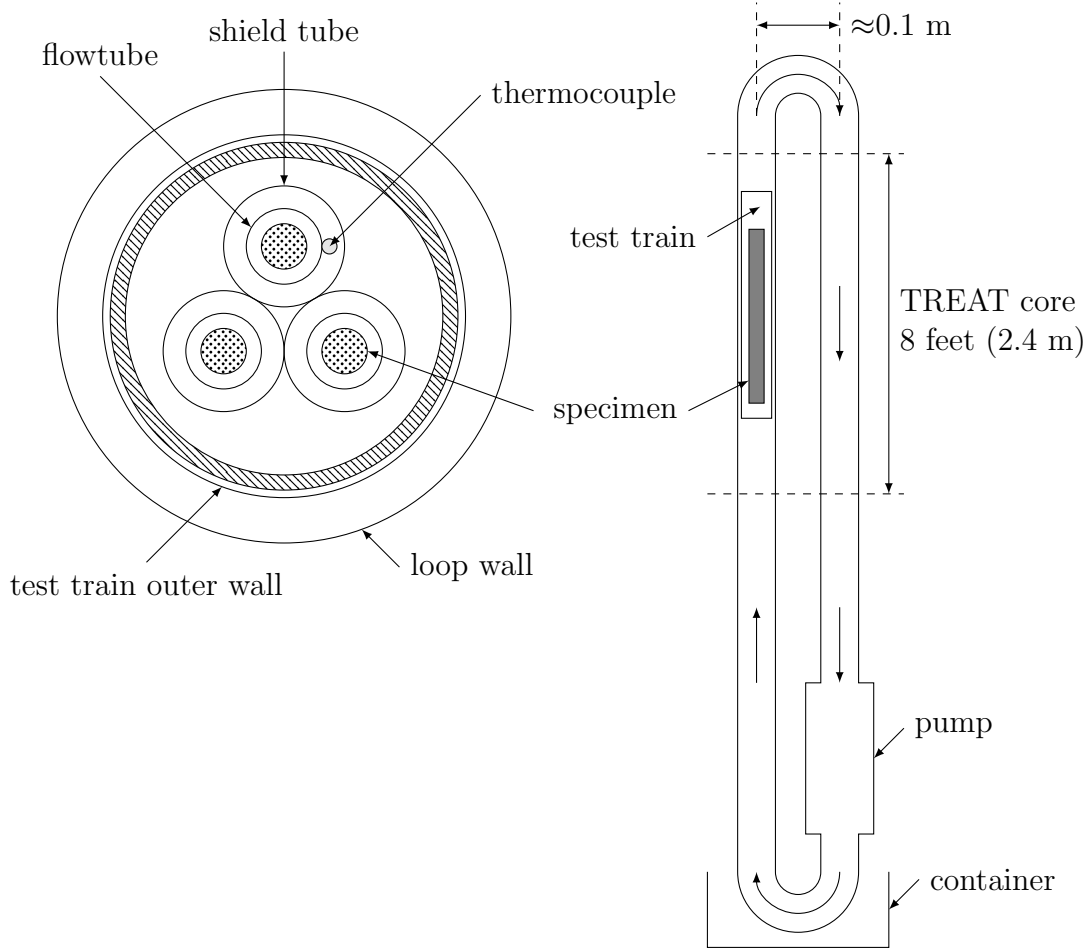


Figure 1.3: Schematic of the Mark-III sodium loop with three fuel pins loaded, after Ref. [2]. The loop has a capacity of 7 fuel pins.

Table 1.2: Features of the Mark-III sodium loop, after Ref. [14].

Parameter	Value
Design pressure	34.5 MPa at 538 °C
Test section inlet temperature (pre-transient)	$\leq 400^\circ \text{C}$
Volume of sodium	≈ 2 liters
Mass of sodium	≈ 1.25 kg
Sodium flow velocity	≤ 7 m/s
Sodium flow rate	≤ 1.2 liter/s
Mass of loop	115 kg

108 1.2.3 Operation Modes

109 TREAT can be operated in the steady-state and the transient modes. The operating charac-
 110 teristics under different modes are listed in Table 1.3. The steady-state mode has a maximum

111 thermal power of 120 kW and neutron flux of $4 \times 10^{11} \text{ cm}^{-2}\text{s}^{-1}$. The heat generated under
 112 this mode can be sufficiently removed by the cooling air. The steady-state mode is mainly
 113 used for physics measurements, isotope build-in (e.g., ^{131}I) for follow-on tests, neutron ra-
 114 diography, and other system checkout operations [3].

115 The distinctive capability of TREAT is its transients, which can provide neutron flux
 116 up to $10^{17} \text{ cm}^{-2}\text{s}^{-1}$. Ref. [13] divides the TREAT transients into the temperature limited,
 117 shaped, and the extended transients, as shown in Table 1.3. However, Ref. [3] categorizes
 118 the transients as the exponential and the shaped transients. The exponential transient has
 119 peak flux shape and usually lasts less than a second. The shaped transient offers flat flux
 120 shape and can be maintained longer than the exponential transient. The shaped transient
 121 is produced by a step insertion of reactivity followed by reactivity insertion or removal at
 122 rates required to produce the desired burst shape [3].

Table 1.3: Operating characteristics of TREAT, after Ref. [13]. The nominal pulse duration is the full width at half maximum (FWHM).

	Temperature limited	Shaped transient	Extended	Steady state
Nominal pulse duration	< 1 s	seconds	minutes	N.A.
Max core power (thermal)	19 GW	10 GW	N.A.	120 kW
Max core energy (MJ)	2900	2900	≥ 2600	N.A.
Max thermal neutron flux ($\text{cm}^{-2}\text{s}^{-1}$)	1.0×10^{17}	1.0×10^{17}	1.0×10^{17}	4.0×10^{11}

123 Duration of the transients is limited by the temperature. A transient is terminated if
 124 the peak fuel and clad temperature exceeds 600 °C. In the shaped transients under current
 125 core configuration, a step insertion of about 4.6% $\Delta k/k$ can reach the temperature limit of
 126 600 °C, and an insertion of 5.9% $\Delta k/k$ can achieve a temperature of 820 °C [3], which is
 127 the driver fuel peak temperature, as shown in Table 1.1. In addition, in the exponential
 128 transients, the control rods can be inserted at high drive speed to suspend the transient,
 129 i.e., the pulse width is narrowed, before the temperature limit is reached. This mechanism
 130 is termed rod-and-temperature-limited excursions [3].

1.2.4 Pulse Narrowing

Upon resumption of TREAT, the LWR fuels, especially the ATFs, will be tested. Behavior of the LWR fuels in the postulated Hot Zero Power Reactivity Initiated Accidents (HZP-RIA) is of interest. An HZP-RIA happens when the control elements (blades, rods, etc.) are withdrawn from an LWR core in the condition that the reactor is preheated to operational inlet temperatures, but not yet producing fission power. A brief nuclear power excursion may happen where rapid fuel pellet thermal expansion could drive cladding failure through mechanical interaction [3].

To simulate the HZP-RIA, the transient pulse width, which is usually measured by full width at half maximum (FWHM), is a critical parameter. Pulses with 30-ms FWHM can create more than doubled peak cladding hoop stress than pulses with 90-ms FWHM [3]. To simulate the HZP-RIAs, the desired pulse width range for pressurized water reactor (PWR) is 25 to 65 ms FWHM, and 45 to 75 ms for boiling water reactor (BWR). However, current FWHM of TREAT pulses is about 100 ms [3], which is too wide for the HZP-RIA testing. Hence, narrowing the TREAT pulses is necessary.

It is under investigation to narrow the TREAT pulse width with increased reactivity insertion (to initiate the pulse) and rapid termination at the end of the pulse (clip) [3]. RELAP5-3D is used to calculate the FWHMs under different reactivity insertions, and the results are shown in Fig. 1.4. In the calculation, the reactor is allowed to respond naturally to the reactivity insertion, i.e., the temperature can exceed the 600 °C limit, and no clipping is applied. As the reactivity insertion increases, the FWHM decreases, and the maximum fuel temperature increases. By reducing the total peaking factor from 1.82 to 1.6, which might be achieved via optimizing the core loading, the maximum fuel temperature decreases at the same reactivity insertion. Thus, if the temperature limit is considered, at 600 °C, the total peaking factor of 1.82 allows a reactivity insertion of about 4.46% $\Delta k/k$, and the FWHM is about 106 ms. For the total peaking factor of 1.6, the allowed reactivity insertion is approximately 4.85% $\Delta k/k$, and the FWHM is 97 ms. Hence, only increasing the reactivity insertion, even under optimized total peaking factor, can not narrow the TREAT pulse width

159 to the desired range for the HZP-RIA simulation. Though not effective in narrowing the
 160 pulse width, larger reactivity insertion may deposit more energy into the specimen. To allow
 161 larger reactivity insertion, numerical core power flattening studies indicate the fuel assembly
 162 power can be reduced on the order of about 20% [3], i.e., assuming the maximum core
 163 temperature varies linearly with reactivity insertion, at 600°C limit, the reactivity insertion
 164 can be increased by a factor of 1.25.

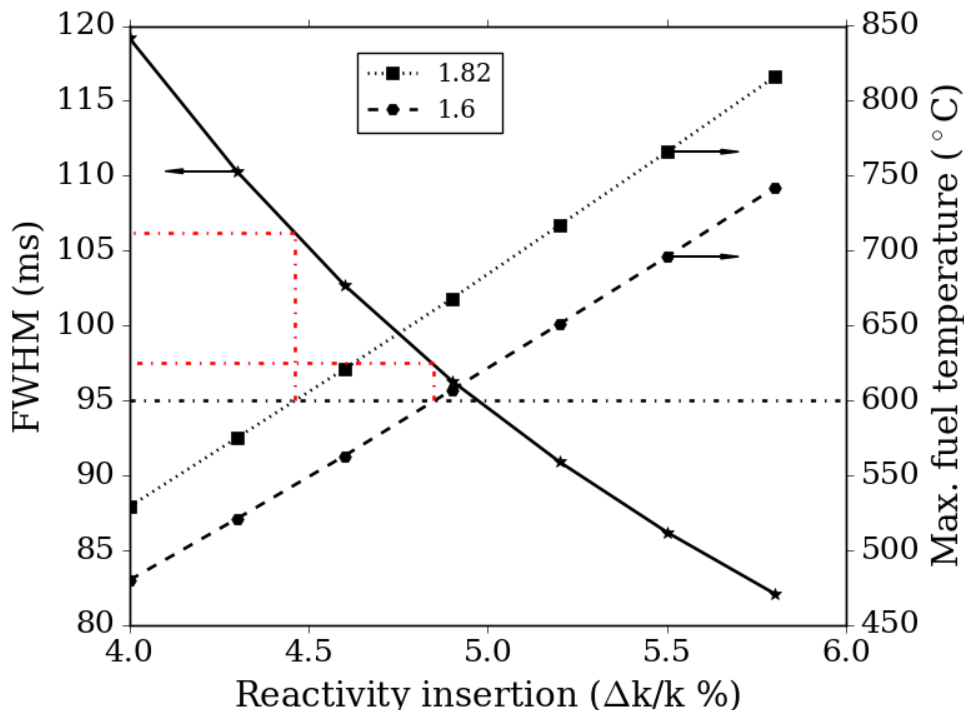


Figure 1.4: FWHM of the TREAT pulse and maximum fuel temperature varies with reactivity insertions, after Ref. [3]. Results under total peaking factors 1.82 and 1.6 are shown.

165 The clipping techniques are considered to narrow the pulse width further, which consist
 166 of increasing the drive speed of the transient rods and a more advanced hypothetical ^3He
 167 system. Numerical evaluation indicates that, at reactivity insertion of 4.5% $\Delta k/k$, increase
 168 the drive speed of the transient rods from the current maximum 140 to 250 inch/s, the
 169 FWHM reduces from 95 ms to 77 ms. When the hypothetical ^3He system is applied, which
 170 represents a reactivity insertion of -5% $\Delta k/k$ in 5 ms, the FWHM can be reduced to the
 171 desired 46 ms [3]. Hence, the ^3He system is more effective than increasing the drive speed
 172 of the transient rods. Ongoing efforts focus on realizing the ^3He system [3].

1.2.5 In-Core Neutron Detectors

TREAT used the prompt-type Self-Powered Neutron Detectors (SPNDs) to measure the in-core neutron flux [4]. A schematic of the SPNDs is shown in Fig. 1.5, and the details are listed in Table 1.4. The SPNDs consist of the Inconel 600 sheath (collector), the alumina insulator, the emitter (hafnium or gadolinium), and two Inconel leadwires. The sheaths and the emitters have cylindrical shapes. The emitter is embedded in the insulator and is positioned from one end of the tube by 12.7 mm. SPNDs with different emitter lengths were used, where the Hf emitters have lengths of about 40 cm, and the Gd emitters have lengths of 2.413 and 2.852 cm, respectively. To adapt the Hf emitter length comparable to the Gd value, a steel rod was used to shield the emitter region of the Hf SPND, after which the neutron-sensitive section of the Hf SPNDs has length of 3.18 cm [4]. A leadwire connects the emitter to the external electronics. A second leadwire is used to compensate the background signal. This background leadwire differs from the emitter leadwire that it ends in the insulator near (not connects to) the emitter.

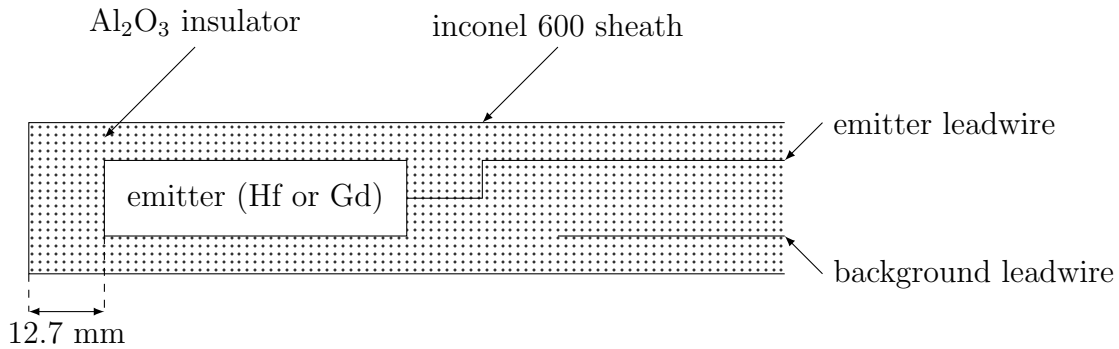


Figure 1.5: The prompt SPNDs used in TREAT, after Ref. [4].

Neutrons may be captured in the emitter, and prompt gamma rays are emitted within about 10^{-13} s [23]. The gamma rays may interact in the emitter mainly via Compton scattering or the photoelectric effect and generate electrons. Additionally, internal conversion electrons may also be produced [4]. If these electrons have sufficient energy, they may travel to the sheath from the emitter and leave the emitter positively charged. This electron motion can be measured as current in the external circuit, which is the signal.

Table 1.4: Details of the SPNDs used in TREAT, after [4].

	Hafnium (Hf)	Gadolinium (Gd)
Emitter		
Material	97.5%Hf min., 2.5%Zr max.	99.7%Gd
Length (cm)	≈ 40	2.413 or 2.852
Diameter (mm)	0.4572	0.559
Mass (g) (nominal)	0.873	0.0508
Leadwire (two each)		
Material	Inconel 600	
Diameter (mm)	0.203	0.229
Sheath		
Material	Inconel 600	
O.D. (mm)	1.372	1.575
Wall thickness (mm)	0.229	0.279
Insulation		
Material	Aluminum Oxide	
Purity	99.65%	99.65%
Compaction	about 70% of theoretical density	

193 The main background of the SPND is the gamma rays from the neutron capture in the
194 core, as opposed to the gamma rays from fission [4]. These gamma rays are proportional to
195 the neutron flux. If the background gamma rays interact in the emitter and eject electrons,
196 the resulted current contributes to signal. However, the background gamma rays may interact
197 within the sheath, and the ejected electrons may travel from the sheath to the leadwire, which
198 produces background potential gradient between the sheath and leadwire. This background
199 potential gradient is compensated by the background leadwire.

200 Space charge exists in the insulator of the SPND, which is produced by the low-energy
201 electrons. The low-energy electrons entering the insulator may be at thermal equilibrium
202 within the insulator. Due to the charge traps and the insulator's energy band structure, the
203 electrons spend a finite time ("dwell" time) in the insulator before drifting to the electrode.
204 These electrons in the insulator constitute the space charge [24]. The space charge grows and
205 reaches a quasistatic state, in which the number of electrons entering equals to the number
206 of electrons leaving the insulator. The space charge introduces an electric field, which has

207 one zero point, or potential peak, in the insulator [25]. The electric field vectors point in
 208 opposite directions on the two sides of the potential peak [24], as shown in Fig. 1.6. In
 209 other words, for the electrons traveling from the origin electrode (emitter or sheath) to the
 210 potential peak, the electric field repels the electrons back to their origin electrode. For the
 211 electrons with sufficient kinetic energy to cross the potential peak and traveling from the
 212 peak location to the non-origin electrode, the electric field accelerates them. For the SPNDs
 213 used in TREAT, the electrons need to have a minimum kinetic energy of about 260 keV
 214 to penetrate the space charge, and contribute to the signal [4]. If the kinetic energy is
 215 insufficient, the electron is repelled back, and its overall contribution to the signal is zero.
 216 Additionally, the space charge is insensitive to the operating temperature of the SPNDs in
 217 the TREAT core [4].

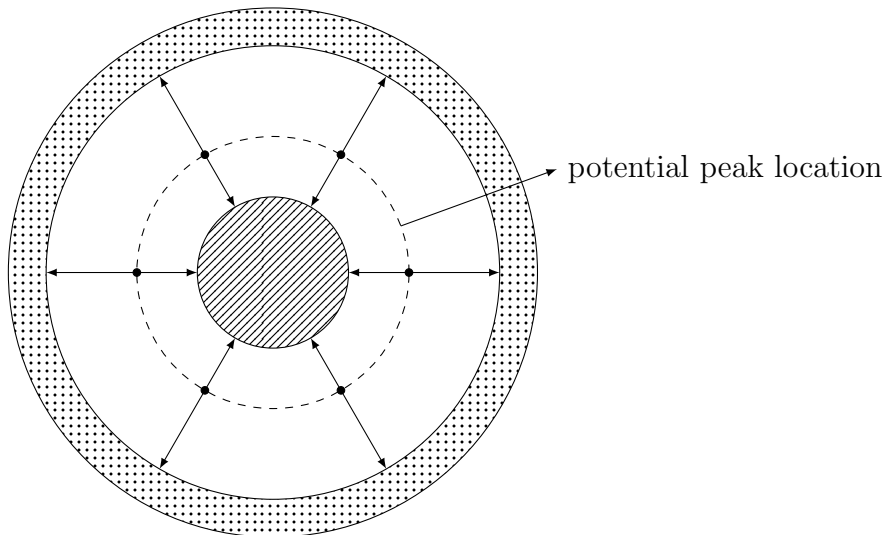


Figure 1.6: Schematic of the force directions on the electrons introduced by the space-charge electric field in the SPNDs.

218 1.2.6 Reactivity and Transient Control Mechanism

219 Shown in Table 1.5 is the reactivity and control rod characteristics of TREAT. TREAT
 220 has a temperature coefficient of $-1.8 \times 10^{-4} \Delta k/k/^\circ\text{C}$, which is mainly contributed from
 221 the graphite in the driver fuel due to a thermal Maxwellian shift with increased leakage [1].
 222 TREAT has 20 control rods with 152.4 cm active absorber length [15]. These 20 control rods

223 are four Compensation Rods, 8 Control/Shutdown Rods and 8 Transient Rods. Layout of
 224 these rods is shown in Fig. 1.7. During transient operation, the Compensation Rods are used
 225 at the end of the transient to shut down the reactor, providing excess negative reactivity.
 226 The Control/Shutdown Rods are used to establish pre-transient criticality and remain fixed
 227 and partially inserted into the core during a transient. The Transient Rods are rapidly
 228 withdrawn to initiate transient conditions during transient operation, and can be moved to
 229 shape the transient with time. Ref. [3] reports the maximum speed of the transient rods is
 230 140 inch per second. However, Ref. [26] states the transient rods have the maximum speed
 231 of 170 inch per second and have a 40-inch stroke, i.e., the transient rods can navigate the
 232 full stroke in about 0.24 seconds.

Table 1.5: Reactivity and transient control mechanism characteristics of TREAT, after Ref. [13, 15]. Ref. [13] stats the number of transient rods is one. Ref. [15] reports the number is eight, which is listed here.

Temperature coefficient ($\Delta k/k/^\circ\text{C}$)	-1.8×10^{-4}	Moderator	graphite
Number of control rods	20	Control rod material	B_4C
Number of transient rods	8 [15]	Transient rod absorbing material	Mild Steel, CP-2 graphite, chrome plating

233 1.2.7 Hodoscope

234 The hodoscope is used to monitor the fuel motion in the transient tests. A schematic of
 235 the hodoscope is shown in Fig. 1.8. The hodoscope has a thick conical front collimator, a
 236 rear collimator with over 300 diverging slots, the lead filter, and the neutron detector arrays
 237 to detect the collimated fission neutrons through the respective slots. The rear collimator
 238 consists of 30 low-carbon steel plates, selection of which over the hydrogenous mixtures is
 239 due to the machinability and the attenuation of the gamma rays from the core [11]. The
 240 detector slots have approximately 1 inch diameter [6]. Fission neutrons from the specimen
 241 can travel through the slotted TREAT hodoscope assemblies, the graphite reflector, and the
 242 collimators to be detected. Then, the fuel motion as a function of space and time can be
 243 monitored.

244 While the steel collimator suppresses some gamma rays from the core, it introduces

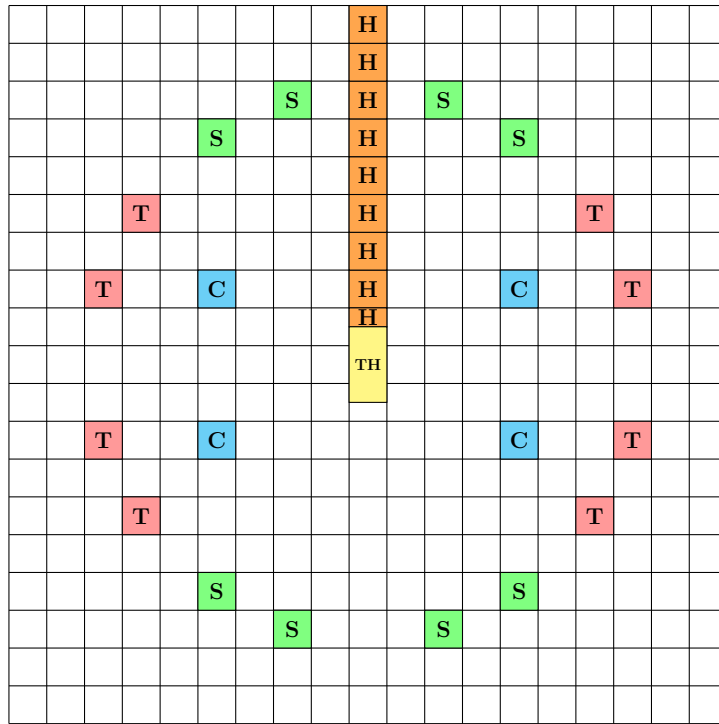


Figure 1.7: Current layout of the TREAT control rods, after Ref. [3]. **T** is the transient rods. **C** is the compensation rod. **S** is the control/shutdown rod. **H** represents the slotted hodoscope assembly. **TH** stands for the test hole.

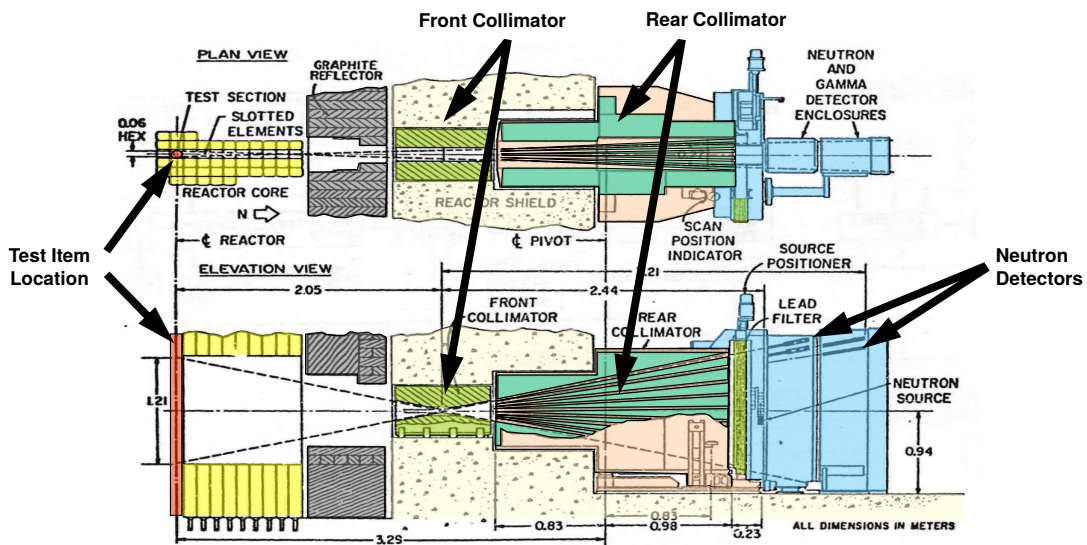


Figure 1.8: Schematic of the TREAT hodoscope, from Ref. [5].

245 another source of gamma rays by capturing neutrons from the core and sample. For ^{56}Fe
 246 (with atomic abundance of 91.75% in natural iron), the most-probable gamma rays are
 247 7.6 MeV with intensity of 29 ± 4.94 per 100 neutron captures [27]. The thermal neutron

capture cross section and the resonance integral of ^{56}Fe are 2.6 and 1.4 barn, respectively. The gamma rays, from the neutron capture in steel and from the core, may further collide via the pair production, Compton scattering, and the photoelectric effect. These capture gammas that arrive the hodoscope fast-neutron detectors constitute a major source of background.

1.2.8 Hodoscope Detectors

It is a challenge to design a hodoscope fast-neutron detector that exhibits good performance over the wide power range of TREAT transients (from MW to 19 GW). The original TREAT hodoscope uses the Hornyak button fast-neutron detectors, design of which considers the linearity, count-rate capacity, dead time, gamma-ray rejection, efficiency, time and spatial resolution at 100-MW power [11]. A schematic of the Hornyak button is shown in Fig. 1.9. It consists of a $2.8 \times 15.9 \times 25.4 \text{ mm}^3$ central active rectangular slab and optically coupled half-cylinder PMMA (Lucite) light guides. The slab is a mixture of 5% mass ratio ZnS:Ag in the PMMA.

Fast neutrons primarily interact with the hydrogen in the detector to generate recoil protons. If the recoil protons deposit energy in the suspended scintillating ZnS:Ag particles, light is emitted. The light can then be shuttled to the photomultiplier tube (PMT) connected to the rear end by the light guides to generate detectable pulses. Another mechanism to generate light is the $^{32}\text{S}(n, p)^{32}\text{P}$ reaction [28], in which the neutron directly interacts with the sulfur nuclide in ZnS:Ag. The Q value of this reaction is -0.93 MeV, and the microscopic cross section is 0.017 b at 2 MeV. Under ideal conditions, the Hornyak button has an efficiency of about 0.4% for neutrons with energy above 0.1 MeV, with good rejection of about 10^{-8} counts per incident gamma ray [11] after applying the pulse-shaping technique [29]. The gamma-ray rejection may be enhanced further by using the passive or active cancellation circuits [30].

The Hornyak buttons lose linearity between count rate and transient power for power levels above 100 MW [11]. At power levels in a few GW, the count rates of the Hornyak buttons are 10 or 20 times greater than the values extrapolated from the readouts at lower

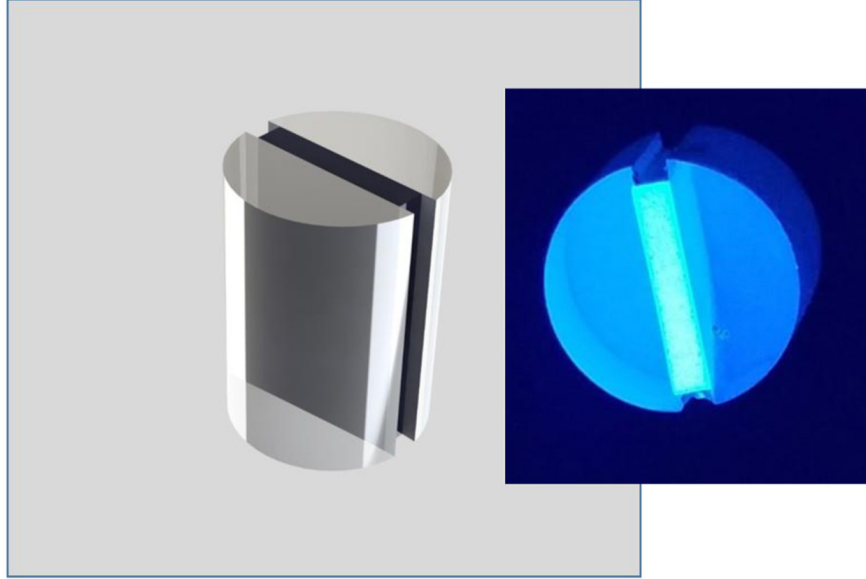


Figure 1.9: Schematic of the Hornyak button fast neutron detector, from Ref. [6].

275 power level, which are mainly caused by the fast neutrons. These large count rates cause
276 channel saturation in the detector responses. The large count rates are verified to be caused
277 by the gamma rays [11]. The gamma rays may generate electrons with velocities larger than
278 the speed of light in the transparent dielectric, e.g., PMMA in the Hornyak button and the
279 photomultiplier glass envelope, via the photoelectric effect, Compton scattering, and pair
280 production [23]. Movement of the high-speed electrons produces the Cherenkov light [31].
281 This Cherenkov light generates competitive pulses responsible for the excessive noise count
282 rates. To eliminate the nonlinearity caused by the gamma ray flash saturation, a lead filter
283 with thickness ranging from 0.375 in. for 30 MW to 2 in. for 16 GW is placed between the
284 collimator and the detector array [11], as shown in Fig. 1.8.

285 **1.3 Modeling of Novel Neutron Detectors for TREAT**

286 To support future operations of TREAT, alternative hodoscope fast-neutron and in-core
287 thermal-neutron detectors are under development at Kansas State University (KSU). The
288 hodoscope detectors, as alternatives to the Hornyak buttons, are layered and homogenized
289 ZnS(Ag)-PMMA scintillation detectors, and fast-sensitive, microstructured semiconductor

290 neutron detectors (MSNDs). The in-core detectors considered are the micro-pocket fission
291 detectors (MPFDs), which are alternatives to the SPNDs used in the TREAT core.

292 The goal of this work is to model and simulate these novel neutron detectors for TREAT to
293 assist development and design. Based on the knowledge of radiation detection, the detectors
294 are designed to have qualitatively good performance for the TREAT applications. Modeling
295 of the detectors can give a quantitative verification of the design by simulating the underlying
296 physics. Simulation is usually cheaper and requires less time than constructing and testing
297 multiple prototypes in the experiments. Numerical evaluation can also calculate quantities
298 that are difficult to measure in experiments. Predictive modeling can be used to optimize
299 the parameters of the detectors. Once optimized detectors are constructed, the numerical
300 and the experimental results can be compared, which contributes to the validation of the
301 simulation codes.

302 **1.3.1 ZnS(Ag)-Based Scintillation Detectors**

303 The proposed hodoscope detectors are designed for good neutron-detection efficiency while
304 rejecting gamma noise using simple pulse-height discrimination, i.e., achieving sufficiently
305 high signal-to-noise (S/N) ratio. The layered and the homogenized ZnS(Ag)-PMMA scin-
306 tillation detectors are evolutions of the existing Hornyak buttons. The scintillation volume
307 of the layer detector consists of alternating layers of ZnS(Ag) and PMMA. The scintillation
308 volume of the homogenized detectors is like the Hornyak button, i.e., a homogeneous mixture
309 of ZnS(Ag) and PMMA. The scintillation volumes of the new detectors are surrounded by
310 silicon photomultipliers (SiPMs) to collect light. Compared to the Hornyak buttons, the use
311 of SiPMs replaces the light guides and the PMT, which reduces Cherenkov noise.

312 To evaluate S/N ratios of the hodoscope detectors, the responses to the fast neutrons and
313 the gamma rays in the hodoscope radiation environment are of interest. For the scintillation
314 detectors, the transportations of radiation particles, i.e., neutrons and gamma rays, and
315 light are simulated in Geant4 (for GEometry ANd Tracking) [32]. The Hornyak buttons are
316 modeled to validate the physical models and approximations. The scintillation volumes of

317 the layered and homogenized variants are modeled to optimize the parameters.

318 **1.3.2 Fast-Sensitive MSNDs**

319 The proposed fast-sensitive MSNDs are adapted from the existing, thermal-sensitive design,
320 which has long been developed at KSU, by using fast-sensitive neutron converters. In the
321 fast-sensitive MSNDs, gamma rays may interact within the silicon base, but the strong,
322 gamma-induced Cherenkov noise is eliminated because no transparent dielectric material
323 exists in the devices, and the MSNDs are not scintillation detectors. The fast-sensitive
324 converters considered are actinides and paraffin wax. The actinide MSNDs allow for high,
325 lower-level discriminator (LLD) settings due to the high-energy fission fragments. The major
326 concern is the neutron-detection efficiency that can be achieved with use of actinide reactants.
327 The paraffin wax has a larger macroscopic cross section for fast neutrons than any actinide.
328 Because the recoil protons have less energy than the fission fragments, hydrogenous MSND
329 designs are considered that maximize the energy deposition of the protons in the silicon
330 depletion region to distinguish neutrons from gamma rays.

331 Fast-sensitive MSNDs are evaluated using Geant4 and MCNP (Monte Carlo N-Particle)
332 [33] for comparison. For the actinide MSNDs, the fission fragment generator (FFG) in Geant4
333 [34] is used to sample and track the fission fragments in a single run. This feature is more
334 convenient than MCNP, where the energy of the fission fragments is assumed to be deposited
335 locally, i.e., in the volume where the fission reaction happens [35]. To evaluate the actinide
336 MSNDs, the deposited energy outside the fission site, i.e., in the active silicon region, is the
337 tally. For the hydrogenous MSNDs, both codes are used to simulate the neutron responses,
338 and Geant4 is used to evaluate gamma-ray noise.

339 **1.3.3 Micro-Pocket Fission Detectors**

340 The MPFDs are gas detectors using the fission reaction to convert in-core neutrons to dis-
341 cernible electric signals. A thin fissile layer is deposited on one side of the chamber. One of the
342 fission fragment pair enters the gas and deposits a few MeV of energy, which distinguishes a

343 neutron event from other in-core radiations. The deposited energy ionizes electron-ion pairs,
344 and the charge carriers are drifted to respective electrodes under an applied electric field,
345 thereby producing a measurable signal.

346 To evaluate the dynamic response of MPFDs, a computational routine consisting of the
347 Garfield++ [36], Gmsh [37], Elmer [38], and stopping and range of ions in matter (SRIM)
348 [39] was used. Elmer computes the electric field using the finite-element method based on the
349 meshed geometry generated by Gmsh. SRIM calculates the energy loss tables of the fission
350 fragments in the gas. Garfield++ computes the energy loss of the fission fragment, simulates
351 the drift of electrons in the gas under applied electric field, and calculates the induced signal.
352 The application using Garfield++ is parallelized using hybrid Message Passing Interface
353 (MPI) and OpenMP.

354 **1.4 Organization of the Dissertation**

355 Chapter 2 reviews the common neutron-detection techniques. Chapter 3 reviews the Monte
356 Carlo method and introduces the Geant4 code used to evaluate the neutron detectors. Chap-
357 ter 4 presents the approximations and physics to evaluate the hodoscope detectors, and the
358 simulated results of the Hornyak buttons. Chapters 5, 6, and 7 models and simulates the
359 Hornyak-button variants, the fast-sensitive MSNDs, and the MPFDs, respectively. Chapter 8
360 concludes the dissertation and provides the future work.

361 Chapter 2

362 Neutron Detection Techniques

363 Neutrons are detected indirectly via signals generated by deposited energy of secondary
364 charge particles. Neutrons are converted to secondary particles through different absorptive
365 or scattering reactions. The secondary particles deposit energy and generate signals via
366 electron-ion pairs in a gas-filled detector, scintillation light in a scintillation detector, and
367 electron-hole pairs in a semiconductor detector. Coupling of neutron converting reaction
368 and signal-forming mechanism creates various neutron detectors for different applications.
369 In this chapter, common neutron detection techniques are reviewed.

370 2.1 Converting Reactions

371 To develop neutron detectors for a specific application, the cross section of the converting
372 reaction and the kinetic energy of the secondary charged particles must be considered. The
373 cross section affects the detector's intrinsic efficiency, and the kinetic energy of the charged
374 particles determines the allowed lower-level discriminator to reject background noise. In this
375 section, these two aspects of common neutron converting reactions are introduced.

376 2.1.1 Thermal Absorptive Reactions

377 Three common absorption reactions to detect thermal neutron are compared in Table 2.1.
 378 ^3He gas proportional counters are widely used in neutron scattering science and homeland
 379 security applications [40] due to the large thermal neutron cross section (5400 b at 0.025 eV).
 380 Helium-3 gas is produced from the decay of tritium, which is produced by nuclear weapons
 381 programs in the U.S. and Russia [40]. Due to the shortage and rising cost of ^3He gas,
 382 alternative neutron-detection techniques are sought.

Table 2.1: Comparison of three thermal neutron absorptive reactions, after Ref. [7].

Reaction	Charge particles produced	Q value (MeV)	$\sigma(\text{b})$ at 0.025 eV
$^{10}_5\text{B}(\text{n}, \alpha)^7_3\text{Li}$	$\alpha, ^7\text{Li}$	2.78	3840
$^6_3\text{Li}(\text{n}, \alpha)^3_1\text{H}$	$\alpha, ^3\text{H}$	4.78	937
$^3_2\text{He}(\text{n}, \text{p})^3_1\text{H}$	$\text{p}, ^3\text{H}$	0.765	5400

383 Boron- or lithium-based neutron detectors have been developed as ^3He -replacement tech-
 384 niques. The ^{10}B reaction has a larger cross section than ^6Li ; however, the ^6Li reaction has a
 385 larger Q value, which can make discrimination of background radiation easier. One proposed
 386 ^3He -replacement technology of relevance to the present work is the microstructured semicon-
 387 ductor neutron detector (MSND) [41], which employs ^6LiF to convert thermal neutrons. The
 388 most recent generation of MSNDs (so-called “dual-sided” MSNDs) has exhibited an intrinsic
 389 thermal neutron detection efficiency of nearly 70% [42].

390 2.1.2 Proton-Recoil Reaction

391 The main scattering reaction to convert fast neutrons is elastic scattering between an incident
 392 neutron and a hydrogen nucleus, i.e., a single proton. As shown in Fig. 2.1, a neutron with
 393 kinetic energy E_n collides with a proton at rest. The kinetic energy of the recoil proton, E_p ,
 394 for θ in the laboratory system is

$$E_p = E_n \cos^2 \theta. \quad (2.1)$$

395 This scattering process is isotropic in the center-of-mass system for neutron energy up to
396 about 14 MeV, and on average, half of the neutron energy is transferred to the recoil proton.
397 The microscopic cross section of this reaction decreases from approximately 13 b at neutron
398 energy of 0.1 MeV to about 1 b at neutron energy of 10 MeV.

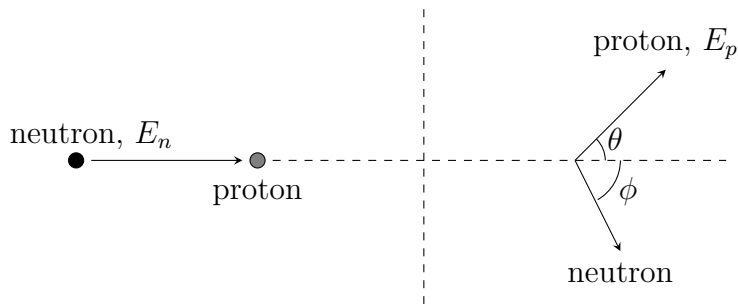


Figure 2.1: Kinematics of neutron-proton collision in the laboratory system.

399 2.1.3 Fission Reactions

400 Fission reactions are used to convert thermal or fast neutrons, depending on the actinide
401 materials used [43]. ^{235}U has a large fission cross section for thermal neutrons (587 b at
402 0.025 eV). ^{237}Np exhibits a 0.5-MeV threshold for the fission reaction, and the cross section
403 is about 1 to 2 b for neutron energies between 1 and 10 MeV.

404 Fission reactions are valuable for use in high-background applications due to the large
405 energy of fission fragments (and, hence, the large energy deposited by those fragments).
406 In the thermal fission of ^{235}U , the fission fragments carry away approximately 168 MeV of
407 energy [23], which allows one to use high lower-level discriminator settings.

408 2.2 Signal-Forming Mechanisms

409 Secondary charge particles from neutron reactions deposit energy in a detector mainly via
410 Coulomb interactions by ionizing and exciting electrons. Electrons are ionized when they
411 gain sufficient energy from the charge particles to become free particles. If the acquired
412 energy is insufficient, electrons are excited to higher energy states but remain bound to

413 atoms. The excited electrons may drop to lower energy states with photon emission.

414 Neutron detectors have different mechanisms to generate signals. The deposited energy
415 liberates electron-ion pairs in a gas-filled detector, generates electron-hole pairs in a semicon-
416 ductor detector, and produces light in a scintillation detector. In the gas-filled and semicon-
417 ductor detectors, charge carriers are drifted under an applied bias, which induces current in
418 an external circuit. In a scintillation detector, the scintillation photons may interact within
419 a coupled light sensor, e.g., photomultiplier tube (PMT) or silicon photomultiplier (SiPM)
420 [9], and produce photoelectrons. These photoelectrons are amplified by the light sensor to
421 generate a measurable signal.

422 2.2.1 Gas-Filled Detectors

423 The response of a gas-filled detector to incident radiation depends critically on the relation-
424 ship between applied voltage and collected charges, which is shown in Fig. 2.2. When a
425 charged particle enters the gas, it deposits energy and ionizes electron-ion pairs along its
426 path. For many commonly used gases, the energy w required to create an electron-ion pair
427 is between 20 and 40 eV (e.g., w for Ar is 27 eV) [44]. The primary electron-ion pairs are
428 drifted under applied electric field. In the recombination region, the electric field is not
429 strong, and ionized electrons may recombine with ions; hence, little or no signal is formed.
430 No detectors are operated in this region.

431 As the applied voltage is increased to the ionization regime, recombination is effectively
432 eliminated, and the electron-ion pairs are drifted apart completely. The collected charges are
433 proportional to the deposited energy. Hence, the total amount of charge produced by incident
434 α , β , and γ particles differ. In addition, the primary ionized electrons are not accelerated
435 by the electric field sufficiently to produce secondary ionizations. Thus, the induced current
436 is small. Detectors operated in this region are called *ion chambers*, and represent the gas
437 detectors of interest for in-core applications at TREAT and elsewhere in this work.

438 However, further increasing the applied voltage leads to two additional characteristics
439 responses, which are described here for completeness. When the applied voltage enters

440 the proportional region, electrons gain sufficient kinetic energy from the electric field to
 441 produce secondary ionizations and excitations. This effect is called *impact ionization* [23],
 442 and *gas multiplication* appears. The measured current is stronger than ion chambers and
 443 still proportional to the original deposit energy. Detectors operated in this region are named
 444 *proportional counters*.

445 With applied voltage in the Geiger-Muller region, gas multiplication is tremendous. Re-
 446 gardless of the initial deposited energy by the charged particle, the output pulse heights
 447 are essentially the same (i.e., to within statistics). The pulse heights are determined by the
 448 detector configuration, and incident particles are not distinguishable. Detectors operated in
 449 this region are termed *Geiger-Muller (GM) counters*.

450 When applied voltage increases beyond the GM region, continuous discharge occurs. No
 451 detectors are operated in this region.

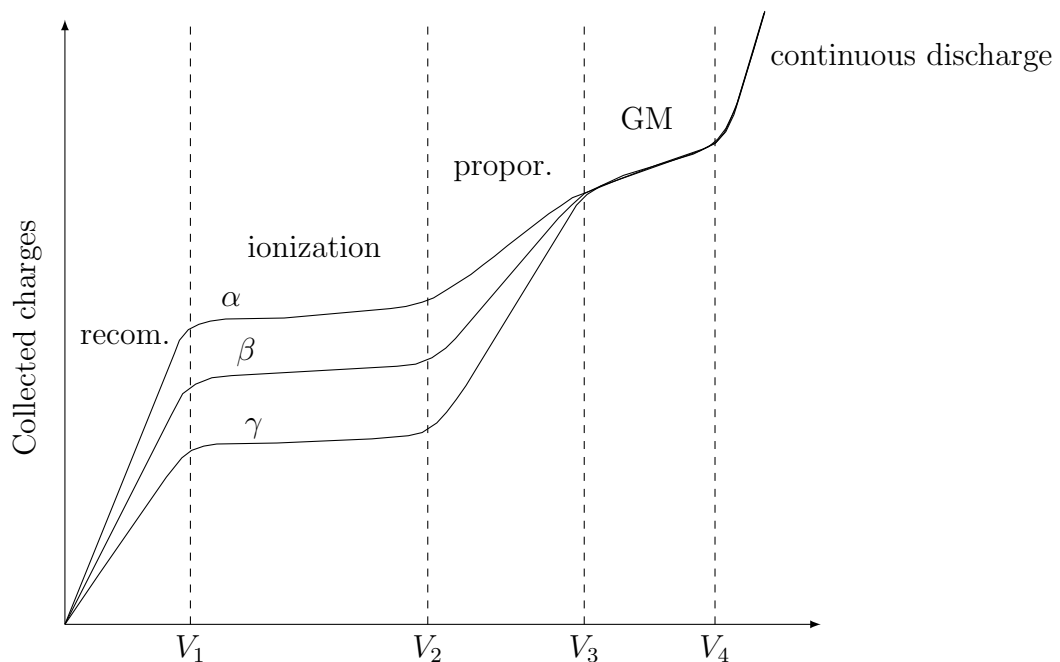


Figure 2.2: The collected charges vary with applied voltage in the gas-filled detectors irradiated by α , β , and γ particles, after Ref. [7].

452 Basic Physics of Ion Chambers

453 Ion chambers can be operated in *pulse mode* or *current mode*. In pulse mode, the induced
454 current is integrated by an external circuit to produce a voltage potential. The voltage is
455 measured to indicate a single radiation event. Then, the circuit is discharged and reset for
456 next radiation event. Pulse mode is generally not suitable for high radiation environment.
457 When the circuit is integrating or discharging current, if a new radiation event happens, it
458 can not be recorded. The period during which a detector cannot respond is called the *dead*
459 *time*. Hence, radiation events during dead time need to be avoided by decreasing the dead
460 time or by reducing the neutron-converting reaction rate.

461 For high radiation fields, current-mode operation is more often used, where the induced
462 current is measured by an ammeter. The measured current indicates the ionization rate from
463 many radiation events in the detector, and a single radiation event is not revealed.

464 Charge collection within an ion chamber depends on the applied voltage and the asso-
465 ciated electric field. To calculate the electric field, the electric potential ψ (V) has to be
466 determined, which follows the Poisson equation, i.e.,

$$\nabla^2\psi = -\rho/\epsilon, \quad (2.2)$$

467 where ρ is the volumetric charge density (C/cm³), and ϵ is the permittivity of the gas
468 (F/cm). Equation (2.2) can be solved subject to appropriate boundary conditions based on
469 the applied bias at the electrodes. Then, the electric field $\boldsymbol{\xi}$ (V/cm) is

$$\boldsymbol{\xi} = -\nabla\psi. \quad (2.3)$$

470 Subject to this electric field, the charge carrier drift speed \boldsymbol{v}_d (cm/s) is

$$\boldsymbol{v}_d = \mu\boldsymbol{\xi}, \quad (2.4)$$

471 where μ is the mobility (cm² V⁻¹ s⁻¹). Mobility is inversely proportional to gas pressure. In

472 calculations, mobility is prepared, e.g., by the MAGBOLTZ program [45], to compute the
 473 drift velocity.

474 Another component of the carrier movement is diffusion, which describes the behavior of
 475 a charge cloud. The diffusion rate can be expressed as

$$\frac{\partial \rho(\mathbf{r}, t)}{\partial t} = D \nabla^2 \rho(\mathbf{r}, t), \quad (2.5)$$

476 where D is the diffusion coefficient (cm^2/s). The diffusion coefficient relates to the mobility
 477 as [10]

$$\frac{D}{\mu} = \frac{kT}{q_e}, \quad (2.6)$$

478 where k is Boltzmann's constant, T is temperature in K, and q_e is elementary charge. Unlike
 479 the deterministic drift velocity, the velocity due to diffusion \mathbf{v}_D of a charge carrier in the
 480 cloud is stochastic. With sampled \mathbf{v}_D , the actual velocity \mathbf{v} is a vector sum of the drift and
 481 diffusion components, i.e.,

$$\mathbf{v} = \mathbf{v}_d + \mathbf{v}_D. \quad (2.7)$$

482 In a Monte Carlo simulation, the distance traveled in a step due to diffusion is sampled
 483 based on the calculated drift distance; this sampling process is described more thoroughly
 484 in Chapter 7.

485 Charge carrier motion induces a current in the external circuit. This induced current can
 486 be determined easily using the Shockley-Ramo theorem, which defines

$$i(t) = -Q \mathbf{v} \cdot \mathbf{E}_w(\mathbf{r}_Q), \quad (2.8)$$

487 where Q is the charge, and \mathbf{E}_w is the weighting electric field at the charge location \mathbf{r}_Q . The
 488 weighting electric field can be calculated by applying unity voltage at the anode. While
 489 the induced current can also be computed by the Green's reciprocity theorem [10], the
 490 Shockley-Ramo theorem is easier to use and is implemented in the Garfield++ code [36].

491 Because the electron mass is thousands times less than that of an ion, under the same

492 electric field, electrons move much faster than ions. Hence, pulses of ion chambers are usually
493 truncated once all electrons are collected for the quickest response, i.e., the resulting pulses
494 are almost entirely from electron motion.

495 Ion chambers using fission reaction to convert neutrons are called fission chambers. Fis-
496 sion chambers are frequently used inside nuclear reactor cores. Considering the large amount
497 of energy deposited by fission fragments in the gas, fission chambers have the potential to be
498 operated in pulse mode and to isolate neutron signals from other intense radiations in the
499 core, e.g., gamma rays, by pulse height discrimination. However, pulse mode is not intrinsi-
500 cally suitable for intense in-core radiation due to dead time. To circumvent this issue, in-core
501 fission chambers are designed to collect ionized electrons rapidly for small dead time that
502 accommodates the in-core radiation. One candidate technology is the micro-pocket fission
503 chambers [46] developed at Kansas State University, detailed models of which are developed
504 and described in Chapter 7.

505 **2.2.2 Inorganic Scintillation Detectors**

506 A scintillation detector consists of the scintillator and the photon-detection device. Scin-
507 tillators can be categorized as inorganic, organic, or gaseous. Because the ZnS:Ag-based
508 scintillation detectors considered in this work are the inorganic type, a brief overview of the
509 associated scintillation mechanism is warranted. The scintillation light is weak, and, thus,
510 it is necessary to couple a scintillator with a photon-detection device to convert and amplify
511 the light to measurable electrical signal. Commonly-used photon-detection devices are the
512 traditional photomultiplier tube (PMT) and the more recent silicon photomultiplier (SiPM).
513 For performance, the response of the light sensor should match the emission spectrum of the
514 scintillator.

515 **Inorganic Scintillation Mechanism**

516 When an inorganic scintillator is irradiated, the ionizing particles deposit energy in it and
517 liberate electron-hole pairs. Energy from relaxation and thermalization of charge carriers is

518 released as intrinsic photons, or transfers to activator and causes extrinsic photon emission
519 [8]. The electron-hole pairs can be generated in several ways. The primary electron-hole
520 pairs are excited directly by the ionizing particles. The energetic primary electrons travel
521 through the scintillator lattice and liberate secondary electron-hole pairs. Furthermore, when
522 an outer-shell electron fills the hole, a characteristic X ray or an Auger electron is emitted
523 with energy equals to the difference of the binding energy between the outer-electron and
524 the inner-hole orbitals. The subsequent emissions can be reabsorbed, and more electron-hole
525 pairs are liberated.

526 The electron transition and the associated scintillation mechanism can be explained by
527 energy band theory, as shown in Fig. 2.3. The electrons of an atom exist in discrete energy
528 states. When N identical atoms are arranged to form a crystal, each energy state of an atom
529 splits into N states because, according to the Pauli exclusion principle, two electrons can
530 not have the same quantum number in a molecule. Because the atomic density in a solid is
531 about 10^{22} cm^{-3} , the energy states from splitting are closely spaced in energy (with gap in
532 the order of 10^{-22} eV) and can be considered as *quasi-continuum* [10], i.e., an energy band.

533 The uppermost allowed band filled with electrons is the valence band, below which is
534 the tight-bound band. Above the valence band are the conduction and upper bands, which
535 are empty in a ground-state crystal. An electron can be excited from the valence or the
536 lower tight-bound band to the conduction or upper band and leave a hole in the original
537 band, which forms a free electron-hole pair. Then, the energetic electron loses energy, e.g.,
538 via Coulombic interactions during traveling through the lattice, and drops back to the lower
539 edge of the conduction band E_c . If the energy an electron gained is insufficient, the electron
540 is liberated to the exciton band instead of the conduction (or upper) band, where the upper
541 edge of the exciton band is E_c . In this case, the electron still binds to the respective hole,
542 i.e., this pair diffuses together, and such pair is called an exciton. The energy gap of an
543 exciton is slightly smaller than the band gap energy E_g , which is the difference between the
544 upper edge of the valence band E_v and E_c , as shown in Fig. 2.3. When an electron (from the
545 upper, conduction, or exciton bands) falls back to E_v , photons are emitted. The photons
546 that have energy E_g are reabsorbed by the scintillator. Therefore, the scintillator is usually

547 opaque to its own light. This process is the intrinsic photon emission.

548 To avoid reabsorption, activator is added to the scintillator, which creates energy states
 549 in the band gap. As shown in Fig. 2.3, E_{t0} is the ground state of the activator, and E_{t1} and
 550 E_{t2} are the excited states. A raised electron may fall into the excited states (e.g., E_{t1} and
 551 E_{t2}). When the electron deexcites to E_{t0} , sub-band-gap photon is emitted and not absorbed
 552 by the scintillator. This photon emission is described as extrinsic, i.e., the photons are
 553 from the added activator atoms. The extrinsic photons usually have less energy, or longer
 554 wavelength, than the intrinsic ones.

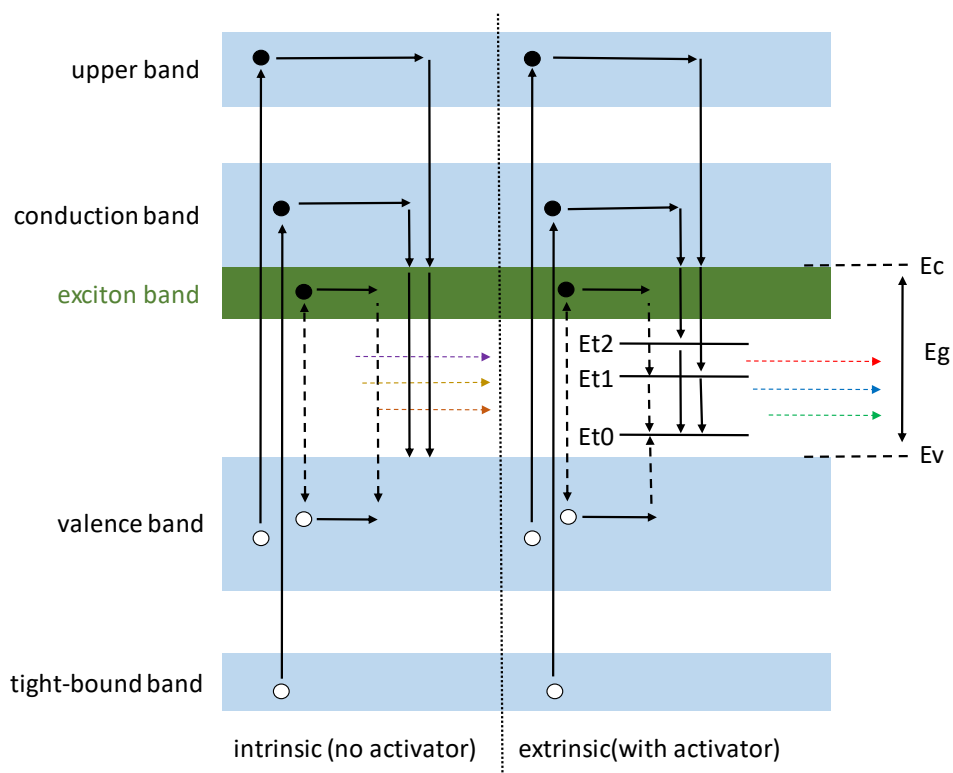


Figure 2.3: Intrinsic and extrinsic scintillation mechanisms, after Ref. [8]. Abbreviations: E_c , conduction band edge; E_v , valence band edge; E_{t0} , activator ground state; E_{t1} and E_{t2} , activator excited states.

555 Only a fraction of the deposited energy is transferred to the extrinsic photons. Part of the
 556 energy ends in thermal form without light emission. If the electrons are excited by gamma
 557 rays, the wavelength at the peak of the incident gamma-ray spectrum differs from that of the
 558 light emission spectrum. This wavelength difference is the Stokes shift [8]. The fraction of the

559 dissipated energy that is converted to the scintillation response is defined as the scintillation
 560 efficiency. Among known inorganic scintillators, NaI:Tl has the highest scintillation efficiency
 561 of about 12% [7]. The scintillation efficiencies of other inorganic scintillators are reported as
 562 fractions respective to the value of NaI:Tl.

563 Photon-Detection Devices

564 The scintillation light is weak, and it has to be amplified by the photon-detection device
 565 for a measurable signal. Two important parameters of a photon-detection device are the
 566 quantum efficiency and the photo-detection efficiency (PDE). The quantum efficiency is the
 567 number of photoelectrons emitted from the photocathode per incident photon, and the PDE
 568 is the overall efficiency of detecting an incident photon.

569 The traditional light sensor used with scintillators is the photomultiplier tube (PMT), the
 570 operational principles of which are shown in Fig. 2.4. The scintillation photons may interact
 571 within the photocathode and produce photoelectrons. Guided by the steering voltage, the
 572 photoelectrons strike the first dynode in the vacuum tube of the PMT and liberate more
 573 electrons. The new electrons undergo the same process in the following dynodes. In the end,
 574 the large number of electrons generate measurable electrical signal at the anode.

575 The total charge produced at the anode is

$$Q = qN_0 \prod_{i=1}^M \bar{g}_i, \quad (2.9)$$

576 where q is the charge of an electron, N_0 is the number of initial photoelectron, M is the
 577 number of dynodes, and \bar{g}_i is the average gain of a dynode. The typical total gain (i.e.,
 578 $\prod_{i=1}^M \bar{g}_i$) of contemporary PMTs ranges from 10^5 to 10^7 [47]. The usual peak quantum
 579 efficiency of PMT is about 25%, and higher value of about 35-40% has been reported [48].

580 Another photon-detection device is the SiPM. A SiPM integrates about 500-4000 tiny
 581 avalanche photodiodes (APDs) per mm^2 on a substrate, which forms a macroscopic unit of
 582 about $6 \text{ mm} \times 6 \text{ mm}$ (or less) [8, 9]. Each APD is connected to a load resistor in series. The

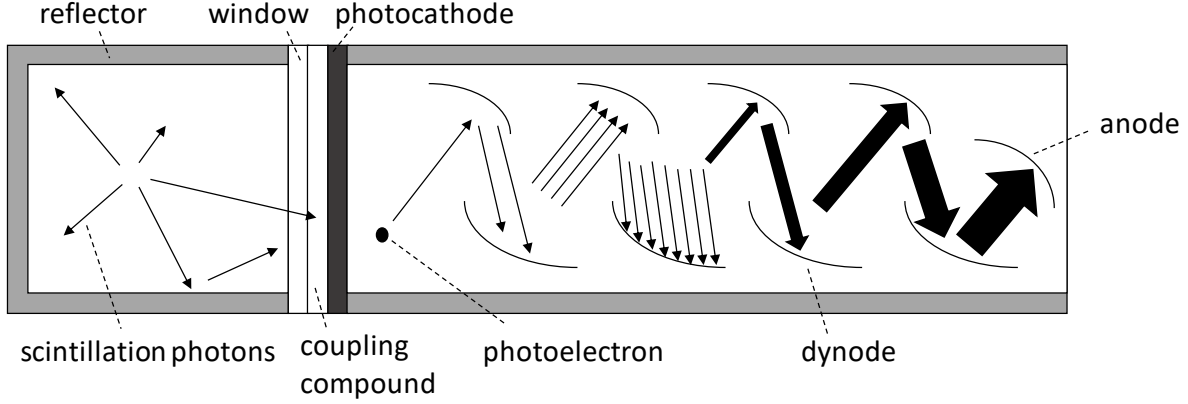


Figure 2.4: A scintillation detector consists of coupled scintillator and PMT, after Ref. [8].

583 voltage across the APD, V_a , is

$$V_a = V - I \times R, \quad (2.10)$$

584 where V is the applied reverse bias voltage across the APD and the resistor, I is the current,
 585 and R is the resistance of the load resistor. The reverse bias voltage is usually 10-20% larger
 586 than the breakdown value [49], and it operates each APD in the Geiger mode. In this mode,
 587 when a photoelectron is produced in an APD, the applied voltage accelerates it to sufficient
 588 energy to create electron avalanche via collisions with bound electrons. From a macro-
 589 scopic view, the semiconductor conducts current. This phenomenon is termed avalanche
 590 breakdown. When the current increases to certain limit, e.g., $10 \mu\text{A}$ [9], due to the series-
 591 connected resistor, the voltage across the APD drops below the breakdown value (as shown
 592 in Eq. (2.10)), then, the avalanche is quenched. The signals of the independent APDs are
 593 summed to measure the light flux.

594 The gain of an APD is in the level of 10^6 [9]. The quantum efficiency of an SiPM is
 595 close to 100%. However, its PDE deteriorates because 1) the detector surface has insensitive
 596 region; 2) only a fraction of photoelectrons can initiate a Geiger discharge; and 3) the pixel
 597 needs recovery time [9]. In general, the PDE of SiPM is better than PMT. Shown in Fig. 2.5
 598 is a comparison between the PDEs of SiPMs to the quantum efficiency of a commercial
 599 PMT, where the peaks are comparable. Furthermore, as of 2018, the blue-sensitive SiPM
 600 has achieved a PDE of 60% around 400 nm [50]. Another attractive feature of SiPMs is its

601 insensitivity to magnetic field, and hence, it is preferred over PMT in applications where
 602 magnetic field exists, e.g., medical imaging and high-energy physics experiments [50].

603 For the TREAT hodoscope, the background gamma rays generate strong Cherenkov
 604 noise in the PMT connected to the Hornyak button. Such noise can be avoided if SiPM were
 605 instead used. Though the gamma rays may still interact with silicon ($Z = 14$), this noise is
 606 relatively easy to discriminate by pulse height.

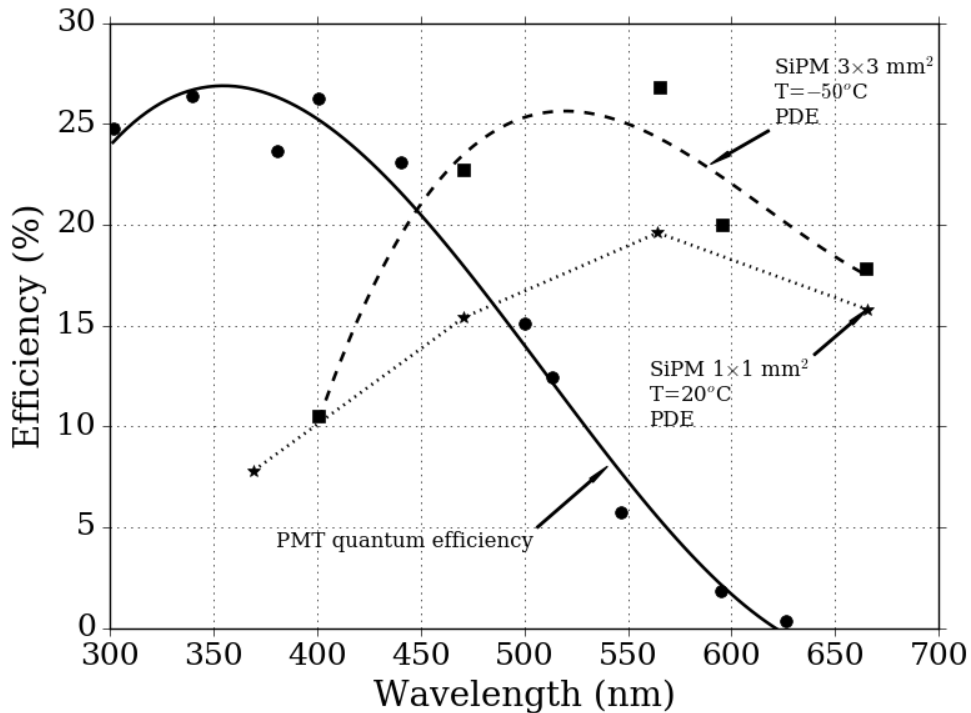


Figure 2.5: Comparison of SiPM PDEs to quantum efficient of PMTs, after Ref. [9].

607 2.2.3 Semiconductor Detectors

608 The electrical conductivity of a semiconductor increases with temperature, which distin-
 609 guishes it from conductors and insulators. The energy gap of a semiconductor is small. For
 610 example, at room temperature, the gap is 1.12 eV for silicon [7], and, hence, electrons can
 611 gain thermal energy to jump from the valence band to the conduction band and leave a hole
 612 in the valence band. As temperature increases, more electrons are excited, which improves
 613 electrical conductivity. Besides the elevated electrons due to temperature, extra electrons

614 are liberated when radiation energy is dissipated, which is termed charge carrier *injection*
 615 [10]. The excess charge carriers can be measured to reflect the deposited energy by radiation,
 616 which is the basis of semiconductor detectors.

617 Semiconductor neutron detectors can be constructed with micro structures to achieve high
 618 efficiency. One notable example is the dual-sided microstructured semiconductor neutron
 619 detector (DS-MSND), which has achieved intrinsic thermal-neutron detection efficiency of
 620 69.2% [42]. As an evolution, the fast-sensitive MSND is considered for the TREAT hodoscope
 621 in this work.

622 **Recombination**

623 The excited electrons may directly fall back to the valence band from the conduction band
 624 and recombine with the holes, which is the *radiative electron recombination*. In practice,
 625 the radiative electron recombination is rare, and the trap-assisted, or the *Shockley-Read-Hall*
 626 (SRH) recombination is more probable [10]. In a semiconductor, defects and impurities,
 627 e.g., *n*- and *p*-type dopings, create trap states in the gap. The charge carriers that transit
 628 through the gap may be captured by the trap states, and the trapped carriers may also be
 629 re-emitted, e.g., electrons to the conduction band and holes to the valence band. The SRH
 630 recombination affects the time during which an electron stays in the conduction band (or a
 631 hole in the valence band), the average of which is the *electron lifetime* τ_n (or the hole lifetime
 632 τ_p).

633 **Energy Resolution**

634 Semiconductor detectors have good energy resolution and are frequently used in spectroscopy
 635 measurement. The energy resolution R is defined as [7]

$$R = \frac{\Gamma}{E_0} \propto \sqrt{\omega F}, \quad (2.11)$$

636 where Γ is the full width at half maximum (FWHM) of a detector pulse from dissipated
 637 energy E_0 , ω is the average energy needed to produce a pair of charge carriers, and F is the

638 *fano factor*, defined as

$$F = \frac{\sigma_N^2}{N}, \quad (2.12)$$

639 where N is the number of charge-carrier pairs produced, and σ_N is the standard deviation
640 of N .

641 For a semiconductor, an energy of 3 to 5 eV is required to create an electron-hole pair. As
642 a comparison, for a gas-filled counter, it takes about 25 to 40 eV to create an electron-ion pair,
643 and for a scintillator-PMT detector, 100 eV to 1 keV is needed to produce a photoelectron.
644 Hence, more charge carriers are produced in semiconductor detector per deposited energy,
645 which decreases the statistical error and provides better energy resolution.

646 ***pn* junction**

647 Semiconductors are doped with donor or acceptor atoms to increase electrical conductivity.
648 A donor atom has more than four valence electrons, while an acceptor atom has fewer than
649 four electrons. Semiconductors with donor (acceptor) atoms are *n*-type (*p*-type), and the
650 conductivity is mainly due to electrons (holes). The doping effects can be explained by the
651 energy band theory, as shown in Fig. 2.6. The excess electron of a donor sits in an energy
652 level close to the conduction band. A small amount of energy, e.g., thermal energy at room
653 temperature, can elevate it into the conduction band. The acceptor atom creates an energy
654 level close to the valence band. An electron of the semiconductor atom can move to this
655 level with a small amount of energy, and a hole is created in the valence band. In both cases,
656 more charge carriers are produced per deposited energy than the un-doped semiconductor,
657 and the conductivity increases.

658 Semiconductor detectors can be designed as *pn*-junction diodes, *pin*-junction diodes,
659 Schottky diodes, resistive detectors, and photoconductors, but the emphasis here is on the
660 *pn* junction, which is used for the present generation of MSNDs [51]. A *pn* junction is usually
661 formed by transforming one end of a certain type semiconductor into another one, e.g., the
662 MSNDs are fabricated by diffusing *p*-type contacts into *n*-type silicon [51].

663 A *n*- or *p*-type semiconductor is neutral. When a *pn* junction is formed, electrons dif-

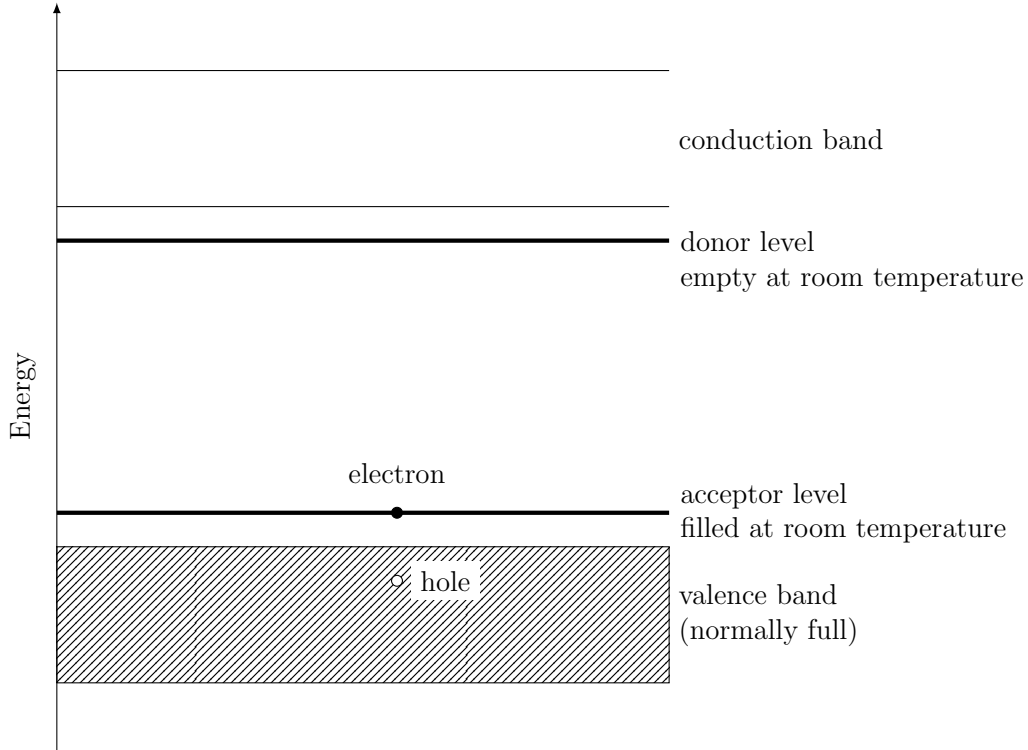


Figure 2.6: Semiconductor doping effects.

664 fuse from the high-concentration n -type to the p -type side, and holes move in the opposite
 665 direction. The heterogeneous electron and hole concentrations, i.e., space charge, create
 666 an internal electric field, which acts against the diffusing process. When diffusion is com-
 667 pensated by drift due to the electric field, equilibrium is established. The width of the
 668 space-charge region is called the *depletion* or *active* region (usually, it is expanded by an
 669 external reverse bias). If electron-hole pairs are generated by radiation in this region, the
 670 charge carriers are swept away under the electric field, which is measured as a signal.

671 The width of the space-charge region can be derived from the Poisson equation (Eq. (2.2))
 672 [10]. In one-dimension, it becomes (assuming uniform permittivity)

$$\frac{d^2\psi}{dx^2} = -\frac{\rho(x)}{\epsilon} = \frac{q_e}{\epsilon}(N_A^- + n - N_D^+ - p). \quad (2.13)$$

673 N_A^- and N_D^+ are charge densities introduced by acceptor and donor concentrations, respec-
 674 tively. An acceptor atom is like a negative ion when it receives an extra electron, and a donor

675 atom loses an electron and becomes an ion. Without radiation, n and p are electron and hole
676 concentrations introduced by temperature, diffusion, and drift. At n -type side, the charge
677 density is mainly dominated by the doping concentration N_D^+ , and at 300K, $N_D^+ \simeq N_D$, i.e.,
678 all the donors lose electrons and become ions. The same approximation applies to the p -type
679 side. Hence,

$$\frac{d^2\psi}{dx^2} \simeq \begin{cases} -q_e N_D / \epsilon, & 0 \simeq x \simeq x_n; \\ q_e N_A / \epsilon, & x_p \simeq x \simeq 0, \end{cases} \quad (2.14)$$

680 where a schematic is shown in Fig. 2.7. Here, x_p is the coordinate of the left edge of the
681 p -type side with a negative value.

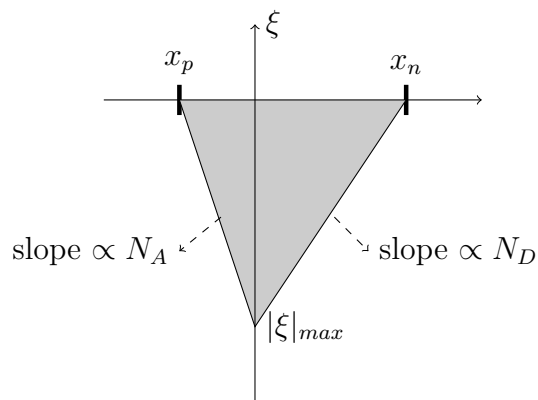


Figure 2.7: Distribution of the electric field in the depletion region of the pn junction, after Ref. [10].

682 The generated electric field ξ can be computed by

$$\xi = -\nabla\psi = - \int dx \frac{d^2\psi}{dx^2}. \quad (2.15)$$

683 In the n -type side,

$$\xi(x) = - \int dx \left(-q_e \frac{N_D}{\epsilon} \right) = \frac{q_e N_D x}{\epsilon} + C_1. \quad (2.16)$$

684 Similarly, in the p -type side,

$$\xi(x) = - \int dx \left(q_e \frac{N_A}{\epsilon} \right) = -\frac{q_e N_A x}{\epsilon} + C_2. \quad (2.17)$$

685 C_1 and C_2 can be determined by the boundary conditions that $\xi(x_n) = \xi(x_p) = 0$. Then,

$$\xi(x) = \begin{cases} q_e N_D (x - x_n) / \epsilon, & 0 \simeq x \simeq x_n; \\ q_e N_A (x_p - x) / \epsilon, & x_p \simeq x \simeq 0. \end{cases} \quad (2.18)$$

686 The electric fields in both regions are negative, which corresponds to the direction pointing
687 from the n -type end to the p -type end. At $x = 0$, the electric field is continuous, which
688 requires

$$-N_D x_n = N_A x_p, \quad (2.19)$$

689 i.e., the space-charge width in one side is inversely proportional to its doping concentration.

690 In addition, the maximum magnitude of the electric field is at $x = 0$, i.e.,

$$\xi_{max} = -\frac{q_e N_D x_n}{\epsilon} = \frac{q_e N_A x_p}{\epsilon}. \quad (2.20)$$

691 The potential difference across the depletion region is

$$\begin{aligned} \Delta\psi &= -\int_{x_p}^{x_n} dx \xi(x) \\ &= -\int_{x_p}^0 \frac{q_e N_A (x_p - x)}{\epsilon} dx - \int_0^{x_n} dx \frac{q_e N_D (x - x_n)}{\epsilon} dx \\ &= \frac{q_e}{2\epsilon} (N_A x_p^2 + N_D x_n^2). \end{aligned} \quad (2.21)$$

692 Based on Eq. (2.19),

$$\begin{aligned} N_A x_p^2 &= \frac{N_D^2 x_n^2}{N_A} \\ N_D x_n^2 &= \frac{N_A^2 x_p^2}{N_D}. \end{aligned} \quad (2.22)$$

693 Upon substitution of Eq. (2.22) into Eq. (2.21), the widths x_n and x_p can be expressed as

$$\begin{aligned} x_n &= \sqrt{\frac{2\epsilon\Delta\psi}{q_e} \frac{N_A}{N_D(N_D + N_A)}} \\ x_p &= -\sqrt{\frac{2\epsilon\Delta\psi}{q_e} \frac{N_D}{N_A(N_D + N_A)}}. \end{aligned} \quad (2.23)$$

694 Then, the total width W is

$$W = x_n - x_p = \sqrt{\frac{2\epsilon\Delta\psi}{q_e} \frac{N_A + N_D}{N_A N_D}}. \quad (2.24)$$

695 If an external reverse bias voltage V is applied, which is usually much larger than the build-in
696 potential difference $\Delta\psi$, the total width can be approximated as

$$W = \sqrt{\frac{2\epsilon(\Delta\psi + V)}{q_e} \frac{N_A + N_D}{N_A N_D}} \simeq \sqrt{\frac{2\epsilon V}{q_e} \frac{N_A + N_D}{N_A N_D}}. \quad (2.25)$$

697 If the doping of one side is much larger than the other, the width can be further simplified
698 to

$$W \approx \sqrt{\frac{2\epsilon V}{q_e N_l}}, \quad (2.26)$$

699 where N_l is the smaller doping concentration. When energy is dissipated in this depletion
700 region, electron-hole pairs are produced and drifted under the bias. The resulting charge
701 carriers are extracted from the semiconductor through an ohmic contact. Then, the signal
702 is amplified, measured, and recorded by counting electronics.

703 In a semiconductor detector, the electron drift velocity is about two to three times than
704 that of a hole [7]. In addition, the depletion region is usually in mm. Thus, both carriers
705 can be collected in the order of 10^{-7} s. This feature is different from a gas-filled ionization
706 chamber, in which the drift velocity of electrons is thousands of times larger than the ion
707 velocity. Therefore, in a gas chamber, pulses are truncated when electrons are collected.

708 **2.3 Summary**

709 In this chapter, common neutron converting reactions and the signal-forming mechanisms
710 of gas-filled, scintillation, and semiconductor neutron detectors are reviewed, which cover
711 fundamental physics of the neutron detectors evaluated in this work. The Hornyak buttons
712 and the variants are scintillation, fast-neutron detectors mainly based on the proton-recoil
713 reaction. The fast-sensitive MSNDs convert fast neutrons by the proton-recoil or the fission
714 reaction. The MPFDs are gas-filled fission chambers. In the next chapter, the Monte Carlo
715 simulation to evaluate the neutron detectors will be presented.

716 Chapter 3

717 Monte Carlo Simulation

718 The Monte Carlo method has been widely used to simulate radiation transport, and different
719 codes have been developed, e.g., GEometry ANd Tracking (Geant4) and Monte Carlo N-
720 Particle (MCNP). In this chapter, the theoretical foundation of the Monte Carlo method
721 and the general flow of a Monte Carlo simulation of particle transport are presented. Then,
722 a typical structure used in this work to build Geant4 applications is introduced. Following
723 this structure, an example problem is modeled in Geant4 and MCNP to compare the inputs.
724 In addition, a summary is given of the optical physics models in Geant4, which are needed
725 to simulate scintillation detectors.

726 3.1 Monte Carlo Basis

727 The theoretical foundations of the Monte Carlo method are the *law of large numbers* and the
728 *central limit theorem*. The law of large numbers states that, with infinite trials, the sampled
729 frequency reveals the underlying probability distribution, and the sample mean (\bar{z}) equals
730 the true (population) value $\langle z \rangle$. Consider a definite integral, which can be defined formally
731 as the sum

$$\frac{1}{N} \sum_{i=1}^N z(x_i) \equiv \bar{z} \stackrel{N \rightarrow \infty}{\equiv} \langle z \rangle \equiv \int_a^b z(x) f(x) dx, \quad (3.1)$$

732 provided that the mean exists, the variance is bounded, and x_i are sampled from the prob-
733 ability distribution function (PDF) $f(x)$. It is, of course, impossible to simulate an infinite
734 number of trials. When a large number of histories are simulated, the statistical error is given
735 by the central limit theorem, which states that $\frac{|\bar{z} - \langle z \rangle|}{\sigma(z)/\sqrt{N}}$ follows a unit normal distribution,
736 i.e.,

$$\text{Prob} \left\{ \frac{|\bar{z} - \langle z \rangle|}{\sigma(z)/\sqrt{N}} \leq \lambda \right\} = \frac{1}{\sqrt{2\pi}} \int_{-\lambda}^{\lambda} e^{-u^2/2} du, \quad (3.2)$$

737 where $\sigma(z)$ is the true standard deviation of z . Typically, the true standard deviation $\sigma(z)$
738 is approximated by the standard deviation of the sample, $s(z)$, defined as

$$s(z) = \sqrt{\frac{N}{N-1}(\overline{z^2} - \bar{z}^2)}, \quad (3.3)$$

739 which converts Eq. (3.2) into

$$\text{Prob} \left\{ \bar{z} - \lambda \frac{s(z)}{\sqrt{N}} \leq \langle z \rangle \leq \bar{z} + \lambda \frac{s(z)}{\sqrt{N}} \right\} \simeq \frac{1}{\sqrt{2\pi}} \int_{-\lambda}^{\lambda} e^{-u^2/2} du. \quad (3.4)$$

740 Equation 3.4 implies the standard deviation of the sample is inverse proportional to square
741 root of the number of histories, i.e.,

$$s(z) \propto \frac{1}{\sqrt{N}}. \quad (3.5)$$

742 In addition, $\frac{s(z)}{\sqrt{N}}$ is the standard error of the sample mean \bar{z} , i.e.,

$$s(\bar{z}) \equiv \frac{s(z)}{\sqrt{N}} = \sqrt{\frac{\overline{z^2} - \bar{z}^2}{N-1}}. \quad (3.6)$$

743 The right hand side of Eq. (3.4) is the confidence coefficient, and its truncated percentage
744 form is the confidence limit. The parameter λ defines the width of the distribution in number
745 of standard deviations of the sample mean, i.e., $s(\bar{z})$. For $\lambda = 1, 2$, and 4 , the confidence
746 limits are 68.27%, 95.45%, and 99.99%, respectively, which means, e.g., for $\lambda = 1$, the true
747 value $\langle z \rangle$ has a probability of 68.27% to fall into the interval of $[\bar{z} - s(\bar{z}), \bar{z} + s(\bar{z})]$.

748 3.2 Flow of Monte Carlo Simulation

749 A particle interacts with a material region following different probability distributions, which
750 are used to sample parameters in a Monte Carlo simulation that include the distance traveled
751 before a next collision, the nuclide with which an interaction occurs at a collision site, and the
752 specific reaction that occurs. While the behaviors of individual particles vary, according to
753 the law of large numbers, the average tally from many individual particles (called “histories”)
754 converges to the true average behavior.

755 In a continuous-energy, Monte Carlo simulation¹, particles are tracked from birth to
756 death, during which the tallies are accumulated. The simulation starts with sampling the
757 initial condition, e.g., energy, position, and direction, of the source particle from user input.
758 Then, the distance to the next collision is sampled from the total macroscopic cross section
759 of the material Σ_t by

$$d = -\frac{\ln \xi}{\Sigma_t}, \quad (3.7)$$

760 where ξ is a pseudorandom number sampled from uniform distribution on $[0, 1)$. If the
761 sampled distance exceeds the distance to the global boundary, i.e., the particle streams
762 out of the volume of interest, the particle is killed. If the passed boundary is not global,
763 the particle is moved to the boundary and placed inside the neighbor volume, and a new
764 distance is sampled. If the distance is within the same volume, a collision occurs. Whether
765 the particle passes the boundary or collides, the above process is a Monte Carlo step.

766 The collision nuclide is sampled based on the discrete probability distribution

$$P(i) = \frac{\Sigma_{t,i}}{\Sigma_t}, \quad (3.8)$$

767 where $\Sigma_{t,i}$ is the macroscopic cross section of nuclide i . The undergoing reaction with the
768 nuclide is likewise sampled from

$$P(j) = \frac{\sigma_j}{\sigma_t}, \quad (3.9)$$

¹The sampling of multi-group simulation is slightly different and not covered here.

769 where σ_j and σ_t are the microscopic cross sections for reaction j and the nuclide. If scattering
770 occurs, the outgoing angle and energy of the particle are sampled from corresponding distri-
771 butions, and the process from Eq. (3.7) is repeated. If the particle is absorbed, it is killed.
772 If secondary particles are generated, e.g., fission and (n, xn) reactions, they are banked for
773 later tracking. The cross sections and algorithms to simulate different reactions are usually
774 stored in a specific data format, e.g., the ACE data produced by NJOY are used by MCNP,
775 Serpent, and OpenMC, and the G4NDL neutron data library is used in Geant4. During the
776 tracking, the tally and square of the tally are accumulated to compute the mean (Eq. (3.1))
777 and variance (Eq. (3.3)). When the tracking of particles is completed, i.e., the particles are
778 absorbed or stream out of the global boundary, the simulation is finished.

779 3.3 Overview of Geant4

780 Geant4 is a toolkit to simulate passage of particles through matter [32]. It is open-source and
781 written in the object-oriented programming language C++. The code was first released for
782 modeling of high-energy physics (HEP) experiments in December 1998 [52], and now, it has
783 been extended to applications in medical physics, nuclear engineering, and reactor physics
784 [53].

785 The accuracy of Geant4 has been improved with subsequent releases. Specific improve-
786 ments include an update of the neutron data library and the incorporation of thermal elas-
787 tic scattering (i.e., $S(\alpha, \beta)$) laws. In previous versions, the Geant4 neutron data library
788 (G4NDL) was based on 9 different databases, but since version 9.5, G4NDL is solely built on
789 the Evaluated Nuclear Data Files (ENDF/B-VI and VII) [34]. In addition, the $S(\alpha, \beta)$ data
790 matrix has been adopted since version 8.2 [54] to provide the double-differential cross sec-
791 tion of thermal-neutron scattering, i.e., the probability that a neutron scatters into certain
792 final-state energy and angle.

793 Geant4 has several useful features. It can simulate optical physics, which are needed
794 to evaluate scintillation detectors. It has the fission fragment generator (FFG) to sample
795 and to track fission fragments [34]. In contrast, an approximation incorporated in MCNP

796 is to assume the fission energy is deposited at the location of the fission event. The FFG
797 simplifies the evaluation of fission-based detectors, where the deposited energy by fission
798 fragments outside the fission volume is of interest.

799 A Geant4 model can be built directly with C++ code (the "batch mode") or by using
800 the more convenient macro commands in a script-like input. Macro commands are text-
801 format equivalents to the corresponding C++ features. For instance, the macro command,
802 `/run/beamOn`, is equivalent to the `BeamOn` function defined in the Geant4 run manager class.
803 Different macro commands for important Geant4 setting functions have been predefined via
804 the "intercoms" category of Geant4 source code. If the functions without corresponding
805 macro commands are needed (which is common), the Geant4 application can be developed
806 using a combination of C++ code and macro commands. In such a case, the macro com-
807 mands are listed in a text file passed to Geant4 executable via the command line. The
808 Geant4 applications in this work were developed in batch mode assisted by macro files.

809 **3.4 Code Structure of Geant4 Application**

810 The code structure of Geant4 applications developed in this work is shown in Fig. 3.1, to-
811 gether with corresponding MCNP input cards. A Geant4 simulation consists of three manda-
812 tory user initialization classes: the detector construction class, the physics list class, and the
813 action initialization class. The action initialization class coordinates the mandatory primary
814 generator class and the optional user run, event, and step action classes. The customized
815 classes inherit from respective base classes defined in Geant4 source ² to communicate with
816 the kernel via defined functions.

817 **3.4.1 Detector Construction**

818 A customized detector construction class inherits from the `G4VUserDetectorConstruction`
819 class to define geometry and material in the `Construct` function. This class is equivalent to

²Names of the Geant4 source classes are with prefix `G4`.

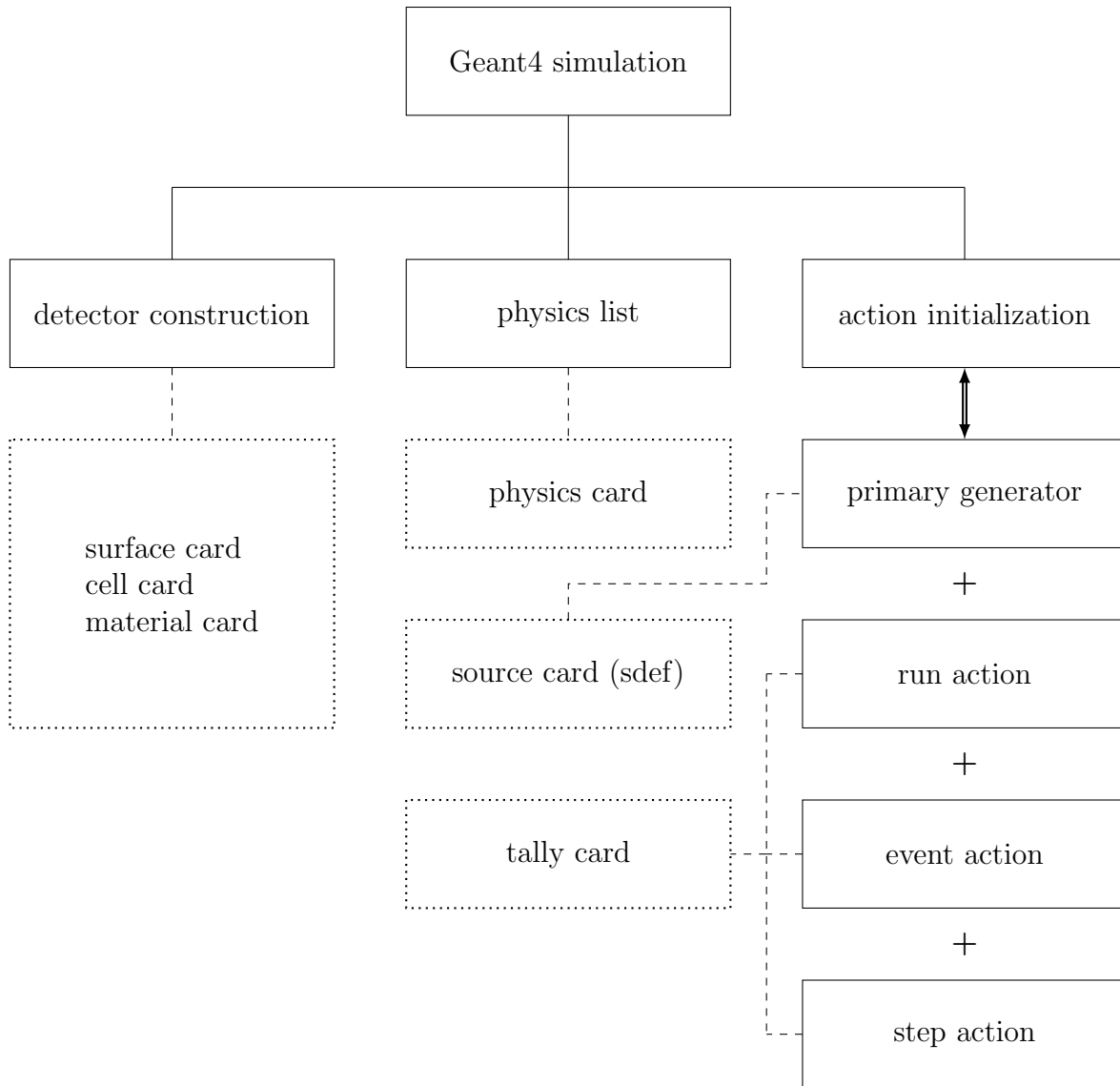


Figure 3.1: Basic structure of a Geant4 simulation (solid boxes), compared to MCNP input cards (dotted boxes).

820 the surface, cell, and material cards in MCNP. The Geant4 geometry is constructed directly
 821 via volumes, which differs from the MCNP syntax that surfaces are first defined, and volumes
 822 are described using surrounding surfaces. The geometry construction in Geant4 starts with
 823 defining a world volume, whose boundary and coordinate system are global. Then, daughter
 824 volumes are defined and put into the world volume. A daughter volume may contain the
 825 “grand-daughter” volumes, and this hierarchy continues as necessary.

826 A volume is defined via solid, logical volume, and physical volume classes. The solid

827 classes implement the Constructive Solid Geometry (CSG) to model different shapes. A
828 solid is filled with material to construct the logical volume. The logical volume has its
829 own coordinate system, and it is placed into the coordinate system of its mother logical
830 volume via the definition of a physical volume, which specifies the rotation matrix and the
831 translation vector. The world volume does not have a mother volume, and its coordinate
832 system is global.

833 A material in Geant4 is defined by successively defining the isotopes and elements. Iso-
834 topes are first defined to constitute an element with respective isotope abundances, e.g.,
835 enriched uranium. Different elements are used to define a material with corresponding ele-
836 ment fractions. For convenience, common materials are predefined in the internal material
837 database, which is derived from the National Institute of Standards and Technology (NIST).
838 This database consists of sub-libraries for single-element materials with natural isotope abun-
839 dance, NIST compounds, high energy physics and nuclear materials, space materials, and
840 bio-chemical materials, respectively.

841 **3.4.2 Reference Physics List**

842 The physics list class describes the particles and the physical processes associated with each
843 particle to be simulated in the calculation. Validated reference physics lists [55] for different
844 applications are provided, and recommendations for which lists to use for which applications
845 are provided. As an example, for neutrons under 20 MeV, the high-precision (HP) lists are
846 recommended, e.g., the QGSP BERT HP reference physics list.

847 The reference physics lists exclude optical physics, which may be needed to simulate
848 scintillation detectors. For this work, a modified physics list is used based on examples with
849 optical physics included with Geant4 source code, which demonstrates how to append the
850 optical physics to the selected reference physics list.

851 **3.4.3 Action Initialization**

852 In the action initialization class, the mandatory primary generator class and the optional user
853 action classes are initialized. In the primary generator class, a concrete class derived from the
854 base `G4VPrimaryGenerator` class is initialized to define source particles. Two concrete gener-
855 ator classes are provided, the `G4ParticleGun` and the `G4GeneralParticleSource` (GPS).
856 The GPS class has all the functionality of `G4ParticleGun` and is more advanced. The GPS
857 class defines a complete list of macro commands to define a variety of source particles. These
858 generator classes can emit multiple source particles in a source event. Each source particle
859 can have its own characteristic. As a comparison, in MCNP, a history typically consists of
860 one source particle.

861 Objects of the optional user run, event, and step action classes can be linked to accumu-
862 late tallies. At the end of a step, the inherited `UserSteppingAction` function defined in the
863 `G4UserSteppingAction` class is called to give access to basically all the information during
864 this step, e.g., the total deposited energy along the step and coordinates of the start and the
865 end step points. The information from all steps in a source event can be summed to a vari-
866 able defined in the user event action to compute the event-specific tally. The event-specific
867 tally can be further accumulated to the variables defined in the user run action to compute
868 average and variance.

869 To illustrate the code structure of a Geant4 application and its similarities to (or differ-
870 ences from) typical MCNP models, both Geant4 and MCNP were used to model a simple
871 source-detector system. The source code and inputs are provided in Appendix A.

872 **3.5 Geant4 Optical Physics**

873 The optical physics are constructed in the `G4OpticalPhysics` class, which is used to build the
874 modified physics list as stated in Section 3.4.2. This class consists of seven optical processes
875 that apply to the optical photon type, which is an independent particle type separate from
876 the higher energy gamma photons that is used to simulate the wave-like electromagnetic

877 radiation. The seven optical processes are Cherenkov³, scintillation, wave length shifting,
878 optical absorption, Rayleigh scattering, Mie scattering, and optical boundary process. The
879 first three are optical generation processes, and the last four are optical tracking processes.
880 The Cherenkov and scintillation processes are implemented in the `electromagnetic/xrays`
881 category, and the other five processes belong to the `optical` category in the Geant4 source
882 tree. To simulate the scintillation detectors in this work, the optical absorption, the optical
883 boundary, the scintillation, and the Cherenkov processes are of interest.

884 Polarization of optical photon must be specified for correct simulation of optical physics.
885 The polarizations of the secondary optical photons are sampled by the kernel, i.e., from
886 either the Cherenkov or the scintillation processes. If the optical photons are the source
887 particles, the polarizations need to be specified by the user.

888 While algorithms for optical-photon transport are implemented, optical properties need
889 to be supplied by the user. The optical physics are simulated only if optical processes
890 are included in the physics list and the associated optical properties are provided. An
891 optical property can be specified as a constant or as a function of energy. The majority of
892 the non-constant optical properties depend on the optical photon energy, and the particle-
893 dependent scintillation yields also depend on the deposited energy. An example in Geant4
894 is the variable that defines the light yield for protons named `PROTONSCINTILLATIONYIELD`.
895 In the classes that implement optical processes, the `GetConstProperty` function is called
896 to find the associated constant optical properties, and the `GetProperty` function is invoked
897 to locate the needed energy-dependent optical properties. The associated optical properties
898 with each optical process are summarized in Table 3.1.

899 3.5.1 Optical Absorption Process

900 The optical absorption process is implemented in the `G4OpAbsorption` class. It simulates the
901 bulk absorption (compared to the surface absorption detailed later) when an optical photon
902 travels in a material. This process reads the energy-dependent optical absorption length

³The spelling of *Cerenkov* is used in Geant4 source code. However, the writing guidelines published by CERN [56] suggest the spelling *Cherenkov*, which is adopted here.

Table 3.1: Summary of the optical properties read by each optical process. Properties with superscript c are constants, and others are functions of optical photo or deposited energy. Data are extracted from the Geant4 source code.

Optical process	Optical property	Description
absorption	ABSLENGTH	mean free path of optical absorption
boundary process	RINDEX ^S	surface refractive index (RI) of back-painted finishes [57]
	RINDEX	material refractive index
	REFLECTIVITY	probability for an optical photon to be reflected or refracted at a surface
	REALRINDEX	real part of RI to compute reactivity of a dielectric-metal surface
	IMAGINARYRINDEX	imaginary part of RI to compute reactivity of a dielectric-metal surface
	EFFICIENCY	probability of detecting an optical photon at a surface
	TRANSMITTANCE	refraction probability (optional)
	SPECULARLOBECONSTANT	probability of specular lobe reflection in a surface reflection event
	SPECULARSPIKECONSTANT	probability of specular spike reflection in a surface reflection event
	BACKSCATTERCONSTANT	probability of backscatter reflection in a surface reflection event
	GROUPVEL	final velocity of a refracted optical photon
SURFACEROUGHNESS ^C	used to sample the probability of Lambertian reflection	
Cherenkov	RINDEX	refractive index
scintillation	FASTCOMPONENT	scintillator emission spectrum of the fast component
	SLOWCOMPONENT	scintillator emission spectrum of the slow component
	PROTONSCINTILLATIONYIELD	scintillation yield by proton
	DEUTERONSCINTILLATIONYIELD	scintillation yield by deuteron
	TRITONSCINTILLATIONYIELD	scintillation yield by triton
	ALPHASCINTILLATIONYIELD	scintillation yield by alpha
	IONSCINTILLATIONYIELD	scintillation yield by carbon ion
	ELECTRONSCINTILLATIONYIELD	scintillation yield by electron
	SCINTILLATIONYIELD ^C	number of optical photons per unit deposited energy
	RESOLUTIONSCALE ^C	scaler characterizing fluctuation of emitted optical photon number
	FASTTIMECONSTANT ^C	decay time constant of fast component
	FASTSCINTILLATIONRISETIME ^C	rise time of fast component
	SLOWTIMECONSTANT ^C	decay time constant of slow component
SLOWSCINTILLATIONRISETIME ^C	rise time of slow component	
YIELDRATIO ^C	relative strength of fast component	
Rayleigh scattering	RAYLEIGH	mean free path before Rayleigh scattering
	RINDEX	reflective index (RI)
	ISOTHERMAL_COMPRESSIBILITY ^C	compressibility
	RS_SCALE_FACTOR ^C	optional scaler for the Rayleigh scattering length
Mie scattering	MIEHG	mean free path of Mie scattering
	MIEHG_FORWARD ^C	average cosine of the forward angle
	MIEHG_BACKWARD ^C	average cosine of the backward angle
	MIEHG_FORWARD_RATIO ^C	ratio factor between the forward angle and backward angle
WLS	WLSCOMPONENT	relative emission spectrum
	WLSABSLENGTH	absorption length
	WLSMEANNUMBERPHOTONS ^C	mean number of secondary OPs following Poisson distribution
	WLSTIMECONSTANT ^C	time delay between absorption and re-emission

903 (ABSLENGTH), which defines the mean free path of an optical photon in a specific material.
904 This process is needed, for example, to simulate optical transport through ZnS(Ag), which
905 absorbs its scintillation light.

906 3.5.2 Optical Boundary Process

907 The optical boundary process is implemented in the `G4OpBoundaryProcess` class. This
908 process simulates the behavior of an optical photon at the boundary between two different
909 materials. An optical photon can be absorbed, reflected, or refracted, sampling of which
910 depends on the optical surface property. An optical surface is defined by its model, finish,
911 type, and the parameter σ_α , which defines surface roughness. A model is the algorithm to
912 sample the optical boundary process, and the `glisur`, `unified`, LUT (look-up-table) and
913 `dichroic` models are provided. The unified model is used in the DETECT program [58],
914 and it applies to the dielectric-dielectric surface. This model was adopted for all simulations
915 performed as part of the present work.

916 The available surface finishes are listed in Table 3.2. For this work, the `polished`,
917 `polishedfrontpainted`, and `ground` finishes were used. For a ground surface, σ_α is used
918 to sample the polar angle ϑ between a virtual facet and the physical average surface, i.e., ϑ
919 follows a normal distribution, the mean and standard deviation of which are zero and σ_α ,
920 respectively. The azimuthal angle ψ is uniformly sampled from zero to 2π . Then, the solid
921 angle Ω are computed as

$$\Omega = \mathbf{i} \sin \vartheta \cos \psi + \mathbf{j} \sin \vartheta \sin \psi + \mathbf{k} \cos \vartheta. \quad (3.10)$$

922 The solid angle and the normal of the average physical surface are used to calculate the
923 normal of the facet, and the boundary processes are with respect to the sampled facet. The
924 virtual facet is not defined, and only its normal vector is sampled on-the-fly. As a comparison,
925 the physical average surface exists in the tracking geometry, i.e., the surrounding surface of
926 a volume defined in the detector construction class.

927 The supported surface types are dielectric-metal, dielectric-dielectric, dielectric-LUT
928 (dielectric-Look-Up-Table interface), dielectric-dichroic (dichroic filter interface), firsov (for
929 Firsov process), and xray (for x-ray mirror process). The dielectric-dielectric type was used
930 for this work because the PMMA and ZnS(Ag) are dielectric materials.

Table 3.2: Optical surface finishes in Geant4. Data are extracted from the Geant4 source code.

Finish	Description
polished	smooth perfectly polished surface
polishedfrontpainted	smooth top-layer (front) paint
polishedbackpainted	same is 'polished' but with a back-paint
ground	rough surface
groundfrontpainted	rough top-layer (front) paint
groundbackpainted	same as 'ground' but with a back-paint
polishedlumirrorair	mechanically polished surface, with lumirror
polishedlumirrorglue	mechanically polished surface, with lumirror and meltmount
polishedair	mechanically polished surface
polishedteflonair	mechanically polished surface, with teflon
polishedtioair	mechanically polished surface, with tio paint
polishedtyvekair	mechanically polished surface, with tyvek
polishedvm2000air	mechanically polished surface, with esr film
polishedvm2000glue	mechanically polished surface, with esr film and meltmount
etchedlumirrorair	chemically etched surface, with lumirror
etchedlumirrorglue	chemically etched surface, with lumirror and meltmount
etchedair	chemically etched surface
etchedteflonair	chemically etched surface, with teflon
etchedtioair	chemically etched surface, with tio paint
etchedtyvekair	chemically etched surface, with tyvek
etchedvm2000air	chemically etched surface, with esr film
etchedvm2000glue	chemically etched surface, with esr film and meltmount
groundlumirrorair	rough-cut surface, with lumirror
groundlumirrorglue	rough-cut surface, with lumirror and meltmount
groundair	rough-cut surface
groundteflonair	rough-cut surface, with teflon
groundtioair	rough-cut surface, with tio paint
groundtyvekair	rough-cut surface, with tyvek
groundvm2000air	rough-cut surface, with esr film
groundvm2000glue	rough-cut surface, with esr film and meltmount

931 When an optical surface is defined, it can be assigned to the physical surface of a defined
932 volume as a *skin surface* or a *border surface*. The optical properties of a skin surface are
933 used to simulate the optical boundary processes for photons coming from both sides of the
934 physical surface. The border surface is one-way transport. Two border surfaces can be used
935 to describe different optical properties of the two faces of one physical surface, respectively.
936 For example, two border surfaces can be used to simulate a box with an inner surface painted

937 black and an outer surface painted white. The optical photons coming from outside the box
938 are reflected, and the ones coming from inside the box are absorbed.

939 An optical photon can be reflected, refracted (transmitted), or absorbed at the boundary.
940 The probability that an optical photon is not absorbed at the surface is defined via the
941 REFLECTIVITY parameter of the optical surface. If an optical photon is not absorbed, it is
942 reflected at a painted surface. At other surfaces, the optical photon that survives is reflected
943 or refracted.

944 Reflection and refraction at a polished surface are illustrated in Fig. 3.2. The reflection
945 angle θ_r equals the incident angle θ_i . The refracted angle θ_t is calculated by the Snell's law,
946 i.e.,

$$n_1 \sin \theta_i = n_2 \sin \theta_t, \quad (3.11)$$

947 where n_1 and n_2 are the refractive indices of the two materials. The reflection probability R
948 for an optical photon with incident angle θ_i is [58]

$$R = \frac{1}{2} \left[\frac{\sin^2(\theta_i - \theta_t)}{\sin^2(\theta_i + \theta_t)} + \frac{\tan^2(\theta_i - \theta_t)}{\tan^2(\theta_i + \theta_t)} \right], \quad (3.12)$$

949 and the refraction probability T is

$$T = 1 - R. \quad (3.13)$$

950 The reflection and refraction probabilities also apply to a ground surface except that the
951 angles are defined with respect to the sampled micro facet.

952 If an optical photon is sampled to be reflected at a ground surface using the unified
953 model, the reflection type is further sampled to be specular spike, specular lobe, backscatter,
954 or Lambertian [57, 59]. The specular spike reflection is with respect to the physical average
955 of the ground surface, as shown in Fig. 3.2. The specular lobe reflection is similar to specular
956 spike except that it is with respect to the sampled facet. These two specular reflections are
957 implemented together in the `G4OpBoundaryProcess` class using respective surface normal
958 vectors. In the backscatter reflection, the optical photon is reflected back to the incident
959 direction. In the Lambertian reflection, the optical photon can be reflected into any direction

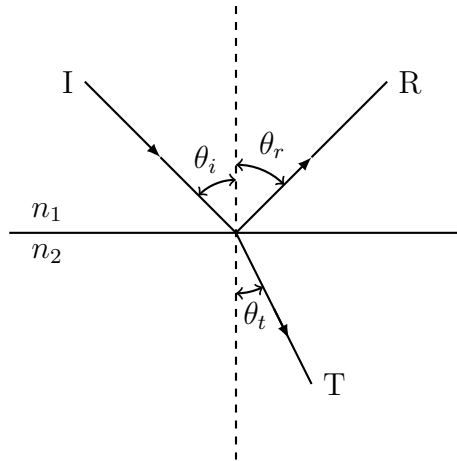


Figure 3.2: An optical photon is reflected or refracted at a polished boundary.

960 in the surface hemisphere, as shown in Fig. 3.3.

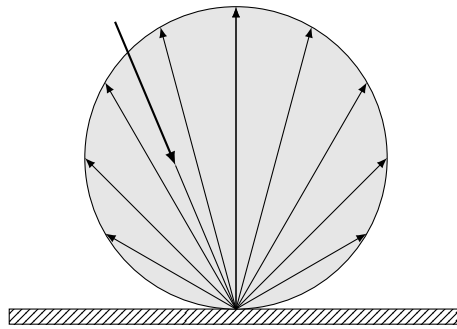


Figure 3.3: The Lambertian reflection.

961 Probabilities of the specular spike, specular lobe, and backscatter reflections are defined
 962 via the `SPECULARSPIKECONSTANT`, `SPECULARLOBECONSTANT`, and `BACKSCATTERCONSTANT` in-
 963 puts, respectively. The Lambertian reflection is implicit, i.e., its probability equals to one
 964 minus the sum of the three constants. This setting ensures the sum of the four reflec-
 965 tion probabilities is unity to preserve the relative probabilities of reflection or refraction, as
 966 shown in Eq. (3.12) and Eq. (3.13). If the three constants are not specified, the Lambertian
 967 reflection is assumed.

968 3.5.3 Scintillation Process

969 The scintillation process is implemented in the `G4Scintillation` class. The average number
970 of emitted optical photons per deposited energy can be defined via the `SCINTILLATIONYIELD`
971 constant. The scintillation yield can also be defined to be dependent on particle type
972 and deposited energy. For example, the scintillation yield for protons can be defined via
973 `PROTONSCINTILLATIONYIELD` as a function of deposited energy. The other supported parti-
974 cles are deuteron, electrons, deuterons, tritons, alphas, and carbon ions [60]. The associated
975 inputs are shown in Table 3.1. The scintillation yield (SY) is used to compute the mean
976 number of scintillation photons N_m , i.e.,

$$N_m = dE \cdot SY, \quad (3.14)$$

977 where dE is the deposited energy. For N_m larger than 10, the actual number of emitted
978 photons N in a Monte Carlo step follows a Gaussian distribution with a standard deviation
979 σ_g calculated from `RESOLUTIONSCALE`, i.e.,

$$\sigma_g = \text{RESOLUTIONSCALE} \cdot \sqrt{N_m}. \quad (3.15)$$

980 For $N_m \leq 10$, N is sampled from Poisson distribution.

981 The scintillation photons may have fast and slow components. The emission spectrum of
982 the fast component is specified by the `FASTCOMPONENT` array as a function of optical photon
983 energy. The decay time constant and the rise time of the fast component are specified via
984 `FASTTIMECONSTANT` and `FASTSCINTILLATIONRISETIME`, respectively. These properties of the
985 slow component can be specified via corresponding inputs. The probability of a scintillation
986 photon born into the fast component is specified by the `YIELDRATIO` parameter.

987 **3.6 Summary**

988 In this chapter, fundamentals of the Monte Carlo simulation were presented. The Monte
989 Carlo method is endorsed by the law of large numbers and the central limit theorem. In a
990 Monte Carlo simulation of particle transport, a general flow consists of sampling the free path,
991 reaction nuclide at the collision site, and reaction type based on respective cross sections.

992 To model and simulate the neutron detectors in this work, the Geant4 Monte Carlo code
993 is used. The code structure of the detector models was described. In addition, the Geant4
994 optical physics used to simulate the scintillation detectors were reviewed. The user-supplied
995 optical properties read by each optical process were summarized. In particular, the optical
996 absorption, boundary, and scintillation processes were discussed. In the following chapters,
997 Geant4 and other codes will be used to model and simulate neutron detectors developed for
998 TREAT.

Chapter 4

Hornyak Button Neutron Detector

The “Hornyak button” is a simple, fast neutron detector constructed from a mixture of ZnS and Lucite first proposed by Hornyak in 1951 [61]. Variants of these detectors [11] were used in the original TREAT hodoscope and are again in use (after refurbishment) at TREAT following the restart of reactor operations. In this chapter, a model constructed using Geant4 is described that was used to simulate the performance of the Hornyak buttons in assumed, hodoscope-like conditions, in which the coupled nuclear and optical physics in the detector were accounted for explicitly. The computed results are compared with reported experimental data to provide a preliminary validation of the computational methodology and physics models used.

4.1 Description of the Hornyak Button

Shown in Fig. 4.1 is the geometry of the Hornyak button detectors used in the original TREAT hodoscope [11]. The devices consist of a scintillation volume sandwiched between two polymethyl methacrylate (PMMA) light guides. The scintillation volume contains a uniform mixture of ZnS(Ag) (5% by mass) and PMMA, whose chemical formula and density are $(C_5O_2H_8)_n$ and 1.19 g/cm^3 , respectively. A PMT is connected to the end of the device (not shown in Fig. 4.1) to collect and amplify the scintillation light. The surfaces not

1017 connected to the PMT are painted white to maximize light retention within the light guide.

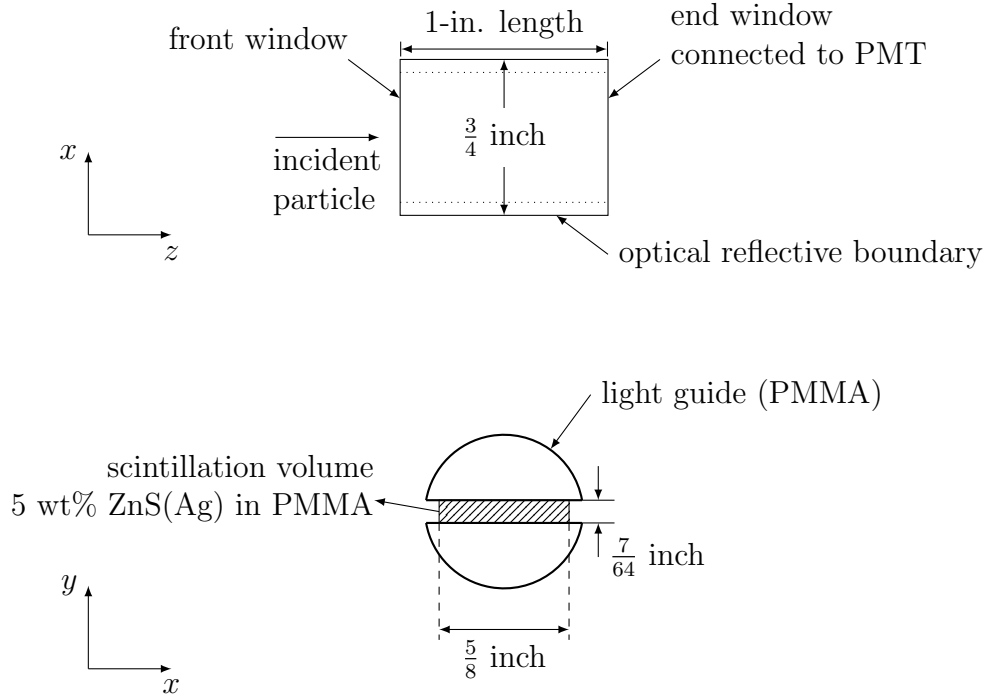


Figure 4.1: Schematic of the Hornyak button as used at TREAT (after [Ref. 11]).

1018 A fast neutron entering the scintillation volume has a certain probability to interact
 1019 with the hydrogen in the PMMA and to generate a recoil proton via elastic scattering.
 1020 If a ZnS(Ag) grain exists along the path of the recoil proton, energy is deposited in the
 1021 scintillator, and light is emitted. The light may leave the scintillation volume, be reflected
 1022 at the white, outer surfaces of the light guide, and reenter the scintillation volume several
 1023 times before arriving at the PMT. In the scintillation volume, the light may be absorbed by
 1024 ZnS(Ag). If a sufficient amount of light reaches the PMT to generate a pulse with height
 1025 larger than the LLD setting, the neutron is detected. The polished, cylindrical light guides
 1026 yield reasonably good light-collection efficiency along the 1-inch length of the scintillation
 1027 volume. For neutrons above 0.1 MeV, the Hornyak buttons used at TREAT were observed
 1028 to have an efficiency of approximately 0.4% [11].

1029 The Hornyak buttons were reported to suffer from large gamma-induced Cherenkov noise
 1030 generated in the light guides and the photomultiplier glass envelope [11]. The gamma rays
 1031 may interact within the Hornyak button to generate electrons via the photoelectric effect,

1032 Compton scattering, and pair production. These electrons can subsequently generate scin-
1033 tillation and Cherenkov noise light. Considering the relatively long range of the electrons,
1034 only a small fraction of the gamma energy is expected to be transferred to the ZnS(Ag).
1035 Therefore, the scintillation noise is relatively easy to eliminate by pulse-height discrimina-
1036 tion. However, because the light guides and the photomultiplier glass envelope consist of a
1037 large volume fraction of the device, production of Cherenkov light is high. The overwhelm-
1038 ing Cherenkov noise may have contributed to the nonlinearity between the detector response
1039 and the TREAT neutron monitors during large transient experiments [11]. To reject the
1040 Cherenkov noise, a pulse-shaping technique was developed based on the decay time differ-
1041 ence between the scintillation light and the Cherenkov light [29]. Additionally, lead filters
1042 were used in front of the detectors to attenuate the gamma rays and to help eliminate the
1043 nonlinearity [11]. These techniques, though successful, complicated the detection system.

1044 4.2 Hodoscope Radiation Environment

1045 To simulate the performance of Hornyak button, the radiation environment in the hodoscope
1046 must be approximated using available information. As stated in Section 1.2.7, the hodoscope
1047 detectors are designed to measure mono-directional, fast neutrons coming through the chan-
1048 nels and to suppress the gamma rays generated from the neutron capture reaction in the
1049 steel collimator. While prompt fission gamma rays were present with an intensity of approx-
1050 imately 5 per fission neutron, these gamma rays may contribute to the prompt signal used to
1051 identify fuel motion. However, for the work described here, the rejection of all gamma rays
1052 was maximized. In addition to the prompt, fission gamma rays, the intensity of the neutron-
1053 activation gamma rays was about 9 additional gamma rays per fission neutron [11]. These
1054 gamma rays originated from neutron activation were modeled as the background radiation
1055 in the calculations.

1056 Because it would be nearly impossible to simulate the original TREAT hodoscope envi-
1057 ronment, it was decided to define a representative neutron and gamma-ray radiation field that
1058 is believed to be conservative. Specifically, neutrons were assumed to be mono-directional

1059 and perpendicular to a detector's front face (i.e., the face adjacent to a collimator channel).
 1060 Neutron energies were assumed to follow a ^{235}U thermal, Watt fission spectrum [62], i.e., for
 1061 neutron energy E in MeV, the probability f is

$$f(E) \propto \exp(-E/0.988) \sinh(\sqrt{2.249E}). \quad (4.1)$$

1062 This spectrum is shown in Fig. 4.2.

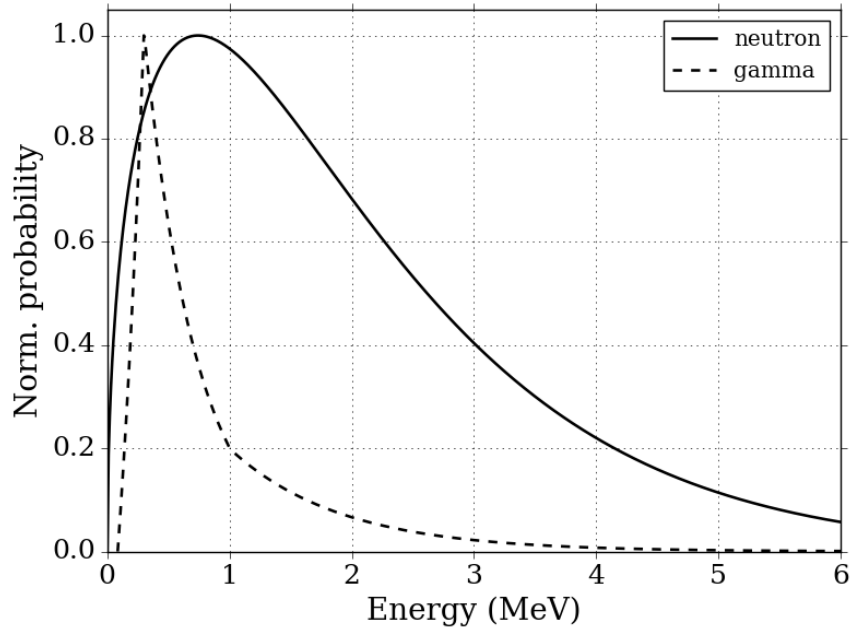


Figure 4.2: Spectra of the ^{235}U , thermal fission neutrons and gamma rays.

1063 For each source neutron incident on the detector, it was assumed that 10 gamma rays
 1064 were *simultaneously incident* on the detector. For different detector form factors in this work,
 1065 this neutron-to-gamma ratio was maintained by adapting the number of gamma rays in a
 1066 pulse event. The gamma rays were assumed to be isotropically distributed in angle and to
 1067 follow a fission gamma-ray spectrum in energy, i.e., the probability G of gamma rays with

1068 energy E in MeV follows [63]

$$G(E) = \begin{cases} 38.13(E - 0.085)e^{1.648E} & E < 0.3 \\ 26.8e^{-2.3E} & 0.3 < E < 1.0 \\ 8.0e^{-1.1E} & 1.0 < E < 8.0 \end{cases}, \quad (4.2)$$

1069 which is shown in Fig. 4.2. Finally, the neutron and gamma-ray sources were assumed to be
 1070 distributed uniformly in space over the detector's entire front face.

1071 4.3 Hornyak Button Model

1072 4.3.1 ZnS(Ag) Grain Randomization

1073 The Hornyak button model developed using Geant4 is shown in Fig. 4.3. The light guides
 1074 were modeled as two sectors, each with a central angle of 160° [11]. To model the homo-
 1075 geneous mixture of ZnS(Ag) and PMMA in the scintillation volume, ZnS(Ag) grains were
 1076 modeled as spheres with a radius of $20 \mu\text{m}$ [64]. Only the reported average radius was used
 1077 because information for grain size distribution is not known from the literature. Indeed,
 1078 the effects of the grain size on detector performance may need to be evaluated (but were
 1079 not considered in this work). Based on a 5% mass fraction of ZnS(Ag) [11], the number of
 1080 ZnS(Ag) grains N_g in the scintillation volume was computed to be about 5×10^5 .

1081 To randomly distribute the N_g grains into the scintillation volume efficiently, a pseudo-
 1082 randomization method was used. The scintillation volume was divided into N_x , N_y , and N_z
 1083 layers along the x , y , and z axes, respectively. The alignment of the scintillation volume with
 1084 respect to the axes is shown in Fig. 4.1. The number of layers along an axis was proportional
 1085 to the corresponding dimension of the scintillation volume, i.e.,

$$\frac{N_x}{L_x} = \frac{N_y}{L_y} = \frac{N_z}{L_z}, \quad (4.3)$$

1086 where $L_x = 5/8$, $L_y = 7/64$, and $L_z = 1$ inch (see Fig. 4.1). These layers formed $N_x \times N_y \times$

1087 $N_z = N_g$ cells, and a cell contained one ZnS(Ag) grain.

1088 As computed, the numbers of layers are not integers, while the number of grains along an
1089 axis must be an integer. Hence, the scintillation volume was first divided into \tilde{N}_z layers along
1090 the z axis, where \tilde{N}_z was the integer part of N_z . Then, each z layer contained $N_{xy} = N_g/\tilde{N}_z$
1091 grains. The values of N_x and N_y were recomputed by

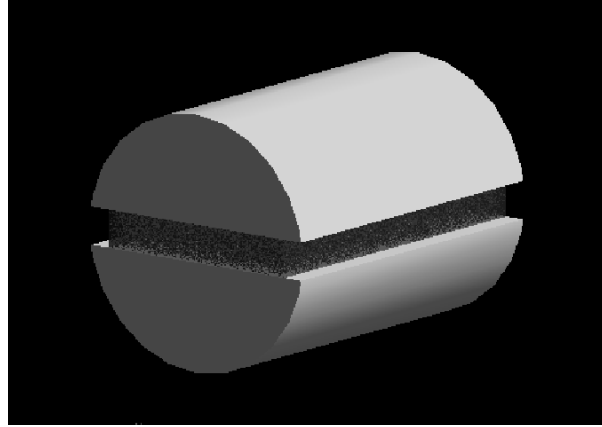
$$\begin{aligned} N_{xy} &= N_x \times N_y \\ N_x/L_x &= N_y/L_y. \end{aligned} \tag{4.4}$$

1092 Then, the number of y layers in a z layer was sampled to be $\tilde{N}_y + 1$ with probability $N_y - \tilde{N}_y$
1093 or \tilde{N}_y otherwise, where \tilde{N}_y is the integer part of N_y . The number of x layers was sampled
1094 in the same way. A ZnS(Ag) grain was randomly embedded in each cell if it did not overlap
1095 with the neighbor placed grains. If placement of a grain in a cell failed 100 times, i.e., all
1096 the sampled positions of the grain overlapped with the neighbor grains, that cell was left as
1097 void, and the number of placed grains was counted. The volume of the scintillation volume
1098 not occupied by the ZnS(Ag) grains (including the void cells) was filled with PMMA. This
1099 pseudo-randomization method avoided issues with overlapping ZnS(Ag) grains and ensured
1100 that desired mass fractions were preserved to within approximately 0.2% of the desired value
1101 for the cases studied. Figure 4.3b shows the random distribution of the ZnS(Ag) grains of
1102 the model.

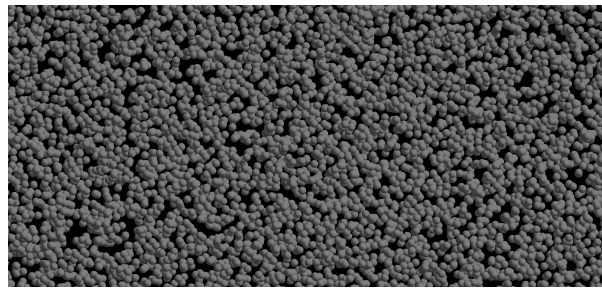
1103 A dummy, finite-volume PMT was connected to the end window of the Hornyak button
1104 (not shown in Fig. 4.3a). If an optical photon left the Hornyak button and entered the PMT
1105 region, the particle was killed, and the tally, i.e., number of detected optical photons in an
1106 event, was increased by one.

1107 4.3.2 Optical Surface Settings

1108 The outer surface of a ZnS(Ag) grain was modeled as ground, and the polished-front-painted
1109 surface finish in Geant4 [59] was used to model the optical reflective property of the outer



(a) Overall geometry



(b) Randomization of the ZnS(Ag) grains in the scintillation volume

Figure 4.3: The developed Hornyak button model in Geant4.

1110 surfaces of the light guides [11]. All other surfaces, e.g., the surfaces between the scintillation
1111 volume and the light guides and the surface between the Hornyak button and the PMT, were
1112 modeled as polished [11, 57]. Because all the surfaces except the coupling ones in the Hornyak
1113 button were coated with white reflective paint [11], no surface absorption of optical photons
1114 was considered. All surfaces were assumed to be of the dielectric-dielectric type.

1115 4.3.3 Source Planes

1116 To simulate neutron responses, prompt neutrons were born uniformly in the cross-sectional
1117 plane of the scintillation volume (Fig. 4.4a). For gamma-induced scintillation, 10 gamma
1118 rays per source neutrons were also sampled uniformly across the cross-sectional plane of
1119 the scintillation volume. However, because Cherenkov radiation is generated in both the
1120 scintillation region and the light guides, incident gamma rays were sampled across the entire

1121 cross-sectional area of the Hornyak button (Fig. 4.4b) in order to simulate the response due
 1122 to Cherenkov radiation. To maintain a consistent gamma-ray intensity between the two
 1123 cases, the number of gamma rays per event for the Cherenkov study was

$$N = \frac{\text{Cross-sectional area of the detector}}{\text{Cross-sectional area of the scintillation volume}} \times 10 \approx 69. \quad (4.5)$$

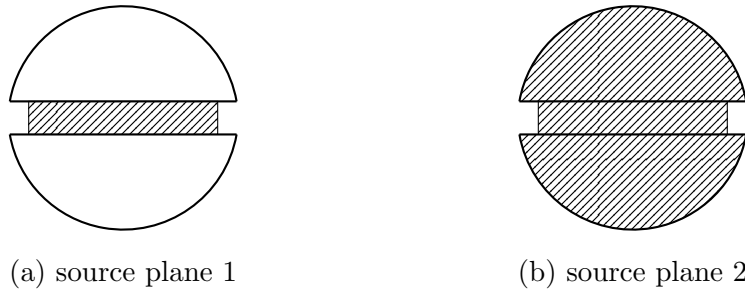


Figure 4.4: One neutron per event was generated uniformly in source plane 1. To evaluate the gamma-induced scintillation noise, 10 gamma rays per event were generated uniformly in source plane 1. To evaluate the gamma-induced Cherenkov noise and the combined Cherenkov-scintillation noise, 69 gamma rays per event were born uniformly in source plane 2.

1124 4.4 Physical Models and Approximations

1125 Geant4 version 10.2 with patch 02 [32] was used to simulate the Hornyak button and other
 1126 ZnS(Ag)-based detectors presented in the next chapter. Neutron interactions were based
 1127 on the neutron cross-section file G4NDL4.5. Nuclear processes were simulated using the
 1128 recommended QGSP BERT HP physics list [55], and all necessary optical processes, e.g.,
 1129 optical absorption, scintillation, Cherenkov, and boundary interactions (using the UNIFIED
 1130 model), were taken into account. For gamma-ray calculations, scintillation and Cherenkov
 1131 processes were enabled independently so that scintillation noise, Cherenkov noise, and their
 1132 combination were analyzed separately.

1133 The refractive index of PMMA is a known function of wavelength [65], with an average
 1134 value of approximately 1.49. For ZnS(Ag), the refractive index was set to 2.36, while the

1135 mean free path of the optical photons in ZnS(Ag) was set to 13 μm [66]. The light yield of
1136 ZnS(Ag) was set to 37 optical photons per keV [67] with an emission spectrum maximized
1137 at a 450-nm wavelength [68]. For all cases, millions of source-particle events were simulated
1138 to obtain good statistics.

1139 4.5 Tally Method

1140 The pulse heights of the Hornyak button and the variants discussed in the next chapter were
1141 represented by the number of detected optical photons (OPs). An optical photon that travels
1142 to the photon-detection device was recognized as detected because of the high PMT and
1143 SiPM (for Hornyak variants evaluated in the next chapter) photon-detection efficiency [9] for
1144 optical photons following the ZnS(Ag) emission spectrum [68]. Pulse height distributions of
1145 these ZnS(Ag)-based scintillation detectors were formed using the `Analysis` class in Geant4
1146 with comma-separated values (CSV) output format. The generated CSV files were post
1147 processed using Python scripts.

1148 4.6 Detector Response and Efficiency

1149 The pulse height distributions of neutron and gamma events were simulated in different runs.
1150 The signal pulse height distribution by neutrons was computed in a run. The pulse height
1151 distribution by gamma rays considering scintillation, Cherenkov, and the combination of
1152 these two processes were calculated in three runs, respectively. The source information in
1153 these runs is specified in Section 4.3.3.

1154 Based on the signal and noise pulse height distributions, an appropriate LLD can be set
1155 to reject a majority of the gamma noise. In the scintillation detectors, the LLD setting was
1156 represented by the number of detected optical photons. At the selected LLD setting, the
1157 neutron-detection efficiency can be calculated, which quantified the detector performance.

1158 Specifically, the detection efficiency ε at an LLD setting was computed as

$$\varepsilon = \frac{\text{Number of pulses with height larger than LLD}}{\text{Total number of pulses}}. \quad (4.6)$$

1159 Corresponding to different LLD settings, the coupled neutron-detection efficiency ε_n and
1160 gamma-detection efficiency ε_g can be computed, with an associated signal-to-noise (S/N)
1161 ratio defined as

$$\text{S/N ratio} = \frac{\varepsilon_n}{\varepsilon_g}. \quad (4.7)$$

1162 To evaluate the hodoscope detectors, if not specified explicitly, the neutron-detection effi-
1163 ciency was defined using an LLD setting consistent with an S/N ratio of 100. It is understood
1164 an S/N ratio of 100 with respect to the background gamma rays is a desirable functional ca-
1165 pability of advanced fast-neutron detectors for the hodoscope [69], and, hence, it is believed
1166 that the neutron-detection efficiency defined in this way is a practical value.

1167 4.7 Results

1168 Shown in Fig. 4.5 are the predicted pulse-height spectra and neutron-detection efficiencies for
1169 the Hornyak button. As indicated by Fig. 4.5a, the neutron event pulse height distribution
1170 is flatter than that of the scintillation noise, which makes pulse-height discrimination of the
1171 scintillation noise possible at reasonably low LLD settings. Contrarily, the intense Cherenkov
1172 noise is readily apparent and dominates the gamma-ray background. Figure 4.5b shows that
1173 for a wide range of LLD settings, the neutron-detection efficiency is on the order of 0.1%. One
1174 factor causing the relatively low neutron-detection efficiency is the small amount of energy
1175 deposited in the scintillator. According to the calculation, on average, each neutron resulted
1176 in approximately 5-keV energy deposited in the ZnS(Ag). This limited energy deposition
1177 may be due to the relative low concentration of the ZnS(Ag) in the scintillation volume,
1178 which results from the compromise between light generation and light absorption.

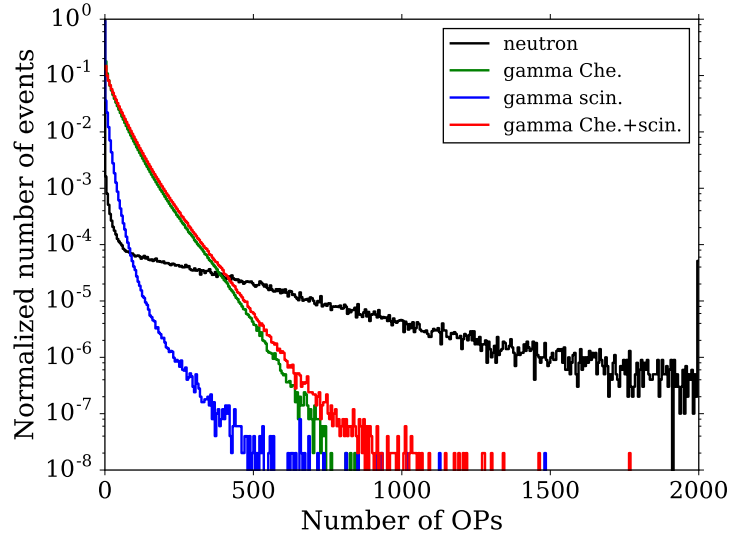
1179 Furthermore, if it is assumed the Cherenkov noise is rejected by the pulse-shaping tech-

1180 nique, as discussed in Section 1.2.8, an LLD setting of 180 optical photons can achieve an
1181 S/N ratio of 100 with respect to gamma-induced scintillation noise, and the corresponding
1182 neutron-detection efficiency is about 0.35%, as shown in Fig. 4.5b. It was reported that the
1183 neutron-detection efficiency of Hornyak button was approximately 0.1%, or, for neutrons
1184 above 0.1 MeV, the value is approximately 0.4% with pulse-shape discrimination to reject
1185 the gamma-induced Cherenkov noise [11]. Hence, the simulated results are in relatively
1186 good agreement with the reported values, an agreement that provides some validation of the
1187 methodology used.

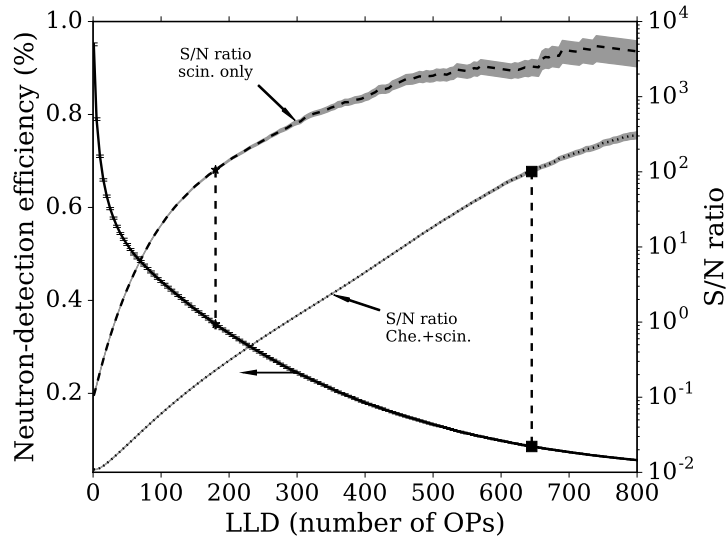
1188 If both gamma-induced scintillation and Cherenkov contributions are included, to achieve
1189 an S/N ratio of 100, an LLD setting of 645 optical photons is necessary, and the corresponding
1190 neutron-detection efficiency is about 0.086%, as shown in Fig. 4.5b. In realistic application,
1191 the Cherenkov noise may even be stronger because it can also be generated in the glass
1192 envelope of the PMT [11] but was not considered in the calculation. Hence, the results
1193 verify the necessity of the pulse-shaping technique to reject the Cherenkov noise, which may
1194 contribute to the non-linear detector response with increased reactor power during transient
1195 experiments [11].

1196 4.8 Summary

1197 In this chapter, the traditional Hornyak button fast-neutron detector used in the hodoscope
1198 was evaluated in Geant4, where the coupled nuclear and optical transports were simulated.
1199 For assumed, hodoscope-like conditions, an intrinsic efficiency of 0.35% for mono-directional
1200 fission neutrons was predicted. The predicted efficiency is in reasonably good agreement
1201 with experimental data from the literature. Strong Cherenkov noise was also observed in
1202 the simulation. If the LLD was set to reject the gamma-induced scintillation and Cherenkov
1203 noises generated in the Hornyak button, the neutron-detector efficiency reduces to about
1204 0.086%. The Cherenkov noise is even stronger if the contribution from PMT was considered.
1205 These results validate the physics models and approximations employed, and the simulation
1206 techniques will be used to evaluate the proposed Hornyak variants in the next chapter.



(a) pulse-height spectra in different cases



(b) neutron-detection efficiency and corresponding S/N ratio as a function of LLD settings, included are the uncertainty bands with one standard deviation

Figure 4.5: Results of the original Hornyak button model.

Chapter 5

Hornyak Button Variants

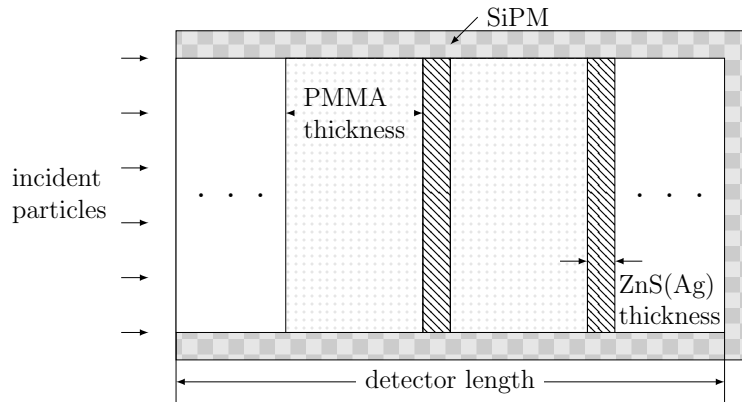
Although the Hornyak button used at TREAT is simple in design and function, the signal ultimately acquired would be improved by designs exhibiting a higher neutron-detection efficiency and/or a higher signal-to-noise ratio (e.g., through the production of less Cherenkov radiation). Here, two variants of the Hornyak button are proposed and studied. The first is an extension of the existing Hornyak button based on an optimal, homogenized mixture of ZnS(Ag) and Lucite. The second uses alternating layers of ZnS(Ag) and Lucite of optimal thicknesses to maximize light transport in the directions orthogonal to the beam line. The new detectors use SiPMs to collect light, which is more efficient than the combination of light guides and the PMT used in the Hornyak button and reduces the Cherenkov noise. The improved light-collection method allows a higher concentration of ZnS(Ag) in the homogenized or the layered scintillation volumes to increase the neutron-detection efficiency. In this chapter, these new detectors are evaluated in Geant4 to demonstrate the designs.

5.1 Design of the Variants

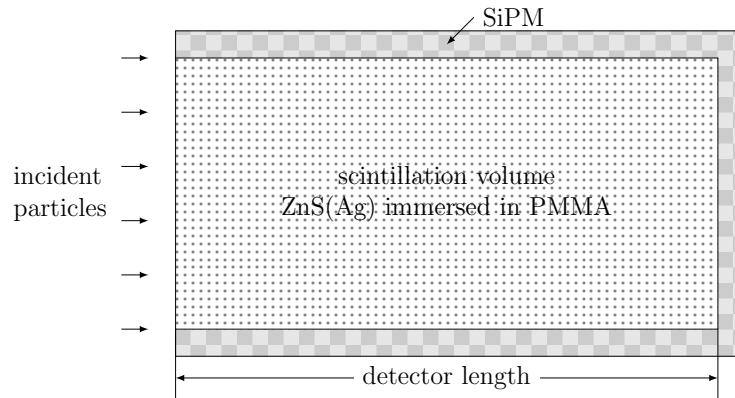
Shown in Fig. 5.1 are the schematics of the layered and the homogenized detectors. SiPMs are used to replace the light guides and PMT used in Hornyak buttons, which reduces generation of the Cherenkov noise and overall detector mass and volume. Therefore, the gamma

1225 background in the TREAT hodoscope may be rejected by use of pulse-height discrimination
 1226 alone, and the more complicated, pulse-shaping techniques used with the Hornyak buttons
 1227 may not be necessary.

1228 The use of SiPMs simplifies the light collection process. In the Hornyak button, the
 1229 majority of the scintillation light needs to be reflected at the cylindrical surfaces of the light
 1230 guides and may re-enter the scintillation volume several times to reach the PMT placed at
 1231 the far end of the device (see Fig. 4.1). Each time the light passes through the scintillation
 1232 volume, it may be absorbed by the relatively opaque ZnS(Ag). By using SiPMs in the new
 1233 detectors, the scintillation light that leaves the scintillation volume can be directly detected.
 1234 Hence, the new light collection method is more efficient.



(a) Layered, ZnS(Ag)/PMMA detector



(b) Homogenized, ZnS(Ag)/PMMA detector

Figure 5.1: Geometric illustrations of the two new detectors. The cross-sectional area of both scintillation volumes is a rectangle with size 2.51×8.89 mm, which is consistent with the designed channel slit in the TREAT hodoscope.

1235 The improved light collection method allows better scintillation volume design. For the
1236 homogenized detector, the scintillation volume is a Hornyak-button-like mixture of PMMA
1237 and ZnS(Ag). Because of the new light collection method, use of a higher concentration of
1238 ZnS(Ag) in the scintillation volume is possible, which increases overall light production and
1239 leads to better maximum performance.

1240 For the layered detector, the scintillation volume consists of repeated layers of ZnS(Ag)
1241 and PMMA. The layered configuration is more efficient for the forward-directional, recoil
1242 protons to deposit energy in the ZnS(Ag) layers compared to the homogenized scintillation
1243 volume, where a proton may not encounter a randomly-distributed ZnS(Ag) grain along its
1244 path and, therefore, cannot generate a signal pulse.

1245 While the homogenized scintillation volume is less efficient for the forward-directed pro-
1246 tons to deposit energy in the scintillator than the layered configuration, this inefficiency
1247 may contribute to improved gamma-ray rejection. As the ratio of background gamma rays
1248 to incident neutrons increases, the corresponding S/N ratio decreases faster for the layered
1249 detector than for the homogenized detector. Hence, the homogenized detector will exhibit
1250 better performance in a highly intense gamma-ray background environment (beyond what
1251 is actually expected in the hodoscope environment).

1252 In the following sections, the Hornyak variants were optimized and evaluated using tech-
1253 niques detailed in Chapter 4. In particular, the new detectors were irradiated by the neu-
1254 tron and gamma sources that represent the hodoscope radiation environment, as detailed in
1255 Section 4.2. Except the gamma rejection evaluations, in a pulse event, one neutron and 10
1256 gamma photons were born uniformly in the detector's cross-sectional plane (a 2.52×8.89 mm
1257 rectangle) to preserve the hodoscope radiation environment, and the renormalization of the
1258 number of gamma photons (as in the evaluation of the Hornyak button, Section 4.3.3) was
1259 not needed. The neutron-detection efficiencies were defined at LLD settings achieving S/N
1260 ratio of 100, where gamma-induced Cherenkov and scintillation noises were considered.

1261 5.2 Layered Detector Results

1262 5.2.1 Thickness Optimization

1263 The primary variables affecting the layered detector performance are the thicknesses of the
 1264 PMMA and the ZnS(Ag) layers. While a thick PMMA layer enhances the proton generation
 1265 and light collection, a large percentage of the recoil protons cannot escape the layer and are
 1266 wasted. According to SRIM [39], the projected range of a 2-MeV proton in PMMA is about
 1267 65 μm . Additionally, a thick ZnS(Ag) layer is beneficial for maximizing the energy deposited
 1268 by entering protons but leads to increased self-absorption of light. Hence, a parametric
 1269 study was performed to find the optimal thicknesses of the PMMA and ZnS(Ag) layers for
 1270 a representative 5-cm long layered device. The ZnS(Ag) layers were modeled with ground
 1271 optical surfaces, while the surfaces of the PMMA layers were modeled as polished.

1272 Table 5.1 summarizes the PMMA and ZnS(Ag) layer thicknesses considered that can yield
 1273 a neutron-detection efficiency above 2%. The gamma-induced noises by the scintillation and
 1274 Cherenkov processes were used to set the LLD. The best case, where the thicknesses of the
 1275 PMMA layer and the ZnS(Ag) layer are 0.18 mm and 12 μm , respectively, can yield an
 1276 efficiency of about 3.31%.

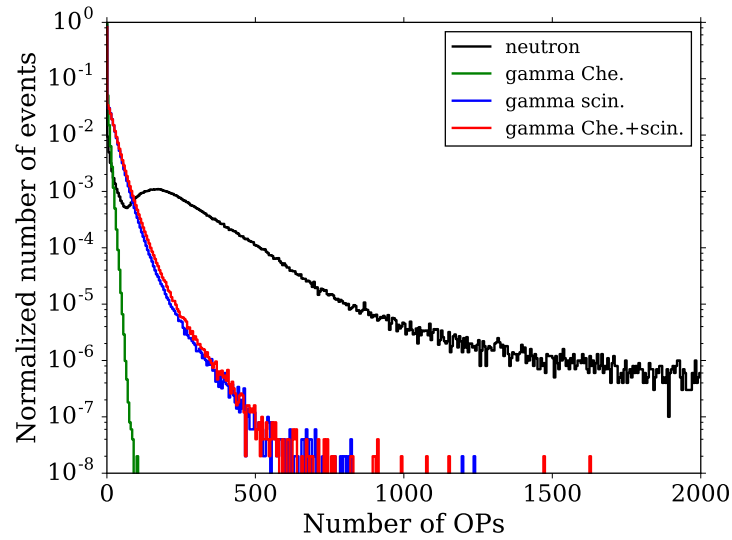
Table 5.1: The neutron-detection efficiencies (%) of a 5-cm long, layered detector under different layer thicknesses.

ZnS(Ag) (μm)	2	4	7	12	21	35	59
PMMA (mm)							
0.10	2.05	3.02	3.15	2.49	2.21		
0.18	2.44	3.03	3.26	3.31	2.71	2.06	
0.32		2.16	2.47	2.54	2.61	2.43	2.11

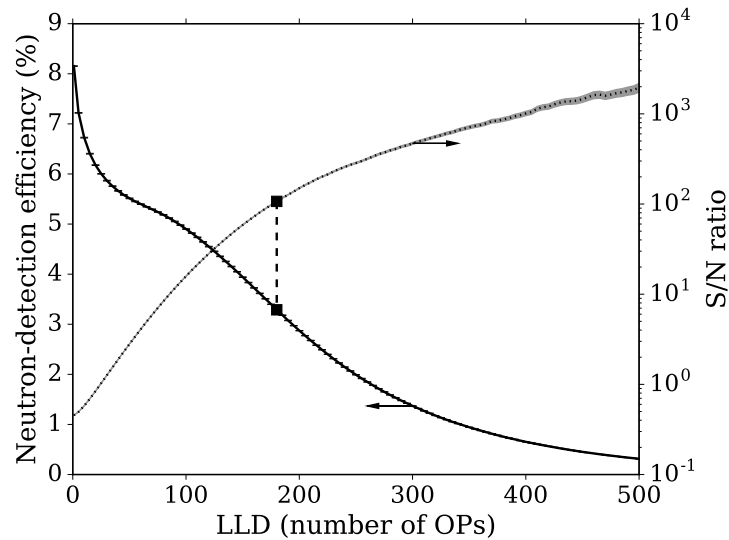
1277 5.2.2 Pulse Height Distributions

1278 Figure 5.2 shows the pulse-height distribution and the neutron-detection efficiencies for a 5-
 1279 cm long device with the optimum layer thicknesses. The gamma-induced noise is primarily
 1280 introduced through scintillation, whereas the Cherenkov noise is minimal and easily rejected

1281 (Fig. 5.2a). In other words, a pulse-shaping technique as used for the Hornyak button is not
 1282 necessary. Moreover, over a wide range of LLD settings, the neutron-detection efficiencies are
 1283 larger than 1% (Fig. 5.2b). At an LLD setting of 180 optical photons, the S/N is predicted to
 1284 be 100, including both scintillation and Cherenkov, with a corresponding neutron-detection
 1285 efficiency of approximately 3.31%.



(a) pulse-height distribution



(b) neutron-detection efficiency as a function of LLD settings. The corresponding S/N ratio (with uncertainty band) is also included.

Figure 5.2: Performance of the 5-cm long, optimized layered detector.

1286 5.2.3 Length Evaluation

1287 Better efficiency is expected by increasing the length of the layered detector, and a study
1288 was performed to determine the neutron-detection efficiency as a function of the detector
1289 length with the PMMA and ZnS(Ag) layer thicknesses set to the best-case values; the results
1290 are shown in Figure 5.3. LLDs that achieved an S/N ratio of 100 were set. At a length
1291 of one inch (the same length as the Hornyak buttons deployed at TREAT), the layered
1292 detector can yield a neutron-detection efficiency of approximately 1.8%. This improved
1293 performance (relative to the Hornyak button efficiency of 0.4%) may be explained by the
1294 increased energy deposition in the scintillator. At this length, the average energy deposited
1295 in ZnS(Ag) layers per source neutron was approximately 26 keV, which was larger than the
1296 energy deposited in the Hornyak button (approximately 5 keV). The results also indicate
1297 the neutron-detection efficiency saturates at just below 6.0% for a device with length larger
1298 than 20 cm. While better neutron-detection efficiency is expected from a longer detector,
1299 when selecting a length, one needs also to consider the size of SiPMs required, the overall
1300 space allocated for the detector and electronics, and the total cost of the resulting system.

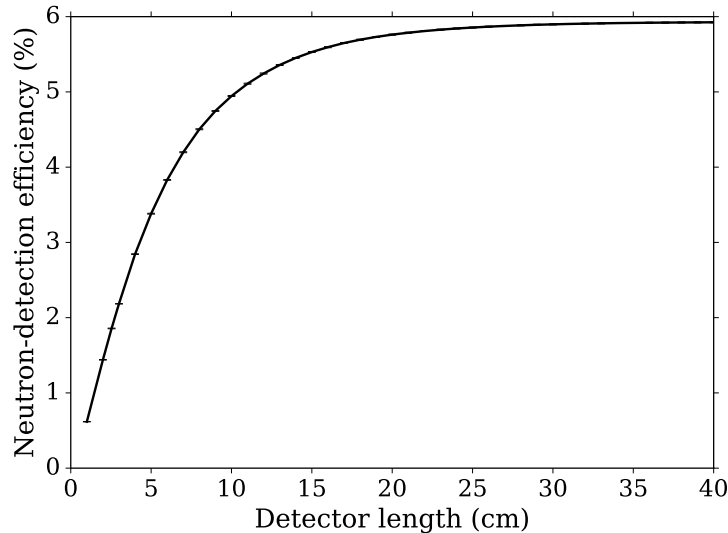


Figure 5.3: Neutron-detection efficiency of the layered detector as a function of the detector length. The thicknesses of PMMA and ZnS(Ag) layers were set to 0.18 mm and 12 μm , respectively.

1301 5.2.4 Gamma Rejection

1302 The layered detector's gamma-rejection capability was evaluated by determining the neutron-
1303 detection efficiency as a function of the background gamma-ray intensity (whereas for all
1304 baseline work, a background intensity of 10 gammas per neutron was assumed). A 5-cm
1305 long device with optimal layer thicknesses was used. As the number of gamma rays per
1306 neutron was increased, a higher LLD setting was required to achieve an S/N ratio of 100.
1307 Hence, the neutron-detection efficiency decreases, as shown in Fig. 5.4. For up to 40 gamma
1308 photons per event, this detector can achieve a neutron-detection efficiency larger than 1%.

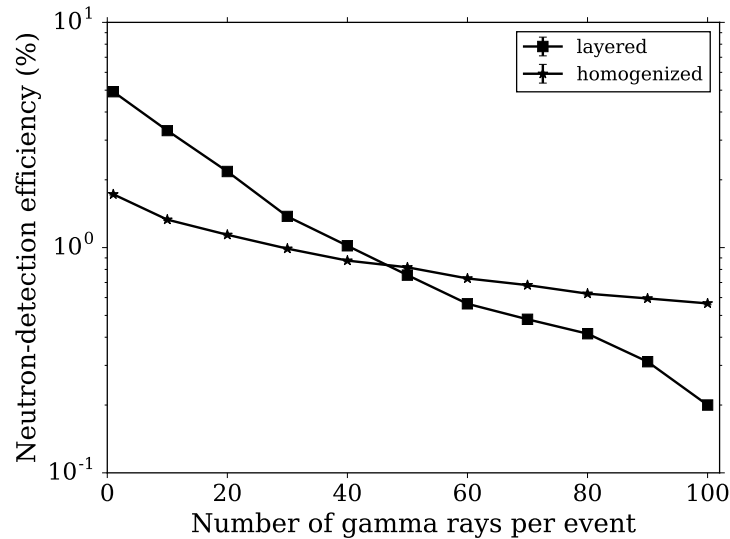


Figure 5.4: A comparison of two new detectors' gamma-rejection capabilities.

1309 5.3 Homogenized Detector Results

1310 5.3.1 ZnS(Ag) Fraction Optimization

1311 The primary variable affecting the homogenized detector performance is the mass fraction
1312 of ZnS(Ag). A higher fraction produces but also absorbs more scintillation light. Figure 5.5
1313 shows the impact of the ZnS(Ag) mass fraction for a 5-cm homogenized detector. At a
1314 mass fraction of 12%, a maximum neutron-detection efficiency of approximately 1.3% was

1315 achieved.

1316 5.3.2 Pulse Height Distributions

1317 The pulse-height distribution and the associated neutron-detection efficiencies at different
1318 LLD settings of the best case are shown in Fig. 5.6. As also observed for the layered
1319 detector, Cherenkov noise can be readily rejected. At a LLD setting of 175 optical photons,
1320 the majority of the gamma-induced scintillation and Cherenkov noise can be discriminated
1321 to achieve an S/N ratio of 100, and the corresponding neutron-detection efficiency is about
1322 1.3%.

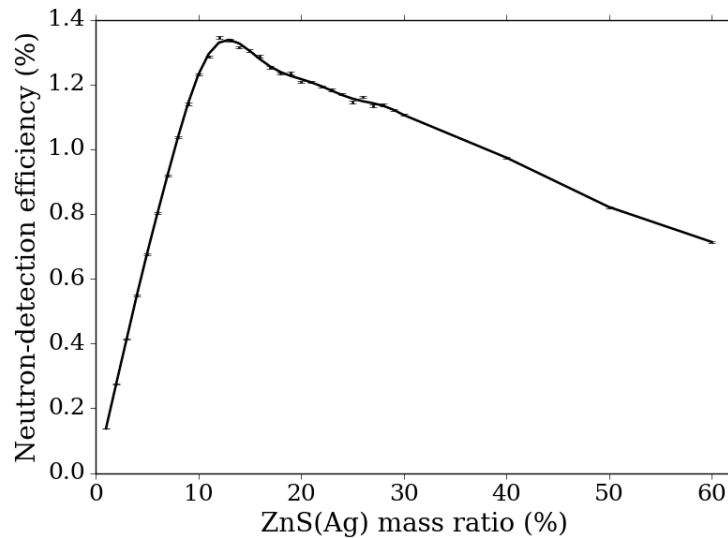
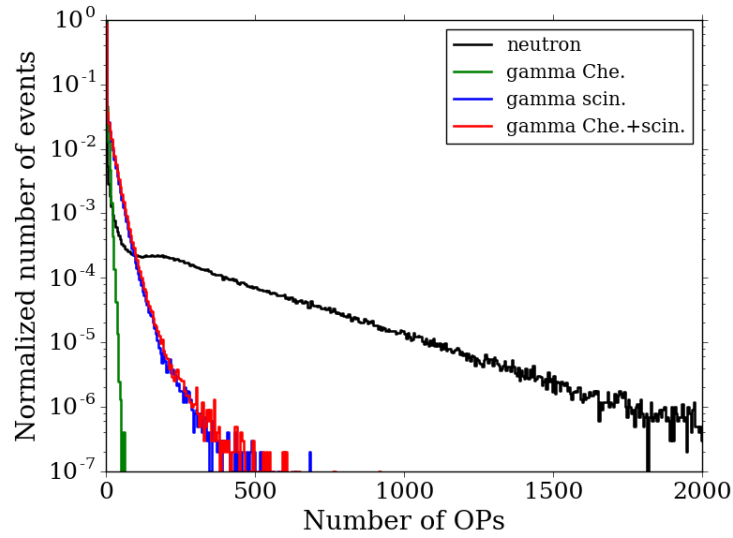


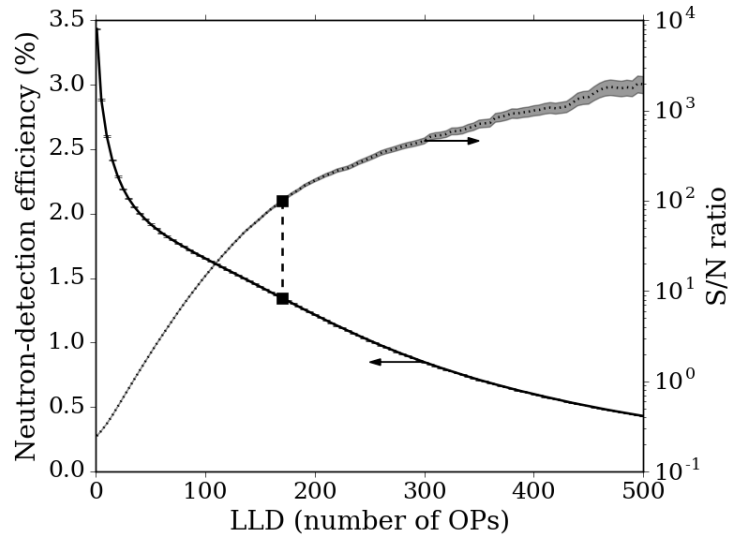
Figure 5.5: Impacts of the ZnS(Ag) mass ratio in the scintillation volume on neutron-detection efficiency.

1323 5.3.3 Length Evaluation

1324 The homogenized detector's efficiency as a function of detector length is shown in Fig. 5.7,
1325 for which the mass fraction of ZnS(Ag) was set to 12%. The results indicate the neutron-
1326 detection efficiency saturates at about 2.2%. To compare to the Hornyak button, at the
1327 length of one inch, the neutron-detection efficiency is about 0.8%. At this length, on average,
1328 one source neutron can result in approximately 12 keV deposited energy in the scintillator,



(a) pulse-height distribution



(b) neutron-detection efficiency as a function of LLD settings. The corresponding S/N ratio (with uncertainty band) is also included.

Figure 5.6: Performance of the 5-cm long, optimized homogenized detector.

1329 which is larger than the 5 keV of the Hornyak button but less than the 26 keV of the layered
 1330 detector.

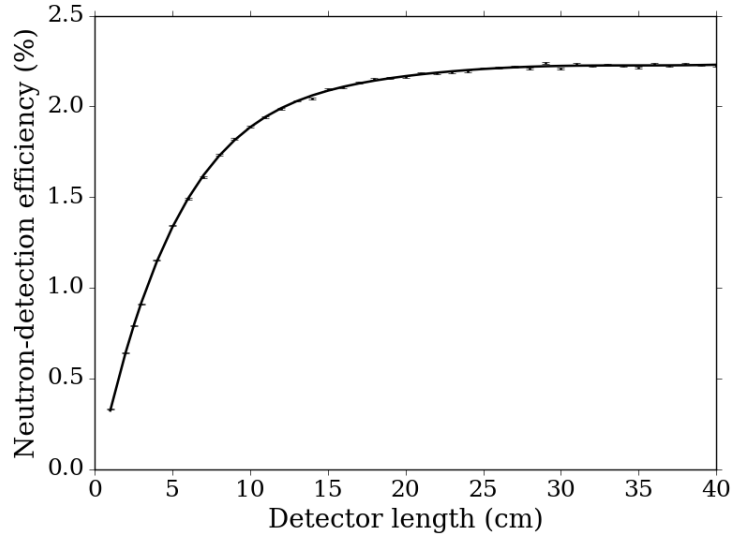


Figure 5.7: Homogenized detector’s performance as a function of detector length.

1331 5.3.4 Gamma Rejection

1332 The homogenized detector’s gamma-rejection capability is illustrated in Fig. 5.4. Up to a
 1333 gamma-to-neutron intensity ratio of about 20, this detector can achieve a neutron-detection
 1334 efficiency above 1%. When the background exceeds 50 gamma rays per pulse event, the
 1335 homogenized detector exhibits better performance than the layered detector. Hence, the
 1336 homogenized detector is more resistant to gamma background, which may be explained by
 1337 its overall lower efficiency.

1338 5.4 Summary

1339 Performance of the layered and the homogenized Hornyak-button variants was evaluated
 1340 in Geant4. By collecting light at the transverse surfaces using SiPMs attached to the pro-
 1341 posed devices, Cherenkov noise is reduced significantly, and gamma-induced scintillation and
 1342 Cherenkov noise can be rejected by using simple pulse-height discrimination alone.

1343 The improved light collection method allowed better scintillation volume designs for
 1344 higher fast-neutron detection efficiency. For the same hodoscope-like conditions used to
 1345 evaluate Hornyak button, at the length of 5 cm, the optimized layered detector was pre-

1346 dicted to have an improved neutron-detection efficiency of approximately 3.3%, while the
1347 optimized homogenized detector was predicted to have an efficiency of approximately 1.3%.
1348 By increasing the detector lengths, efficiencies were shown to saturate at about 5.9% and
1349 2.2% for the layered and homogenized devices, respectively. For more intensive gamma-ray
1350 background (gamma-to-neutron ratios above 50), the homogenized detector exhibited better
1351 performance than the layered detector.

Chapter 6

Fast-Sensitive MSNDs

Besides the Hornyak-button variants described in Chapter 5, fast-sensitive, actinide and hydrogenous MSNDs were also considered for the TREAT hodoscope. Fast-sensitive MSNDs are evolutions of well-established thermal-sensitive devices by using fast-neutron converters. Neutron converters considered are ^{237}Np , ^{235}U , natural uranium, and ^{232}Th for actinide MSNDs and paraffin wax for hydrogenous MSNDs (H-MSNDs). Paraffin wax has a larger fission-spectrum-weighted macroscopic cross section than the actinide materials. However, actinide reactants allow higher LLD settings due to the large energy of fission fragments. In this chapter, these fast-sensitive MSNDs are evaluated using Geant4 and MCNP.

6.1 Description of the MSND

Shown in Fig. 6.1 is the basic design of an MSND [51]. The micro-structured trenches are etched into the high-resistivity *n*-type silicon substrate to a depth of 350 μm [70]. The *p*-type contacts are diffused along the trenches to form the *pn* junction. Then, the trenches are backfilled with neutron converters. Finally, the ohmic contacts are added.

A neutron entering the detector has a certain possibility to interact with the converters in the trenches and to produce the charged particle(s). Then, the charged particle(s) might leave the trench and deposit energy in the silicon depletion region. This deposited energy can

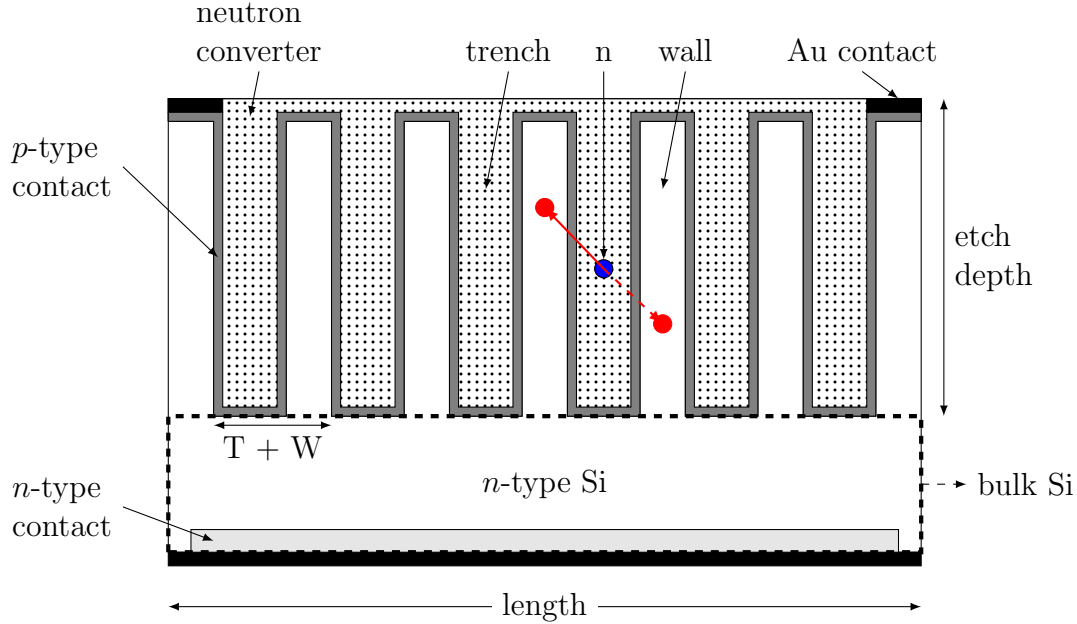


Figure 6.1: Basic design of an MSND, where T is the trench width, and W is the wall width.

1370 excite electron-hole pairs. Under an applied bias, the motion of the charge carriers produces
 1371 a detectable current. The resulting current can then be amplified, measured, and recorded
 1372 by the counting electronics [71]. If the resulting current is beyond the LLD setting, a valid
 1373 count is generated, and the neutron is detected.

1374 Thermal-sensitive MSNDs have been developed at Kansas State University for decades
 1375 [41]. Current generations of the thermal-sensitive devices use ${}^6\text{LiF}$ to convert thermal neu-
 1376 trons. A typical MSND has $20\text{-}\mu\text{m}$ wide trench and $10\text{-}\mu\text{m}$ wall thickness [70]. At a length of
 1377 1 cm, it contains approximately 330 trench-wall pairs. The most-recent incarnation, known
 1378 as the dual-sided MSND, has exhibited an intrinsic thermal neutron detection efficiency of
 1379 69% [42].

1380 To adapt the existing MSND technique for the TREAT hodoscope, fast-sensitive, actinide
 1381 and hydrogenous MSNDs were considered by using fast-neutron converters. The actinide
 1382 MSNDs are loaded with ${}^{237}\text{Np}$, ${}^{235}\text{U}$, natural uranium, or ${}^{232}\text{Th}$. In a neutron event, one of
 1383 the fission fragment pair may enter the active silicon region to generate signal. The H-MSNDs
 1384 use paraffin wax to convert fast neutrons. The recoil proton from neutron scattering reaction
 1385 with the hydrogen nuclide may enter the depleted silicon region to liberate electron-ion pairs.

1386 6.2 Cross Section Comparison of the Converters

1387 Efficiency of a fast-sensitive MSND depends on the probability that a fast neutron interacts
 1388 with the converter. Shown in Fig. 6.2 are the microscopic cross sections of the converting
 1389 reactions and the Watt fission spectrum $\chi(E)$ of neutrons from ^{235}U thermal fission reaction
 1390 (as shown in Eq. (4.1)). As a comparison, the microscopic cross section of the $^6\text{Li}(n, \alpha)^3\text{H}$
 1391 reaction at 0.025 eV is 937 b, as shown in Table 2.1. The χ spectrum peaks at the most-
 1392 probable neutron energy of approximately 0.74 MeV and leads to an average neutron energy
 1393 of about 2 MeV.

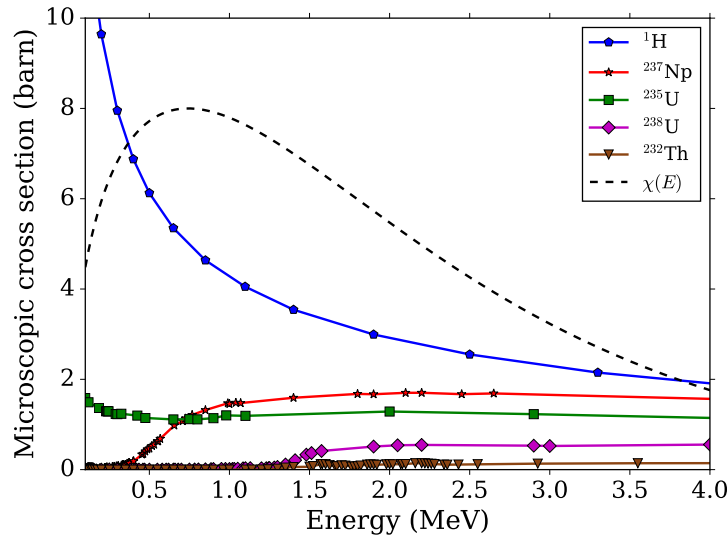


Figure 6.2: Microscopic cross sections of the target reactions [12] and the ^{235}U Watt fission spectrum by thermal neutron.

1394 To quantify the probabilities of the fission neutrons interacting with the nuclides, the
 1395 fission-spectrum-weighted microscopic cross sections were computed as

$$\bar{\sigma} = \frac{\int \sigma(E)\chi(E)dE}{\int \chi(E)dE}, \quad (6.1)$$

1396 where the integrals are from 10^{-11} to 20 MeV, and the results are shown in Table 6.1. Paraffin
 1397 wax has the highest macroscopic cross section of 0.32 cm^{-1} , and ^{237}Np has the largest cross
 1398 section among actinides by a small margin. While the neutron-converting probabilities of

1399 the actinide MSNDs are smaller than the H-MSNDs, the actinide MSNDs allow higher LLD
 1400 settings to reject neutron-activation gamma rays in the hodoscope because of the large energy
 1401 of fission fragments.

Table 6.1: Comparison of the converter cross sections.

Converter	Density (g/cm ³)	Molecular weight (g/mole)	$\bar{\sigma}$ (b)	$\bar{\Sigma}$ (cm ⁻¹)
paraffin wax (C ₂₅ H ₅₂ [72])	0.93	352.68	3.93	0.32
²³⁷ Np	20.25	237.05	1.31	0.067
²³⁵ U	18.95	235.04	1.21	0.059
²³⁸ U	18.95	238.05	0.31	0.015
²³² Th	11.72	232.04	0.075	0.0023

1402 6.3 Modeling Details

1403 The fast-sensitive MSNDs were evaluated using Geant4 and MCNP. A previous MCNP6
 1404 simulation showed the ²³⁷Np-filled and the ²³⁵U-filled MSNDs yielded efficiencies larger than
 1405 1% [43]. In the following, the actinide MSNDs filled with ²³⁵U, natural uranium, and ²³²Th
 1406 were re-evaluated in Geant4 using the fission fragment generator (FFG) [34]. The FFG
 1407 samples and tracks fission fragments in a single run to simplify the two-step evaluation in
 1408 MCNP6 [43].

1409 ²³⁷Np-filled MSNDs were not evaluated because Geant4 does not include the neutron
 1410 data for ²³⁷Np [73]. Though absent, the predicted efficiencies of the ²³⁷Np-filled MSNDs
 1411 were better than those of ²³⁵U-filled devices [43]. More importantly, ²³⁷Np may be preferred
 1412 to ²³⁵U because it is insensitive to neutrons below about 1 MeV, which are generated by the
 1413 slowing down of the fast neutrons in the test section [11] and the collimator in the TREAT
 1414 facility. These sub-fast neutrons are a further source of background radiation in addition to
 1415 neutron-activation gamma rays.

1416 The neutron event pulse-height distributions (NEPHDs) of the H-MSNDs were computed
 1417 in Geant4 and MCNP6 for comparison. The pulse-height distributions (PHDs) of the H-
 1418 MSNDs from hodoscope-like gamma rays were calculated in Geant4, where the number of

1419 source particles per event was adjustable to simulate the gamma ray strength. For complete-
1420 ness, the neutron-detection efficiencies of the H-MSNDs at the 300-keV LLD [71] and the
1421 LLD settings that achieved S/N ratio of 100 based on the gamma event PHDs were reported,
1422 respectively.

1423 **6.3.1 Neutron Data Library**

1424 Performance of fast-sensitive MSNDs was evaluated in Geant4 10.03.p01 [32] and MCNP6.1
1425 [33]. The G4NDL4.5 neutron data library [73] was employed in the Geant4 calculations. This
1426 library is primarily based on the ENDF/B-VII.1 nuclear data [12]. Because the G4NDL4.5
1427 library only contains the data for isotopes up to uranium [73], the ^{237}Np -filled MSNDs were
1428 not evaluated with Geant4. The MCNP6 calculations used the ENDF/B-VII.0 nuclear data
1429 [74]. All cross sections used were for a temperature of 293 K.

1430 **6.3.2 MSND Models for NEPHDs**

1431 Shown in Fig. 6.3 and Fig. 6.4 are the MSND models developed for NEPHDs in Geant4 and
1432 MCNP6, respectively. Because the neutron-sensitive materials in the MSNDs are primarily
1433 the converters in the trenches, these models consisted of the etched silicon region, i.e., the
1434 repeated trench-wall structures, as shown in Fig. 6.5. For illustration, the trench and the
1435 wall widths in Fig. 6.3 and Fig. 6.4 were 0.1 cm. The NEPHDs of the actinide MSNDs
1436 were computed in Geant4 using the FFG. The NEPHDs of the H-MSNDs were computed in
1437 Geant4 and MCNP6 for comparison.

1438 **6.3.3 MSND Model for Gamma Event PHDs**

1439 Shown in Fig. 6.6 is the H-MSND model to compute the gamma event PHDs in Geant4.
1440 In the model, the electronic board, the bulk silicon region, and the etched silicon region
1441 were considered. Their dimensions in the height-depth plane are shown in Figure 6.5. These
1442 volumes were sensitive to the gamma rays due to the relatively high- Z materials. Silicon has

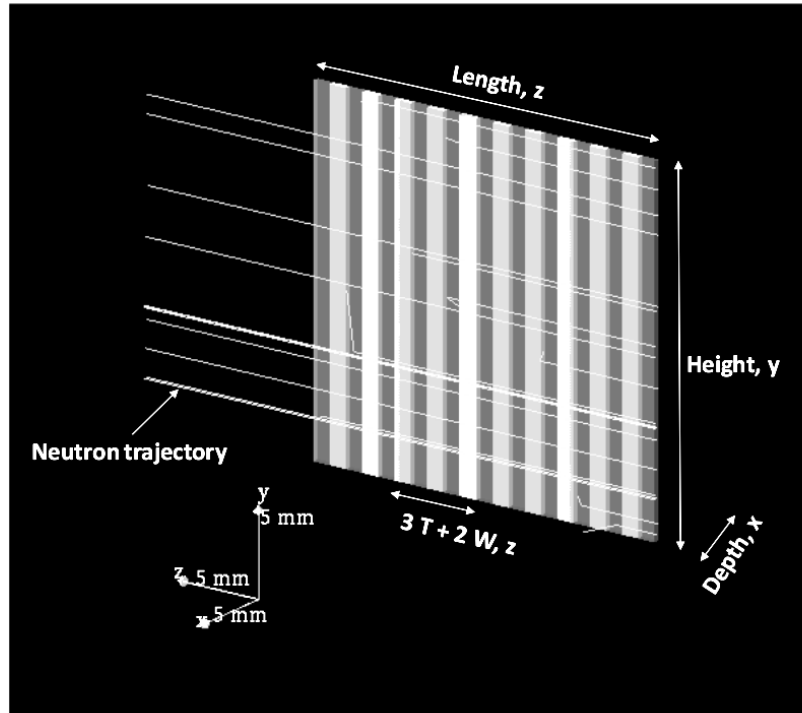
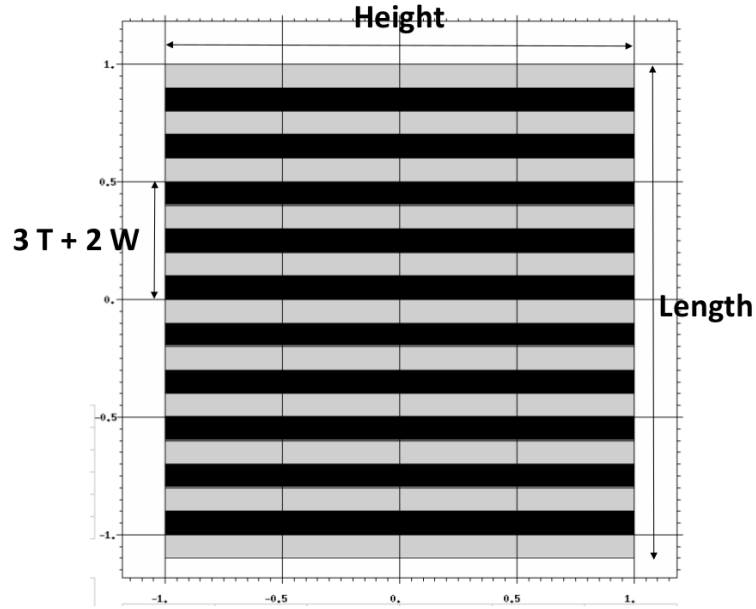


Figure 6.3: The developed MSND model for NEPHDs in Geant4. The trench (T) and wall (W) widths were 0.1 cm for illustration.

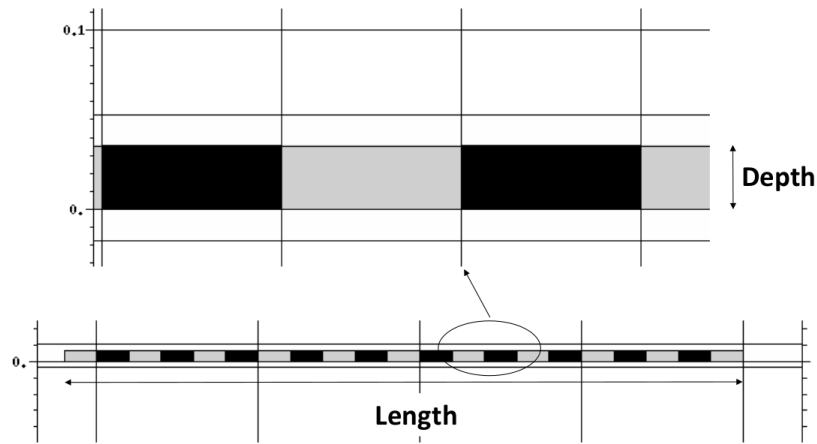
1443 an atomic number Z of 14, and the electronic board contained copper ($Z = 29$) and bromine
 1444 ($Z = 35$).

1445 Geant4 was used to compute the gamma event PHDs because the number of source
 1446 particles in a pulse event was adjustable [60]. Hence, specific gamma-to-neutron intensity
 1447 ratio can be sampled to simulate the hodoscope environment.

1448 Based on the Geant4-computed neutron and gamma event PHDs of the H-MSNDs, LLDs
 1449 that achieved S/N ratio of 100 [69] were set to define the practical neutron-detection effi-
 1450 ciencies in the hodoscope. The actinide MSNDs' responses to the gamma rays were not
 1451 evaluated because the energetic fission fragments allowed high LLD settings intrinsically.



(a) height-length plane



(b) depth-length plane

Figure 6.4: The developed MSND model for NEPHDs in MCNP6. The trench (T) and wall (W) widths were 0.1 cm for illustration.

1452 6.3.4 Physics Settings

1453 Geant4 Physics Setting

1454 The QGSP BERT HP reference physics list [55] was used in the Geant4 calculations. In

1455 Geant4, the secondary particle production threshold is specified as the range cutoff in dis-

1456 tance unit [60], i.e., the secondary particle that can travel longer than the cutoff is generated.

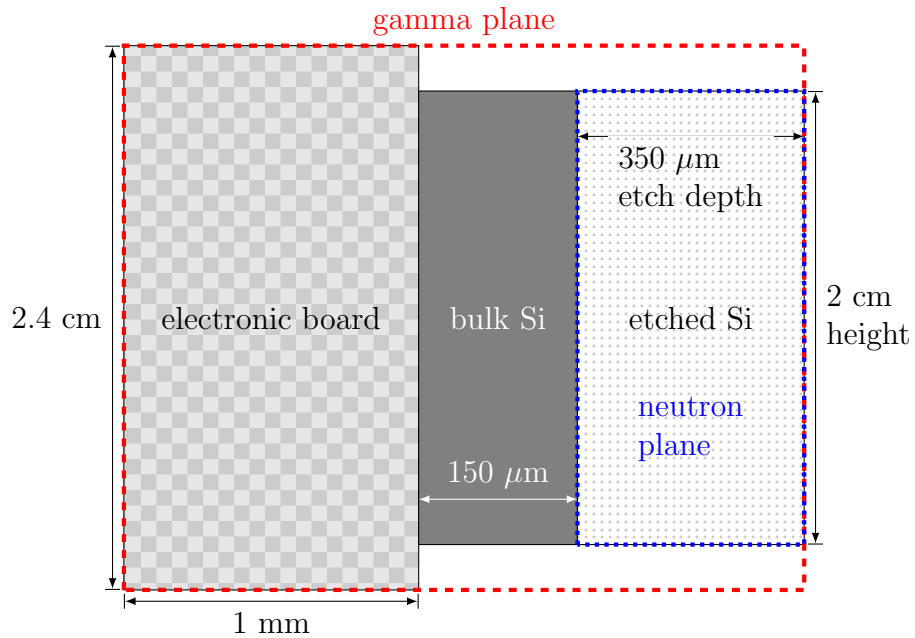


Figure 6.5: The etched silicon region was modeled to compute the NEPHDs in Geant4 and MCNP6. To evaluate the H-MSNDs' responses to the gamma rays in Geant4, the bulk silicon region and the electronic board were added. The neutron and the gamma source generation planes were set correspondingly.

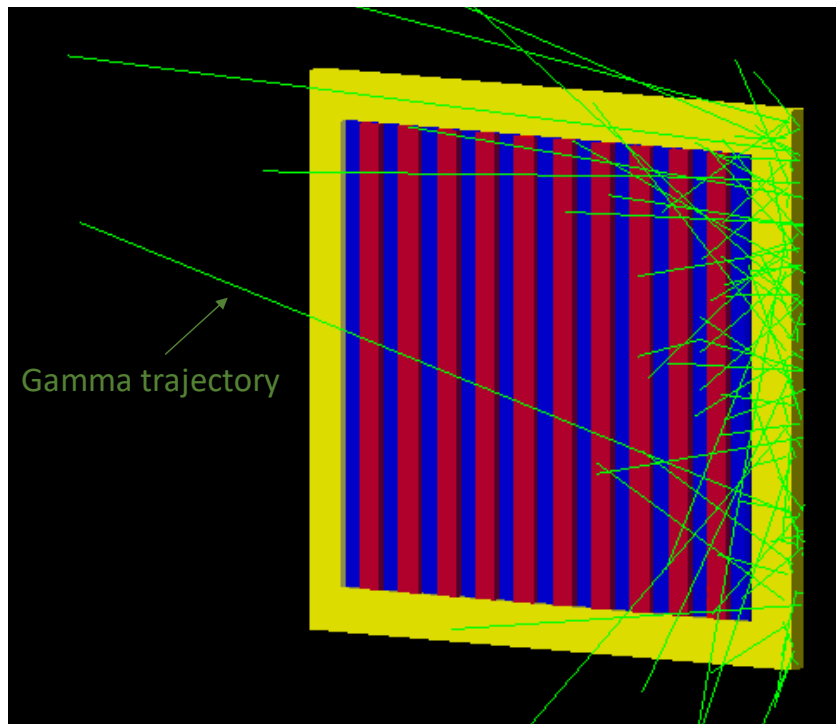


Figure 6.6: The H-MSND model to calculate the gamma event PHDs in Geant4.

1457 Based on the range cutoff, the production threshold energies for different materials are com-
1458 puted. The energy equivalences of the range cutoff cannot be lower than a lower-bound,
1459 threshold value; otherwise, the lower-bound value will be used. For best accuracy, the lower-
1460 bound value was set to 250 eV, which is the lower limit for the low-energy electromagnetic
1461 processes [32], and the range cutoff was set to 10 nm to activate the lower-bound value. In
1462 addition, the produced particles are tracked to zero energy [60].

1463 MCNP6 Physics Setting

1464 In MCNP6, to obtain the most accurate energy deposition, the potential secondary particles
1465 (proton, heavy ion, photon, and electron) were transported in the calculations [35]. In the
1466 neutron physics card, the analog energy limit parameter, *emcnf*, was set to 100 MeV. This
1467 setting performed analog capture for the neutrons with energies smaller than 100 MeV,
1468 which provided reliable f8 pulse-height tally. The light-ion and heavy-ion recoil and neutron
1469 capture ion algorithm (NCIA) control parameter, *coifl*, was set to the recommended value
1470 of four [35], which generated one ion from neutron elastic scattering. In the proton physics
1471 card, the *recl* light ion recoil control parameter was set to one. Hence, one light ion was
1472 created at each proton elastic scatter event with light nuclei, i.e., hydrogen, deuteron, triton,
1473 ^3He , and ^4He . The default values for the other physics settings were used. The default
1474 energy cutoffs for neutron (0), electron (1 keV) and photon (1 keV) were used. The energy
1475 cutoffs for the proton and heavy ion were decreased to the lower limit of 1 keV.

1476 6.3.5 Source Terms

1477 Neutron Source

1478 In the NEPHD calculations, mono-directional source neutrons traveled along the length-
1479 wise direction. The neutron trajectories in Geant4 are shown in Fig. 6.3. These neutrons
1480 were generated uniformly in the depth-height plane of the etched silicon region, as shown in
1481 Figure 6.5. Energies of the neutrons were sampled from Eq. (4.1).

1482 **Gamma-Ray Source**

1483 Details of the gamma source are specified in Section 4.2, i.e., fission-spectrum gamma rays
1484 were shot into the detector isotropically with an intensity of 10 gamma rays per neutron.
1485 Because the gamma rays may interact within the electronic board and the silicon substrate,
1486 the source gamma rays were born in a plane covering the H-MSND ($2.4 \text{ cm} \times 1.5 \text{ mm}$,
1487 Figure 6.5). Considering the different sampling areas of the neutron and the gamma sources
1488 (Figure 6.5), to maintain an intensity of 10 gamma rays per fast neutron, the number of
1489 gamma rays per event (N_g) was scaled to

$$N_g = \frac{A_g}{A_n} \times 10 = \frac{2.4 \times (0.1 + 0.05)}{2 \times 0.035} \times 10 \approx 51, \quad (6.2)$$

1490 where A_g and A_n are the areas of the gamma-ray and the neutron source planes, respectively.

1491 **6.3.6 Tally Methods**

1492 In the NEPHD calculations, the deposited energy spectra in the walls were tallied. In the
1493 gamma event PHD calculations, the deposited energy spectra in the silicon depletion region,
1494 i.e., the walls and the bulk silicon, were tallied.

1495 In Geant4, the deposited energy spectra were computed by the user actions [60]. In
1496 MCNP6, the f6 tally by all the tracked particles was first used to compute the deposited
1497 energy in the tally region. Then, based on the f6 tally, the PHD was computed by the *ft phl*
1498 option of the f8 tally [35].

1499 **6.4 Assumptions of the Modeling**

1500 To evaluate the MSNDs, a few assumptions were made:

- 1501 1. The neutron interactions outside the etched silicon region, e.g., the bulk silicon region,
1502 were not considered, though these reactions may contribute to the neutron detection
1503 efficiency.

- 1504 2. A perfect charge collection efficiency in silicon was assumed. Indeed, the charge col-
1505 lection efficiency may deteriorate due to the damage or degradation of silicon caused
1506 by the fission fragments or protons. These negative effects need further experimental
1507 evaluation.
- 1508 3. The neutrons traveled along the detector length direction perfectly. The impact of
1509 any departure from this idealized alignment in practical applications warrants future
1510 consideration.

1511 **6.5 Evaluation and Results**

1512 **6.5.1 Effects of Parameters**

1513 The fast-sensitive MSNDs with different trench widths, wall widths, and lengths were eval-
1514 uated. All the detectors had 350- μm depth and 2-cm height. The depth and height were
1515 consistent with the current thermal-sensitive MSNDs [70].

1516 For a fixed length, when the trench width is small, an increase of the trench width
1517 results in higher neutron-sensitive volume fraction for better efficiency. If the trench width
1518 increases further, more charge particles are generated, but a large portion of their energies
1519 are deposited in the trenches. Because the electric signal is caused by the energy deposited
1520 in the silicon, trapping of the charge particles in the trenches deteriorate the efficiency.

1521 A wider wall enables the charged particles to deposit more energy in the silicon, which
1522 allows a higher LLD setting. However, for a fixed length, a wider wall leads to smaller
1523 neutron-sensitive volume fraction. Therefore, fewer charged particles are generated. Addi-
1524 tionally, a wider wall increases the H-MSND's gamma sensitivity.

1525 For fixed trench and wall widths, a longer MSND yields better efficiency because the
1526 neutron penetrates more trench-wall pairs. Longer lengths can be achieved by stacking
1527 the processed silicon substrates into an array, similar to proposed ^3He replacement devices
1528 [75]. The length is also limited by the space in the hodoscope to install the MSND, i.e.,
1529 approximately 20 cm.

1530 6.5.2 Actinide MSNDs

1531 Trench-Wall Optimization

1532 Shown in Fig. 6.7 are the Geant4-computed neutron detection efficiencies of the 2-cm long
1533 ^{235}U -filled MSNDs with different trench and wall widths at a LLD setting of 5 MeV. With
1534 20- μm trench and 10- μm wall widths, the ^{235}U -filled MSND yields intrinsic neutron detection
1535 efficiency of about 1.2%. Though better efficiencies are achievable with smaller trench widths,
1536 filling the trenches with uranium has proven difficult [43].

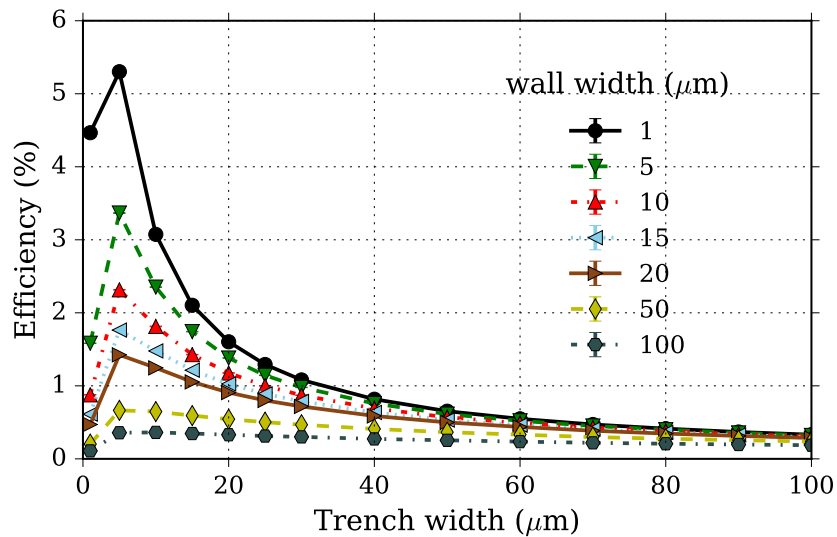


Figure 6.7: The Geant4-computed neutron-detection efficiencies of the 2-cm long ^{235}U -filled MSNDs with different trench and wall widths at the 5-MeV LLD.

1537 NEPHDs

1538 The Geant4-predicted distributions of the energy deposition by the fission fragments in silicon
1539 of the actinide MSNDs with 2-cm length, 20- μm trench and 10- μm wall widths are shown
1540 in Figure 6.8. The distribution of the ^{235}U -filled MSND features peaks A and B at about
1541 18 MeV and 30 MeV, respectively, plateaus C and D, and slopes E and F. The features for
1542 MSNDs filled with natural uranium and ^{232}Th are not significant (probably also exist).

1543 The formation of these features may be explained using Fig. 6.9, where P1, P2, and P3
1544 are extreme paths for a fission fragment to enter the silicon wall. P1 is the shortest length to

1545 penetrate the wall along the depth direction. P2 is nearly perpendicular to the wall depth
1546 direction. P3 represents the path for a fission fragment to deposit all kinetic energy while
1547 reaching the wall width limit.

1548 While the true fission-fragment distribution was sampled by the fission fragment gener-
1549 ator in Geant4 to generate the results in Fig. 6.8, to understand the features exhibited in
1550 Figure 6.8 in more depth, consider a representative fission fragment pair of ^{95}Sr and ^{139}Xe
1551 with initial kinetic energies of 100 and 70 MeV, respectively. In the uranium trench, the
1552 projected ranges for these two ions are 5.7 and 4.1 μm , respectively, and in the silicon wall,
1553 the projected ranges for these two ions are 16.7 and 11.8 μm , respectively [39]. Based on
1554 the projected ranges in uranium and 20- μm trench, only one fission fragment of a pair can
1555 enter the wall.

1556 If a fission fragment enters the wall with energy not sufficient to leave the wall even along
1557 the shortest path P1, the contribution of this fission fragment is under peak B for Sr, or
1558 peak A for Xe.

1559 If a fission fragment enters the wall with more energy to penetrate the wall along the
1560 shortest path P1, and its path is between P2 and P3, all of its kinetic energy is deposited
1561 in the wall because the 2-cm height and 350- μm etch depth (as shown in Fig. 6.5) are much
1562 larger dimensions than the 10- μm wall width. If the fission fragment is Sr, its deposited
1563 energy is 100 MeV less the energy deposited in the born trench 1, which leads to slope F in
1564 Fig. 6.8. If the fission fragment entering the wall is Xe, the corresponding feature is slope E.

1565 If the range of the fission fragment that enters the wall is larger than P1, and the path
1566 is between P3 and P1, a part of the kinetic energy is deposited in the wall. If the fission
1567 fragment is Sr, the contribution is under the area of plateau C, slope E, and plateau D with
1568 height of plateau D. If the fission fragment is Xe, it contributes to plateau C besides the
1569 contribution of Sr.

1570 The results in Fig. 6.8 indicate the actinide MSNDs allow high LLD settings, e.g., 10 MeV.

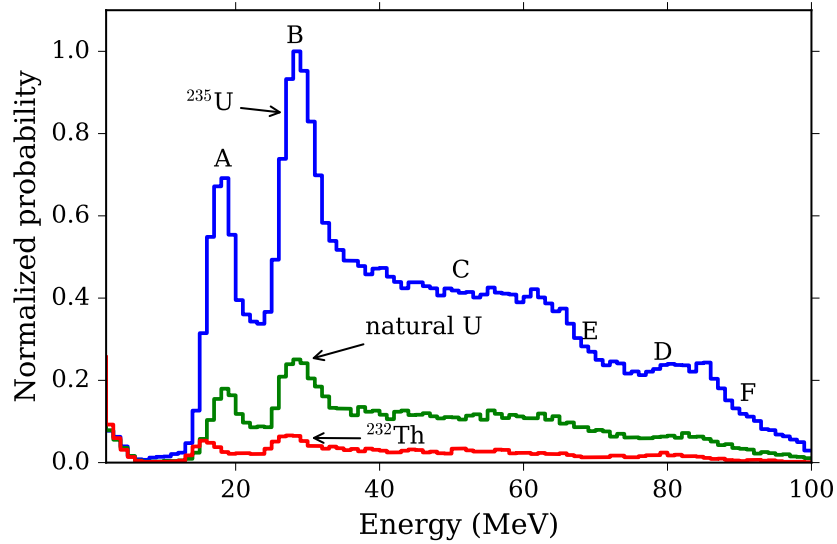


Figure 6.8: The Geant4-predicted distributions of the energy deposition in silicon by fission fragments of the 2-cm long actinide MSNDs with 20- μm trench and 10- μm wall widths.

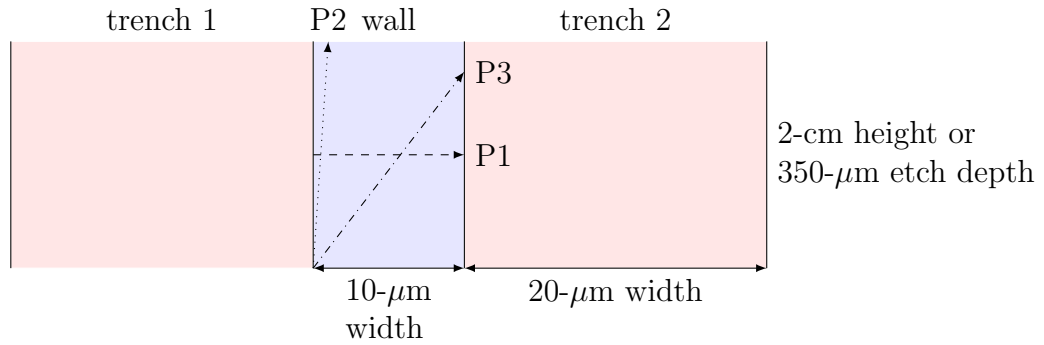


Figure 6.9: Extreme paths of fission fragments in the actinide MSND.

1571 Efficiencies of the Actinide MSND Arrays

1572 With 20- μm trench and 10- μm wall widths, intrinsic neutron detection efficiencies of the
 1573 actinide MSNDs with different lengths are shown in Figure 6.10. The 5-MeV LLD was
 1574 applied. The ^{235}U -filled MSNDs with lengths larger than 14 cm yield intrinsic neutron
 1575 detection efficiency of about 2.6%. The MSNDs filled with natural uranium and ^{232}Th can
 1576 not achieve efficiencies larger than 1%.

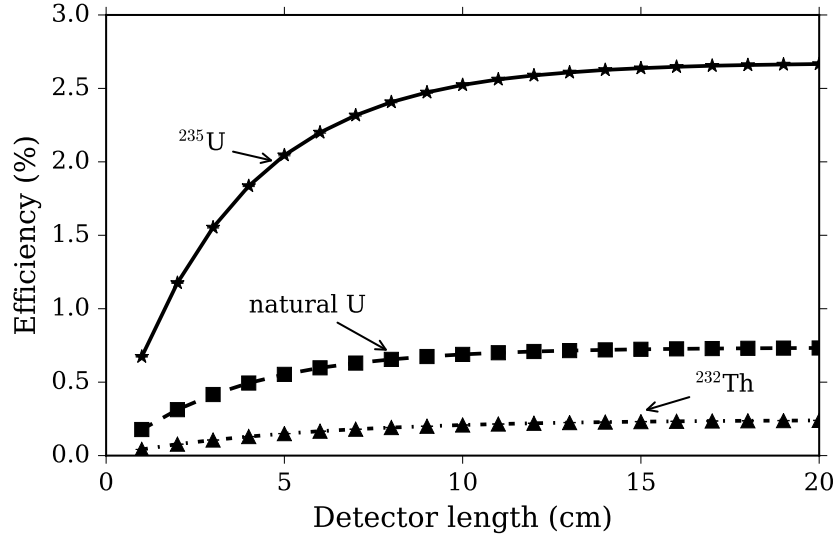


Figure 6.10: The Geant4-computed intrinsic neutron detection efficiencies of the actinide MSND arrays. The MSNDs had 20 μm trench and 10 μm wall widths. The LLDs were set to 5 MeV.

1577 Comparison between Geant4 and MCNP6

1578 The Geant4-computed and the MCNP6-computed total deposited energies in the trenches
 1579 per neutron of the actinide MSNDs were compared. The MSNDs had the geometry of 2-cm
 1580 length, 20- μm trench, and 10- μm wall widths (orientation of the dimensions is shown in
 1581 Fig. 6.1). This particular comparison was made because MCNP6 assumes the fission energy
 1582 is deposited locally [35]. To be consistent, the FFG in Geant4 was turned off.

1583 Shown in Table 6.2 are the computed results, which agree relatively well. The difference
 1584 is computed by

$$E_g - E_m, \quad (6.3)$$

1585 where E_g is the Geant4-predicted deposited energy, and E_m is the calculated deposited
 1586 energy by MCNP. For ^{235}U , the Geant4-computed tally is smaller than the MCNP6 value
 1587 by about 0.073 MeV. The differences might be caused by the different cross section libraries
 1588 used by the two codes, as discussed in Section 6.3.1.

Table 6.2: Total deposited energies (MeV) in the trenches per neutron computed by Geant4 and MCNP6 and their differences (relative to MCNP6).

	MCNP6	Geant4	Difference
^{235}U	10.44 ± 0.020	10.37 ± 0.041	-0.073 ± 0.045
Natural Uranium	2.75 ± 0.012	2.64 ± 0.021	-0.11 ± 0.024
^{232}Th	0.46 ± 0.0022	0.42 ± 0.0080	-0.031 ± 0.0083

1589 Alpha Decay of the Reactants

1590 Besides the necessity of discriminating gamma rays in the hodoscope environment, the LLD
 1591 of the actinide MSNDs must be set to account for the decay alpha particles of the converters.
 1592 Table 6.3 summarizes the alpha decay information of the actinide reactants in the MSNDs
 1593 with the geometry of 2-cm length, 20- μm trench, and 10- μm wall widths. The energies of
 1594 the alpha particles are approximately 4 MeV. In the 10- μs pulse shaping time of current
 1595 MSND [71], the number of alpha particles would not exceed 1.41. Hence, a 5-MeV LLD
 1596 should be sufficient to reject the alpha particles and the gamma rays. In addition, based
 1597 on the NEPHDs (Fig. 6.8), the LLD can be set to 10 MeV without significant efficiency
 1598 deterioration.

Table 6.3: Alpha decays of the 2-cm long actinide MSNDs with 20- μm trench and 10- μm wall widths. Data from Ref. [16].

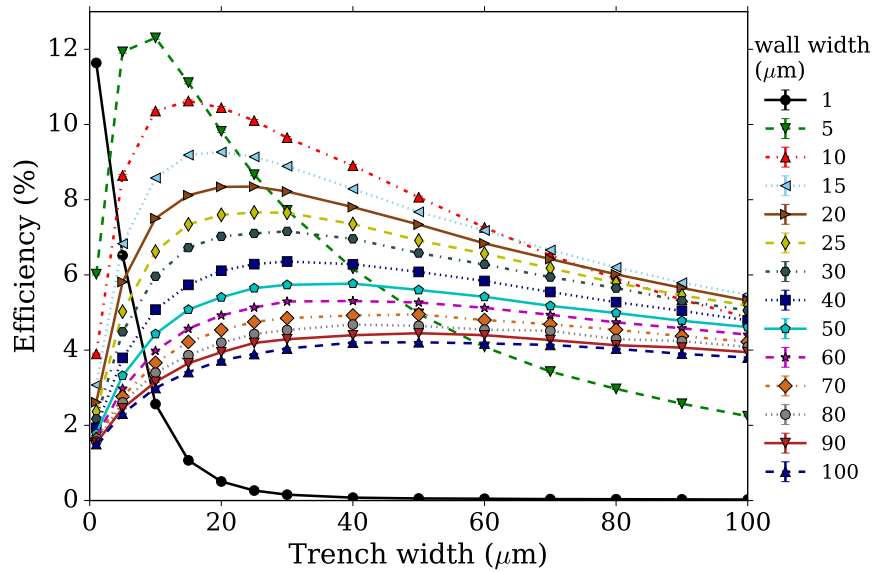
Reactant	Half life (s)	Number of α particles in 10 μs	Most-probable α energy (MeV) (abs. %)
^{235}U	2.22×10^{16}	1.41	4.40 (57.73)
^{238}U	1.41×10^{17}	0.22	4.20 (79.00)
^{232}Th	4.42×10^{17}	0.045	4.01 (78.20)

1599 6.5.3 Hydrogenous MSNDs

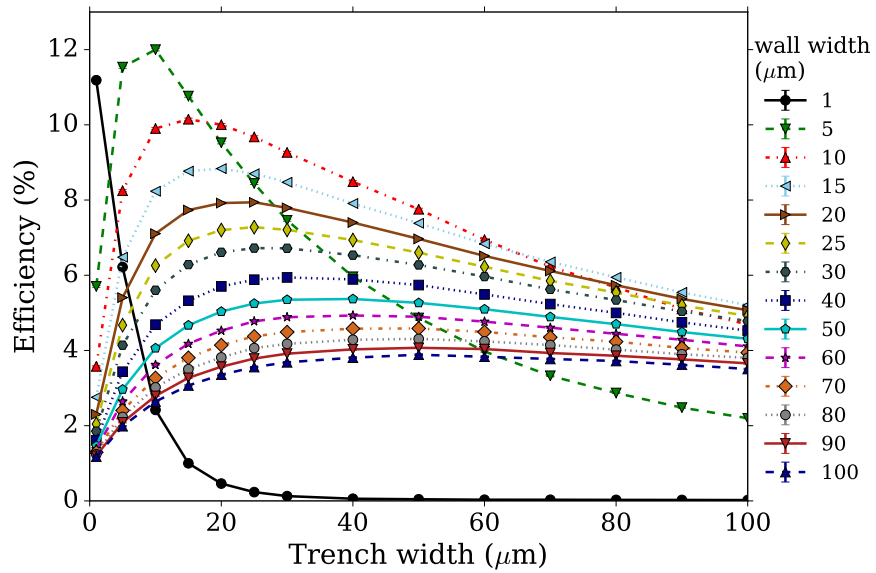
1600 Trench-Wall Optimization at 300-keV LLD

1601 At 300-keV LLD, the intrinsic neutron detection efficiencies of the 2-cm long H-MSNDs with
 1602 different trench and wall widths were computed in Geant4 and MCNP6, and the results are
 1603 shown in Fig. 6.11. Results of the two codes agree well, and the slight differences may be

1604 caused by the different cross-section libraries (Section 6.3.1). With 20- μm trench and 10- μm
 1605 wall widths, the efficiency of about 10% was predicted.



(a) Geant4 results



(b) MCNP6 results

Figure 6.11: The Geant4- and MCNP6-computed intrinsic neutron detection efficiencies of the 2-cm long H-MSNDs with different trench and wall widths. A 300-keV LLD was set.

1606 **NEPHDs at 300-keV LLD**

1607 Shown in Fig. 6.12 are the Geant4- and MCNP6-computed NEPHDs of the 2-cm H-MSND
1608 with 20- μm trench and 10- μm wall widths. On average, about half of the neutron energy
1609 is transferred to the recoil proton. Because the most-probable energy of fission-spectrum
1610 neutrons is about 1 MeV, the corresponding proton energy is about 500 keV, and, hence,
1611 a peak at about 500 keV exists. Because the energy distribution of the recoil proton is
1612 relatively uniform from the neutron energy to zero, in the lower part of the curve, protons
1613 from more higher-energy neutrons can contribute, and, hence, the distribution accumulates
1614 in the low energy part.

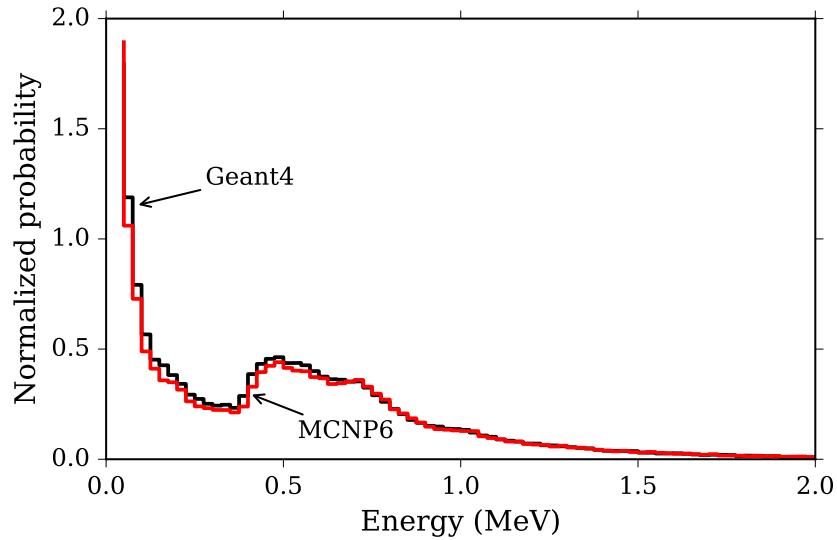


Figure 6.12: The Geant4- and MCNP6-computed NEPHDs of the 2-cm long H-MSND with 20- μm trench, 10- μm wall widths.

1615 **Efficiencies of the H-MSND Array at 300-keV LLD**

1616 With 20- μm trench and 10- μm wall widths, the Geant4- and MCNP-computed intrinsic
1617 neutron detection efficiencies of the H-MSNDs with different lengths are shown in Figure 6.13.
1618 A 300-keV LLD was applied. The efficiency saturates at about 26%.

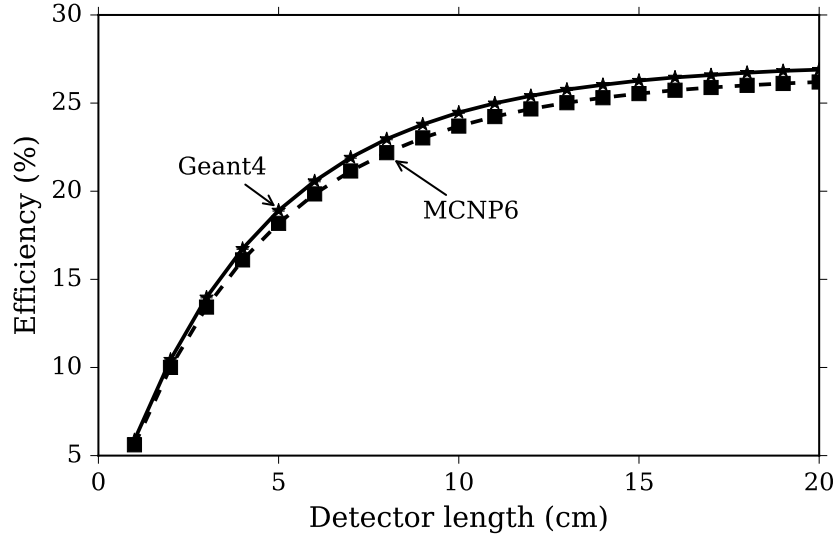


Figure 6.13: The Geant4- and MCNP6-computed neutron detection efficiencies of the H-MSNDs with different lengths. The 300-keV LLD was set. The H-MSNDs were with 20- μm trench and 10- μm wall widths.

1619 **Trench-Wall Optimization at S/N 100**

1620 Table 6.4 summarizes the trench and wall widths of the 2-cm long H-MSNDs that yielded
 1621 intrinsic neutron detection efficiencies larger than 2% . The LLDs were set to achieve an
 1622 S/N ratio of 100 based on the neutron and the gamma event PHDs computed by Geant4.
 1623 The H-MSND with 60- μm trench and 40- μm wall widths yields the best efficiency of 2.47%,
 1624 where the 1.2-MeV LLD is set to achieve an S/N ratio of 100.

Table 6.4: The trench and wall widths of the 2-cm long H-MSNDs that yielded neutron detection efficiencies (in percent) above 2% at the LLD settings that achieved S/N ratio of 100. The LLD settings in MeV are shown in the parentheses.

Trench (μm)	Wall (μm)				
	25	30	40	50	60
40	2.01 (1.225)	2.21 (1.250)	2.21 (1.325)		
50		2.37 (1.175)	2.20 (1.300)	2.15 (1.350)	
60	2.04 (1.125)	2.28 (1.150)	2.47 (1.200)	2.29 (1.275)	2.04 (1.350)
70		2.35 (1.100)	2.41 (1.175)	2.25 (1.250)	2.11 (1.300)
80		2.18 (1.100)	2.36 (1.150)	2.32 (1.200)	2.09 (1.275)
90			2.30 (1.125)	2.20 (1.200)	2.11 (1.250)
100			2.18 (1.125)	2.15 (1.200)	2.14 (1.200)

1625 **Neutron and Gamma Event PHDs at S/N 100**

1626 Figure 6.14 shows the Geant4-computed neutron and gamma event PHDs of the 2-cm long
1627 H-MSND with the optimized 60- μm trench and 40- μm wall widths. The peak of the NEPHD
1628 is beyond 1 MeV.

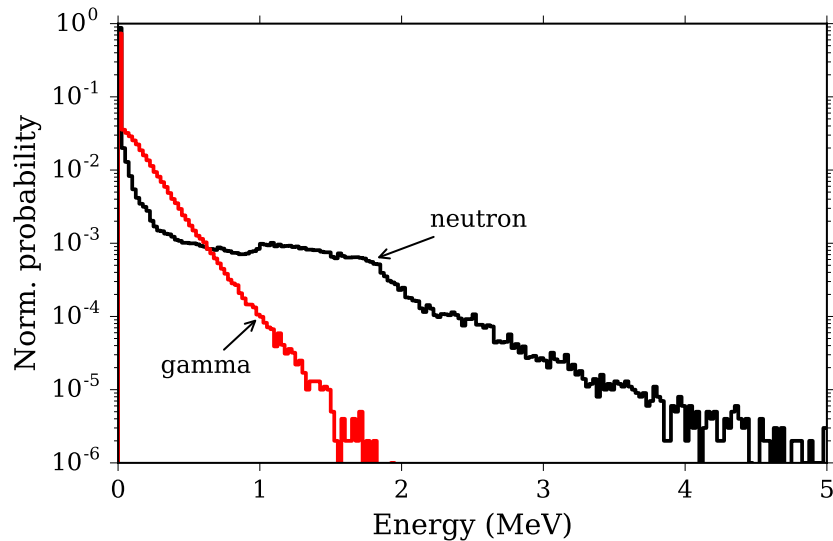


Figure 6.14: The Geant4-computed neutron and gamma event PHDs of the 2-cm long H-MSND with 60- μm trench and 40- μm wall widths.

1629 **Efficiencies of the H-MSND array at S/N 100**

1630 With 60- μm trench and 40- μm wall widths, the neutron-detection efficiencies of the H-
1631 MSNDs with different lengths are shown in Fig. 6.15. The LLDs were set to achieve S/N
1632 ratio of 100. The maximum efficiency of about 9.6% is predicted at the length of 20 cm.

1633 **6.6 Summary**

1634 Performance of the actinide MSNDs and the H-MSNDs for the TREAT hodoscope was
1635 evaluated in Geant4 and MCNP6. The actinide MSNDs allow high LLD settings due to the
1636 energetic fission fragments, while paraffin wax in the H-MSNDs leads to more fast neutron
1637 interactions.

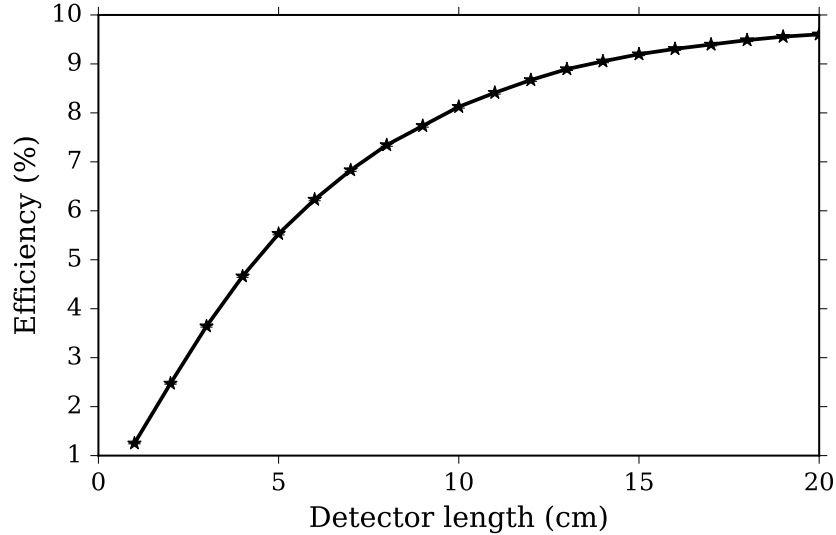


Figure 6.15: The Geant4-computed neutron detection efficiencies of the H-MSNDs vary with length. The H-MSNDs had the optimized 60- μm trench and 40- μm wall widths. The LLDs were set to achieve an S/N ratio of 100 based on the gamma event PHDs.

1638 Actinide MSNDs filled with ^{235}U , natural uranium, and ^{232}Th were evaluated in Geant4
 1639 using the fission fragment generator. With the LLD set to 5 MeV, the intrinsic neutron-
 1640 detection efficiency of the ^{235}U -filled MSNDs was 1.2% for a 2-cm device length and saturated
 1641 at 2.6% for lengths beyond 14 cm, where 20- μm trench and 10- μm wall widths were assumed.
 1642 The deposited energy in ^{235}U predicted by Geant4 was smaller than the MCNP6-predicted
 1643 value by about 0.073 MeV. The efficiencies of the ^{235}U -filled MSNDs acted as the lower
 1644 limits of the ^{235}Np -filled devices, which are preferred due to their insensitivity to the slow
 1645 neutrons. The MSNDs filled with natural uranium and thorium were predicted to have
 1646 efficiencies lower than the 1%.

1647 With the LLD set to 300 keV, Geant4 and MCNP6 predicted an efficiency of about 10%
 1648 for a 2-cm long H-MSND with 20- μm trench and 10- μm wall widths and an efficiency of
 1649 about 26% for a detector length of 20 cm. For an LLD set to achieve an S/N ratio of 100
 1650 when including gamma-ray noise, the best-case, Geant4-predicted efficiencies were 2.5% and
 1651 9.6% for 2-cm and 20-cm long devices with 60- μm trench and 40- μm wall widths.

Chapter 7

Micro-Pocket Fission Detectors

Micro-Pocket Fission Detectors (MPFDs) are in-core neutron detectors for TREAT, which can be operated in pulse mode and use the large amount of deposited energy by the fission fragments to separate neutron pulses from other in-core radiation. While for the largest TREAT transients, i.e., neutron flux in the order of $10^{17} \text{ cm}^{-2}\text{s}^{-1}$, the pulse mode may not be suitable due to the dead time count loss, the electron collection process in the MPFDs still needs to be quantified to interpret the measurements and to optimize future designs. In this chapter, a Garfield-based computational tool is explored to evaluate the electron motion in MPFDs, and the gained experiences in the modeling process are detailed. Preliminary results of the MPFD evaluation are presented.

7.1 MPFD Physics

The schematic of the MPFD developed for Idaho National Laboratory is shown in Fig. 7.1. It is a miniature fission chamber designed to monitor the neutron flux at a point inside the core. The chamber is typically filled with argon gas at a pressure of 30 psig (or 3.04 atm), and in this work, a gas temperature of 50 °C was assumed. Two electrode wires, each with a diameter of 0.255 mm, penetrate the gas volume to create electric field. A thin, fissile layer is deposited in the gas volume to convert in-core neutrons. A typical thickness of the fissile

1670 layer is in the nm range [46] and can be adjusted for different applications.

1671 In a neutron event, one nucleus of the fission fragment pair enters the gas and deposits
1672 approximately a few MeV of energy. Along the path of the fission fragment, ionized electron-
1673 ion pairs are generated. The charge carriers are drifted under applied electric field and, at
1674 the same time, diffuse. The motion of the charge carriers induces current in the external
1675 circuit, which is processed to generate a pulse.

1676 The electron collection process in MPFDs needs to be quantified to assist the devel-
1677 opment. Because electrons move thousands of times faster than ions, pulse-mode MPFDs
1678 are usually connected to an RC circuit to truncate the signal after electrons are collected.
1679 Therefore, the time to collect electrons from a neutron pulse event needs to be determined
1680 in order to select a suitable RC circuit. In addition, pulse-mode detectors are designed to
1681 minimize dead time count loss. Ideally, the electrons from one neutron event are collected,
1682 and the signal is processed before the next neutron event occurs. To accommodate a range
1683 of in-core neutron flux levels, the reaction rate of the neutron-converting, fission reaction
1684 can be adjusted by changing the thickness of the fissile layer. A faster electron collection
1685 allows a thicker fissile layer to produce higher count rate while maintaining a small dead
1686 time, which reduces the relative error. Overall, the thickness of the fissile layer, the speed
1687 of the electron collection, and the electronics system need to be matched to achieve optimal
1688 performance in TREAT and other reactor cores.

1689 **7.2 Computational Scheme**

1690 To simulate the electron collection process in MPFDs, a Garfield-based, computational
1691 scheme [76] was used, as shown in Fig. 7.2. The scheme consists of the following codes:
1692 Garfield++ (version v1r0)[36], Gmsh (version 3.0.6) [37], Elmer (version 8.3) [38], and stop-
1693 ping and range of ions in matter (SRIM) (version 2008.04) [39].

1694 Gmsh was used to construct the gas volume (shown in Fig. 7.1) and to generate the finite-
1695 element mesh for Elmer. The Gmsh output was converted to Elmer-suitable format using
1696 the ElmerGrid module, and the electric field was calculated by the ElmerSolver module

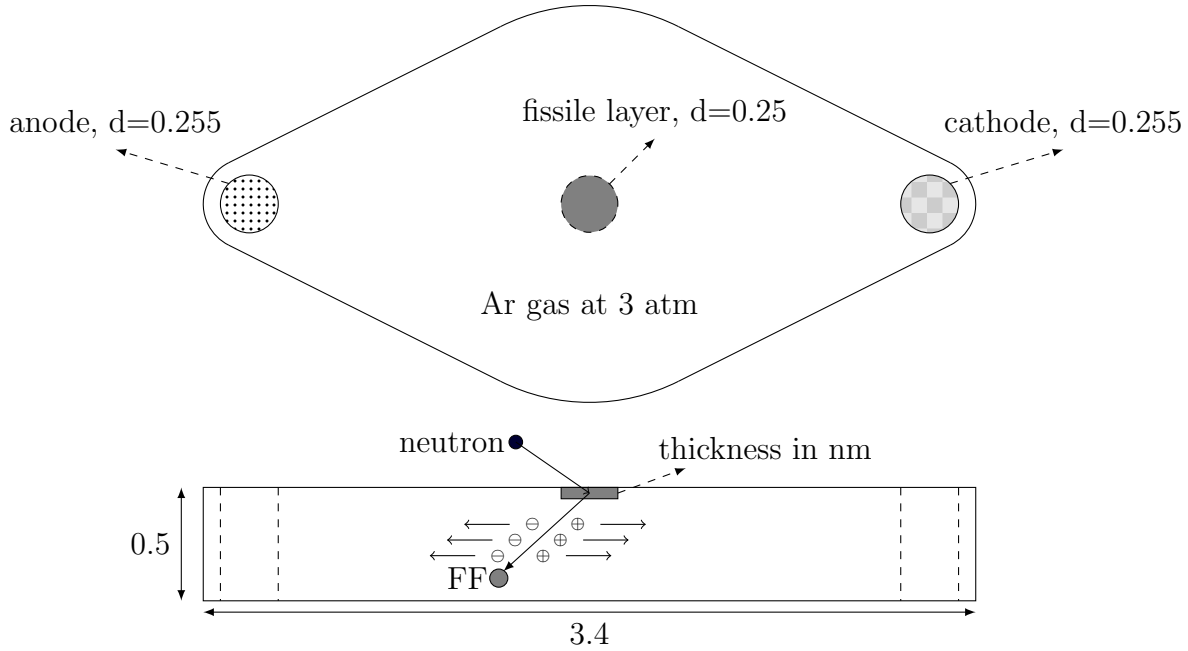


Figure 7.1: Schematic of the MPFD developed for Idaho National Laboratory. Dimensions are in mm.

1697 using a finite-element method. The Elmer outputs were imported into Garfield++ via the
 1698 `ComponentElmer` class.

1699 SRIM was used to generate the energy loss tables of a pair of representative fission
 1700 fragments, $^{95}_{38}\text{Sr}$ and $^{139}_{54}\text{Xe}$. These tables were imported into Garfield++ using the `TrackSrim`
 1701 class.

1702 With the inputs from Elmer and SRIM, Garfield++ simulated the ionization of fission
 1703 fragments in gas and created electron clusters along its path based on the deposited energy
 1704 and the user-supplied work function (Eq. (2.11)) and fano factor (Eq. (2.12)) of the gas.
 1705 Then, the drift of the electrons in the clusters under the Elmer-computed electric field and
 1706 the diffusion process were simulated in Garfield++ using algorithms based on the Monte
 1707 Carlo method. During the electron transport, the induced current generated by the electron
 1708 movement was calculated simultaneously using the Shockley-Ramo theorem.

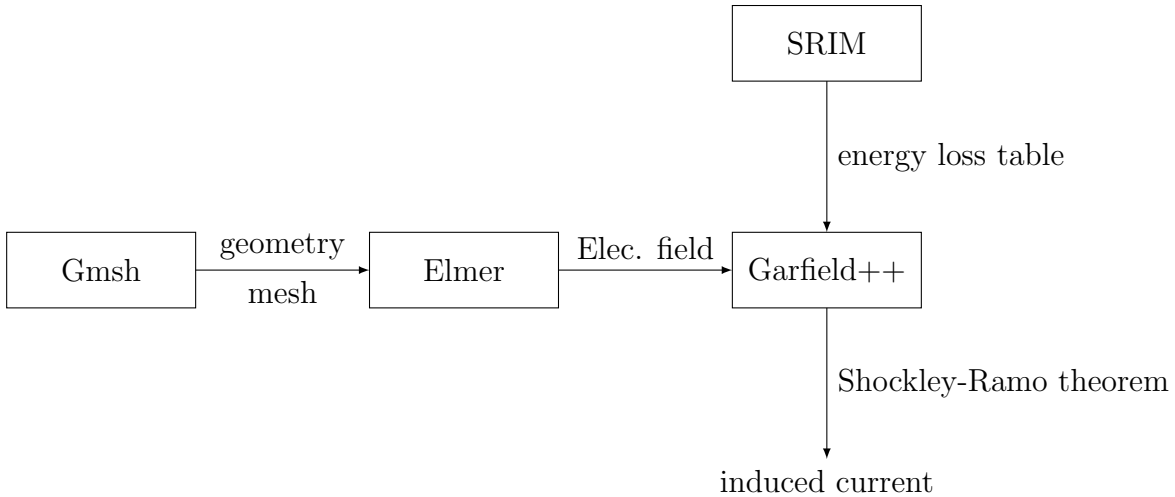


Figure 7.2: The computational scheme to evaluate MPFDs.

1709 7.3 Gmsh

1710 7.3.1 Running Modes

1711 Gmsh is an open-source, three-dimensional (3-D) finite-element grid generator with a built-in
 1712 CAD engine and postprocessor. Gmsh can be run in an interactive graphical user interface
 1713 (GUI) mode or the non-interactive batch mode. The GUI mode is useful to examine the
 1714 geometry and the mesh quality. The GUI mode is built on the Fast Light Toolkit (FLTK) [77]
 1715 configured with OpenGL support. Thus, to enable the GUI mode, the FLTK module needs
 1716 to be pre-installed, and the Gmsh source code needs to be compiled with the GUI-support
 1717 options on.

1718 The GUI mode greatly facilitates model construction. Geometry entities can be added
 1719 to the model easily through the GUI interface, and the software automatically adds the
 1720 corresponding Gmsh commands to the underlining plaintext `.geo` script.

1721 However, the GUI mode is limited in that it does not support all the Gmsh commands.
 1722 For full functionality, *batch* mode must be used instead. To build the model in batch mode,
 1723 Gmsh uses C++-like commands, which are hard coded by the user in the `geo` text file. In
 1724 particular, the batch mode supports user-defined functions, loops, and if conditions, which
 1725 are useful for parameterization. In this study, both modes were used.

1726 **7.3.2 Geometry Construction**

1727 The geometry modeling in Gmsh consists of the elementary and the physical entities. To
1728 define the elementary geometry, Gmsh provides the basic built-in and the more advanced
1729 **OpenCASCADE** geometry kernels. The two kernels are not fully compatible, and, hence, it
1730 is recommended to build the model using either of the kernels, which is specified by the
1731 **SetFactory** command. The built-in kernel builds the geometry in a bottom-up flow by suc-
1732 cessively defining points, lines (by connecting points), surfaces (by line loops), and volumes
1733 (by surface loops).

1734 The more advanced **OpenCASCADE** kernel was used to construct the MPFD geometry
1735 shown in Fig. 7.1. To enable the kernel, the *Open CASCADE* software [78] needs to be
1736 pre-installed. This kernel implements constructive solid geometry and provides additional
1737 commands to define lines, surfaces, volumes, and boolean operations that are not avail-
1738 able in the built-in kernel. Specifically, standard volumes can be directly defined using the
1739 **OpenCASCADE** kernel. If a volume is defined in this way, Gmsh still implicitly constructs
1740 the underlying points, lines, and surfaces that form the volume to mesh the geometry. The
1741 identification numbers of these underlying geometry entities can be found by using the GUI
1742 mode and are needed to define the **characteristic length** as discussed bellow. The non-
1743 standard volumes can be defined through line loops using the **ThruSections** command in
1744 the **OpenCASCADE** kernel.

1745 When an elementary point is defined explicitly, the mesh element size at the point can be
1746 specified via the **characteristic length** input parameter at initialization. For the points
1747 that are implicitly constructed, this parameter can be specified using the **Characteristic**
1748 **Length** function using the associated identification numbers found using the GUI mode.

1749 The physical entity is a group of elementary geometry entities. While not required,
1750 physical entities are defined to facilitate the mesh generation in Gmsh. If defined, the
1751 output mesh only contains the elements that belong to the physical entities. In addition, the
1752 physical entities bridge Gmsh and Elmer. When the Gmsh output is imported into Elmer to
1753 calculate the electric field, the physical surface defined in Gmsh corresponds to the **target**

1754 `boundaries` entity in Elmer to apply boundary condition. The physical volume corresponds
1755 to the `body` entity in Elmer to specify governing equation and to define the material relative
1756 permittivity (or dielectric constant).

1757 **7.3.3 Geometry Meshing**

1758 Gmsh generates a mesh from the bottom up. Lines are discretized first, and, then, the
1759 line mesh is used to mesh the surfaces. Finally, the surface mesh is used to mesh the
1760 volumes. The *unstructured* or the *structured* meshing algorithms for 3-D geometry are
1761 provided. The unstructured algorithms generate tetrahedra, while the structured algorithms
1762 generate tetrahedra, hexahedra, prisms or pyramids depending on the type of the surface
1763 meshes.

1764 The `Delaunay` (which is the default) and the `Frontal` 3-D unstructured meshing algo-
1765 rithms are implemented, and the quality of the elements produced by the two algo-
1766 rithms are comparable [79]. Other mesh algorithms exist that are not fully documented
1767 in the Gmsh reference manual [79]. For instance, the `Delaunay`, `New Delaunay`, `Frontal`,
1768 `Frontal Delaunay`, `Frontal Hex`, `MMG3D`, and `R-tree` mesh algorithms can be selected via
1769 the `Mesh.Algorithm3D` option. The `del3d`, `front3d`, `mng3d`, and `pack` mesh algorithms
1770 can be specified in the command line via the `algo` option. The unspecified mesh algorithms
1771 may be the structured type or in the experimental phase. In addition, the built-in and the
1772 `Netgen` algorithms are provided to optimize the mesh quality.

1773 The size of the mesh elements can be defined in three ways. The first is from the character-
1774 istic lengths of the elementary points. If the `Mesh.CharacteristicLengthFromCurvature`
1775 option is set, the mesh is adapted with respect to the curvature of the geometrical entities.
1776 Finally, the size can also be specified by defining fields. These three methods can work
1777 simultaneously. In this case, the smallest element size is selected at any given point. The
1778 first two methods were used in this work.

1779 **7.3.4 MPFD Gmsh Model**

1780 In this work, the `OpenCASCADE` kernel was used to model the MPFD geometry shown in
1781 Fig. 7.1. The global gas volume was constructed using the `ThruSections` command by
1782 defining the top and the bottom line loops. The two wire volumes were constructed by
1783 the `Cylinder` command, and, then, the two wire volumes were subtracted from the global
1784 gas volume using the difference boolean operation. The resulting gas volume was set as a
1785 physical volume. This physical volume was later used in `ElmerSolver` to assign governing
1786 equation and the relative permittivity of argon gas. The cylinder surfaces of the two wire
1787 volumes were set as two physical surfaces, respectively. The physical surfaces were used in
1788 `ElmerSolver` to specify boundary condition, i.e., to apply voltage on the electrodes. The
1789 default `Delaunay` mesh algorithm and the built-in mesh-optimize algorithm were used to
1790 mesh the geometry.

1791 The characteristic length of 0.02 was applied to all the elementary points to produce
1792 elements with sufficient quality required by `Garfield++`. Because the elementary points
1793 associated with the wire volumes were created implicitly by `Gmsh`, the `Characteristic`
1794 `Length` function was used to set the value of 0.02 at these points, whose identification num-
1795 bers were found using the GUI mode. The `Mesh.CharacteristicLengthFromCurvature`
1796 option was set.

1797 With all the commands written in a `geo` file, `Gmsh` was run with the `-3 -order 2`
1798 command line options to generate a 3-D mesh with second-order tetrahedral elements. The
1799 second-order elements are supported in `Garfield++`. A `msh` file was generated to describe
1800 the meshed geometry. The meshed geometry of the MPFD is shown in Fig. 7.3.

1801 **7.4 Elmer**

1802 The `Gmsh`-generated `msh` file was used in `Elmer` to calculate the electric field. `Elmer` is an
1803 open-source, finite-element software package for the solution of partial differential equations.
1804 It consists of several modules, and the the `ElmerGrid` and the `ElmerSolver` modules were

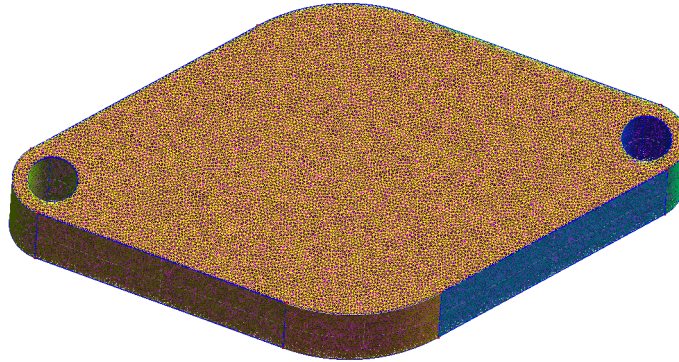


Figure 7.3: The meshed MPFD geometry using Gmsh.

1805 used in this study.

1806 **7.4.1 ElmerGrid**

1807 ElmerGrid was used to convert the `msh` file to the format readable for ElmerSolver. The
1808 command used was

```
1809 ElmerGrid 14 2 GmshFile.msh -autoclean.
```

1810 The option 14 indicated the input is from Gmsh, and the option 2 stated the output is for
1811 ElmerSolver. `GmshFile.msh` was the mesh file generated by Gmsh. The `autoclean` flag re-
1812 numbered the physical surfaces and the physical volumes defined in Gmsh starting at one and
1813 with unit increment following the defining sequence. The physical surfaces and the physical
1814 volumes are re-numbered independently. Hence, the identification number of the defined
1815 physical gas volume in Gmsh was re-set to one, and this physical volume corresponded to
1816 `body 1` in ElmerSolver to specify the governing equation and dielectric constant of argon
1817 gas. The identification numbers of the two wire physical surfaces were re-numbered to one
1818 and two, respectively. These two physical surfaces corresponded to `target boundaries 1`
1819 and `2` in ElmerSolver, respectively, to assign specific boundary condition, i.e., applying
1820 different voltages on electrodes.

1821 After applying the aforementioned command, `ElmerGrid` created a subdirectory contain-
1822 ing the generated `mesh.boundary`, `mesh.elements`, `mesh.header`, and `mesh.nodes` files.

1823 7.4.2 ElmerSolver

1824 `ElmerSolver` reads a text `sif` file, which specifies the location of the `ElmerGrid` outputs,
1825 the applied voltages at the electrodes via the `target boundaries` keyword, the relative
1826 permittivity of argon gas, the electrostatic solver to calculate the electric field, the assignment
1827 of the governing equation, and the material properties of the gas `body`. The used `sif` file is
1828 shown in Appendix B.

1829 Two electric field maps were generated, in which 100-V and 1-V voltages were applied
1830 to anode wire, respectively, and the cathode was grounded. The field map with 100-V bias
1831 on anode was used in `Garfield++` to drift electrons, and the map with 1-V anode was the
1832 weighting field to calculate the induced current used in the Shockley-Ramo theorem. The
1833 calculated field maps were written in the generated `result` files.

1834 Shown in Fig. 7.4 is the Elmer-computed electric field inside the gas volume with 100-V
1835 bias on the anode wire. The plot was generated in `Garfield++` using the `ViewField` class.
1836 The maximum magnitude is about 900 V/cm near the electrode wires. Shown in Fig. 7.5 is
1837 the weighting field, which has the same shape as Fig. 7.4.

1838 7.5 Garfield++

1839 `Garfield++` is a toolkit written in C++ mainly used to simulate the electron transport
1840 in gaseous detectors. The electron transport properties in gas mixtures under different
1841 electric and magnetic fields are calculated by the built-in interface to the Magboltz program
1842 [45], and the computed properties in argon gas were validated against experimental values
1843 [80]. In particular, the Magboltz-predicted electron drift speed was compared to an analytic
1844 approximation, and the details can be found in Appendix C. The main code structure of a
1845 `Garfield++` application is shown in Fig. 7.6.

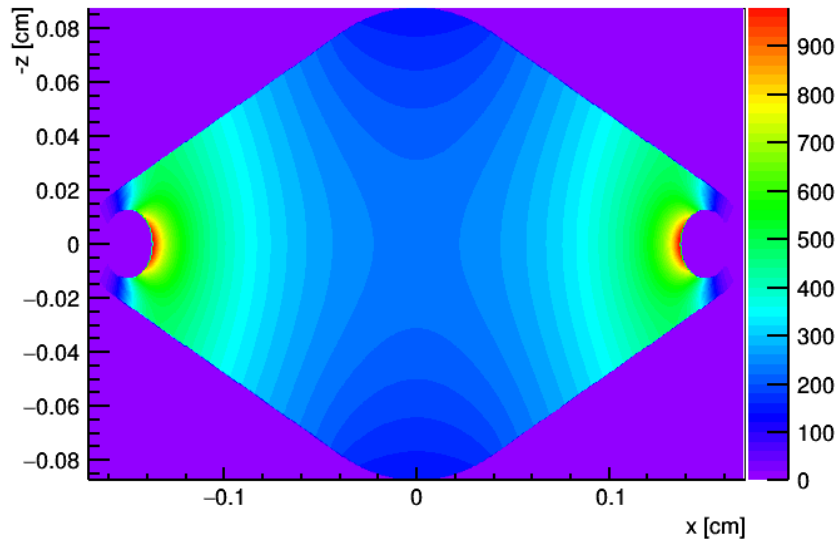


Figure 7.4: The computed electric field (V/cm) inside the gas volume.

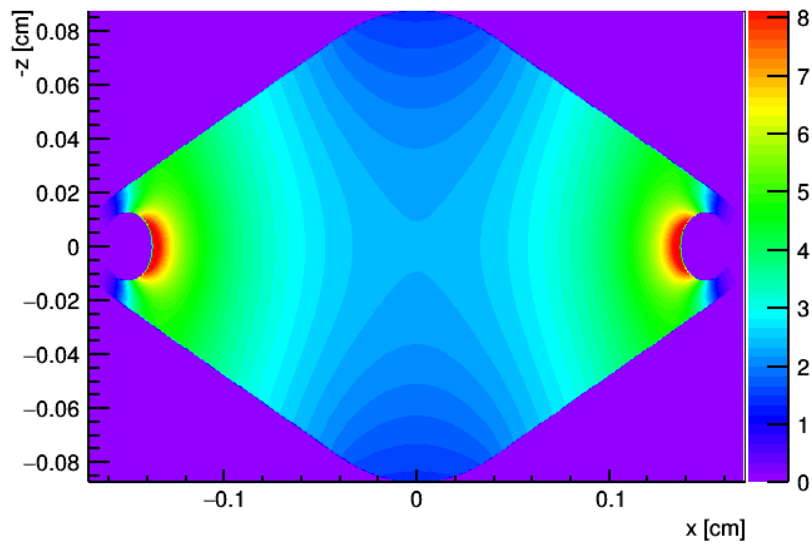


Figure 7.5: The computed electric weighting field (V/cm) inside the gas volume.

1846 **7.5.1 MediumMagboltz Class**

1847 The `MediumMagboltz` class was used to define the argon gas at a pressure of 30 psig and a
 1848 temperature of 50 °C. The density of argon gas at this condition was calculated automatically
 1849 by Garfield++ using the ideal gas law.

1850 The electron transport properties in gas are computed by the underlying Magboltz

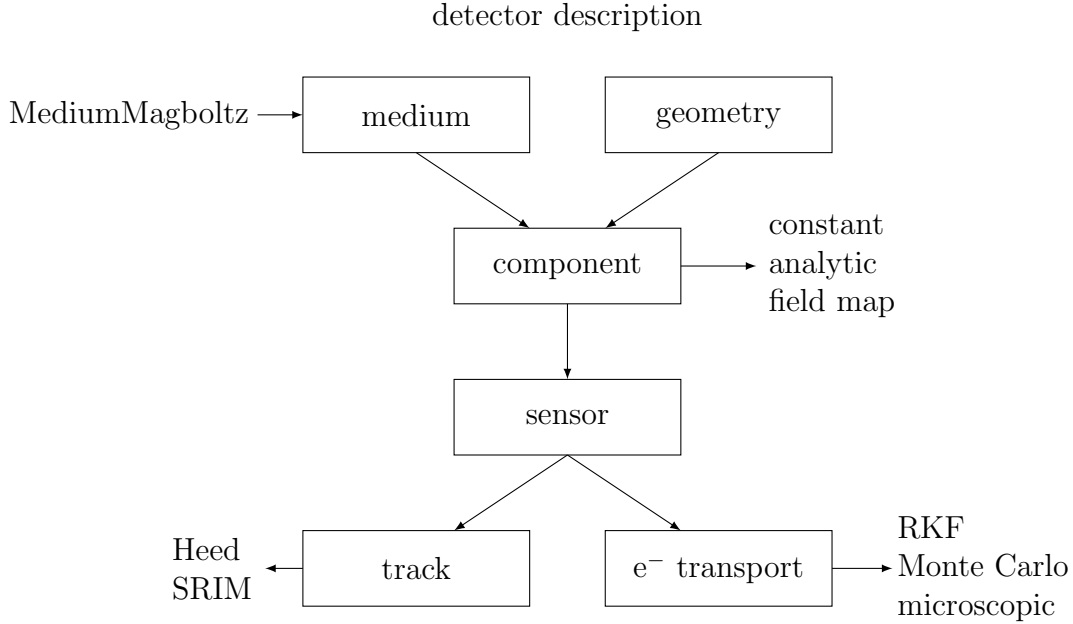


Figure 7.6: Code structure of a Garfield++ application.

1851 program. If the electrons are tracked by the Monte Carlo integration algorithm, an elec-
 1852 tron transport table needs to be calculated using the `GenerateGasTable` function in the
 1853 `MediumMagboltz` class. This table provides the drift velocity, longitudinal and transverse
 1854 diffusion coefficients, attachment and Townsend coefficients of electron tracking in the de-
 1855 fined gas as a function of electric and magnetic fields. In this study, no magnetic field existed,
 1856 and, thus, the generated table was one-dimensional and solely depended on electric field.

1857 To generate the table, the range of the electric field, the number of grid points spanning
 1858 the electric-field range, and the number of electron collisions inside the gas need to be
 1859 specified. Because it is time-consuming to generate the table, in this work, a coarse table
 1860 was generated with 50 grid points uniformly distributed between zero and 1500 V/cm for the
 1861 electric field using a collision number of 10^8 . The Monte Carlo tracking of electrons using
 1862 this coarse table was only used in the parallel plate example (shown in Appendix C) and to
 1863 examine the parallelization scheme. The effects of these parameters on the induced current
 1864 need further investigation.

1865 The MPFD was evaluated using the more-accurate microscopic algorithm, which is di-
 1866 rectly based on the electron scattering cross sections with the gas atom in the Magboltz

1867 database. Hence, a gas table is not necessary for the microscopic algorithm. Because the
 1868 statistics error introduced in generating the table is avoided, the microscopic treatment is
 1869 more accurate than the Monte Carlo integration algorithm.

1870 7.5.2 Component Classes

1871 In the component classes, the geometry is defined, the initialized `MediumMagboltz` gas is
 1872 used to fill the geometry, and the electric field inside the gas volume is specified, i.e., the
 1873 model is described. The constant, analytic, and field map component classes are provided.
 1874 The constant component class defines a constant electric field. The analytic component class
 1875 calculates simple electric fields created by two-dimensional wires, planes, or tubes using the
 1876 capacitance matrix method. In these two component classes, the geometry must be defined
 1877 in Garfield++ by using the basic `GeometrySimple` or the more advanced `GeometryRoot`
 1878 classes.

1879 For more complicated electric fields, the field map component classes are provided to read
 1880 the electric field computed by other means (e.g., Elmer), which are summarized in Table 7.1.
 1881 When the field-map files are imported into Garfield++ via the field map component class,
 1882 the geometry defined in the third-party software is also constructed. Therefore, it is not
 1883 necessary to define the geometry. In this work, the `ComponentElmer` class was used to read
 1884 the result files generated by Elmer. The defined argon gas was used to fill the gas volume,
 1885 i.e., body 1 in Elmer.

Table 7.1: Field map component classes to read results from different softwares.

Software	Component class
Ansys	<code>ComponentAnys121</code> for 2-D geometry
	<code>ComponentAnsys123</code> for 3-D geometry
Synopsys TCAD	<code>ComponentTcad2d</code> for 2-D geometry
	<code>ComponentTcad3d</code> for 3-D geometry
Elmer	<code>ComponentElmer</code>
CST	<code>ComponentCST</code>
COMSOL	<code>ComponentComsol</code>

1886 **Mesh Quality**

1887 Garfield++ includes a built-in capability to check the imported finite element quality. When
1888 an electron is tracked in the gas, the finite element that contains the electron position is
1889 searched using the `FindElement13` function to calculate the electric field. If the quality
1890 of the located finite element does not meet the criteria, the user is alerted. Then, the
1891 electron that resides in the tracking geometry is killed due to the poor-quality element, which
1892 introduces error. Hence, a field map with sufficient quality is necessary for correct simulation.
1893 It was tested that in the Gmsh meshing of MPFD geometry, defining elementary points
1894 with characteristic length of 0.02 and turning on the `CharacteristicLengthFromCurvature`
1895 option can generate finite elements with sufficient quality.

1896 **Accelerating Finite Element Searching**

1897 Although the settings and options described above had led to electric field maps with high
1898 quality, the number of elements in the map was large (and, hence, computations became
1899 excessively costly). Because the original searching algorithm in the `FindElement13` function
1900 is not efficient, it was time-consuming to locate the element. In the default searching algo-
1901 rithm, at a new electron position, it is first checked whether the new position is in the caching
1902 box of last element. If not, a search from the first element in the map is performed, and at
1903 each iteration, the caching box of the new element is computed. Hence, with large number
1904 of elements, which is required for sufficient mesh quality, looping over all the elements is
1905 computationally expensive.

1906 To improve the performance, the optimized search techniques were used [81]. In the
1907 optimized algorithm, the caching box of each element is calculated before the simulation.
1908 If an electron leaves the old element, the neighbor elements are first checked instead of
1909 searching from the first element. In addition, the tetrahedral tree structure is used. These
1910 techniques have been implemented in the Garfield++ source code; however, they are not
1911 documented in the user guide [82]. The new search algorithm was enabled using the
1912 `EnableTetrahedralTreeForElementSearch` function in the `ComponentElmer` class.

1913 7.5.3 Track Classes

1914 Garfield++ provides two classes for simulating the energy loss of charge particle in gas,
1915 namely the `TrackHeed` and the `TrackSrim` classes. The `TrackHeed` class uses the HEED
1916 program [83] to simulate the ionization of charged particles with relativistic energy using
1917 the photo-absorption ionization model, i.e., the energy loss is minimal compared to the
1918 initial kinetic energy. This class is mainly used to simulate detectors for high-energy physics
1919 experiments.

1920 The `TrackSrim` class was used in this work. This class reads a SRIM-generated table
1921 that describes the energy loss of ions in a gas to simulate the ionization of fission fragment.
1922 The SRIM tables of $^{95}_{38}\text{Sr}$ and $^{139}_{54}\text{Xe}$ in argon gas were calculated. This representative fission
1923 fragment pair was selected because of the high fission yield of about 0.05 [84], i.e., at the
1924 peak of the ^{235}U fission fragment distribution. Because argon gas has a density of $1.784 \times$
1925 10^{-3} g/cm³ at 0 °C and one atm, at 50 °C and 30 psig, according to the ideal gas law, the
1926 density was set to 4.586×10^{-3} g/cm³ in the SRIM-generated tables.

1927 The SRIM tables were imported into Garfield++ using the `TrackSrim` class. In this
1928 class, the work function and Fano factor of argon gas were set to 27 and 0.19 eV, respectively
1929 [44]. The atomic and mass numbers of Ar were set to 18 and 40, respectively. The initial
1930 kinetic energies of $^{95}_{38}\text{Sr}$ and $^{139}_{54}\text{Xe}$ were set to 101.9 and 69.8 MeV, respectively [23]. One
1931 thousand $^{95}_{38}\text{Sr}$ and one thousand $^{139}_{54}\text{Xe}$ ions were simulated. It should be noted that it is an
1932 approximation to simulate one representative fission pair, and in the future work, a more
1933 comprehensive fission fragment distribution needs to be studied. The fission fragments were
1934 born uniformly in the fissile layer (shown in Fig. 7.1) at time zero with directions sampled
1935 isotropically into the gas-facing half space.

1936 The `TrackSrim` class simulates the ionization of a fission fragment in the gas and creates
1937 electron *clusters* along its path, where a cluster is a group of electrons with same initial
1938 condition. In the calculations, along the track of a fission fragment, the maximum number
1939 of clusters was set to 5000 [85]. For each cluster, the (x, y, z) coordinate, the time of creation,
1940 the number of electrons (in the cluster), the energy deposited to create the cluster, and the

1941 ion's energy when the cluster was created can be retrieved using the `GetCluster` function.
1942 This cluster information is then used thereafter to initialize the electrons to be transported.

1943 It was impractical (and probably not necessary) to transport all the electrons in the
1944 clusters to calculate the induced current, which requires that a compromise is made when
1945 considering the computing power available and the accuracy desired. In at least one past
1946 study, just a single electron per cluster was transported to calculate the signal with appar-
1947 ently sufficient accuracy [85]. In this study, the optimized element search techniques and the
1948 parallelized scheme (shown in the following) allowed tracking more electrons using the most-
1949 accurate (and time-consuming) microscopic tracking method for best accuracy. To evaluate
1950 the MPFD, 1% of the electrons in each cluster were transported to calculate a more-accurate
1951 shape of the induced current for future validation. According to the following MPFD re-
1952 sults, one percent corresponded to about 10 to 30 electrons per cluster. The induced current
1953 by these 1% electrons was re-factored by 100 to represent the total signal. The systematic
1954 error introduced by not tracking all the electrons has not been formally quantified and needs
1955 further investigation.

1956 **Fission Fragment Adjustment**

1957 It was reported that grouping the electrons into clusters introduces a bias [85]. When the
1958 fission fragment collides with an atom of the gas, the fragment is deflected. Over the whole
1959 path of the fission fragment, this deviation, measured by the lateral straggling in the SRIM
1960 table, is relatively small compared to the range. However, grouping the electrons into clusters
1961 in Garfield++ over-estimates the deviation.

1962 In the MPFD simulation, because the fission fragments were born in the fissile layer near
1963 the boundary of the gas volume, as a result of the over-estimated deviation, about 40%
1964 to 50% of the sampled fission fragments left the gas volume with only one or two clusters
1965 generated, which was a simulation artifact. To avoid this bias, sampling of the ionization of
1966 fission fragment in the gas was repeated until the number of clusters was larger than two.
1967 Thus, each of the two thousands simulated fission fragments ionized more than two clusters

1968 of electrons. It has been shown that with such a correction, the Garfield++ simulated
 1969 results still follow the range and straggling provided by SRIM [85], i.e., the fission fragment
 1970 adjustment does not introduce an extra bias.

1971 Cluster Time Adjustment

1972 Garfield++ neglects the time that a fission fragment takes to pass through the gas volume,
 1973 and for fission fragments that enter the gas volume at time zero, all the electron clusters are
 1974 created at time zero. For best accuracy, the cluster-creation time was adjusted taking into
 1975 consideration the flight time of the fission fragment [85].

1976 Specifically, the first cluster was created at time zero. Each of the following clusters was
 1977 created at time

$$t_i = \frac{\|\vec{P}_i - \vec{P}_{i-1}\|}{v_i} + t_{i-1}, \quad (7.1)$$

1978 where \vec{P}_i and \vec{P}_{i-1} were the coordinates of the i th and the $(i-1)$ th clusters, respectively,
 1979 and t_{i-1} was the creation time of the $(i-1)$ th cluster. The velocity of the fission fragment
 1980 v_i was calculated by

$$v_i = \sqrt{\frac{2E_a}{m}} \quad (7.2)$$

$$E_a = (E_{i-1} - dE_{i-1} + E_i)/2.$$

1981 m was the mass of the fission fragment. E_a was the average kinetic energy of the fission
 1982 fragment during the flight. After the $(i-1)$ th cluster was created, i.e., the start point of the
 1983 flight, the energy of the fission fragment was $E_{i-1} - dE_{i-1}$, where E_{i-1} was the kinetic energy
 1984 of the fission fragment when the $(i-1)$ th cluster was created, and dE_{i-1} was the energy
 1985 spent to create the $(i-1)$ th cluster. E_i was the energy of the fission fragment when the i th
 1986 cluster was created, i.e., the end point of the flight. These variables to calculate the adjusted
 1987 cluster-born time were provided by the `GetCluster` function in the `TrackSrim` class.

1988 **7.5.4 Electron Transport Classes**

1989 Garfield++ provides three different algorithms of increasing fidelity for tracking charge car-
1990 riers in the gas: Runge-Kutta-Fehlberg (RKF) integration, Monte Carlo integration (class
1991 name `AvalancheMC`), and a microscopic tracking technique (class name `AvalancheMicroscopic`).
1992 While the avalanche physics is implemented in the last two methods, it is not of importance
1993 in MPFDs. All the three methods can not simulate the electron recombination physics [85].
1994 The last two methods were used in this study to transport electrons.

1995 **Monte Carlo Integration**

1996 The Monte Carlo integration method can be used to track electrons or ions in gas using a
1997 table that contains the transport properties of the charge carrier. For electrons in gas, this
1998 table can be computed by the built-in interface to the Magboltz program, as discussed in
1999 Section 7.5.1, to provide the electron transport properties in most common gas mixtures.
2000 Based on the electron transport properties, the Monte Carlo integration method simulates
2001 the drift under electric field, diffusion, attachment, and Townsend processes. In addition,
2002 the `AvalancheMC` class has the `DisableDiffusion` function to exclude the simulation of
2003 the diffusion process, which may be used to analyze the effects of diffusion on the induced
2004 current.

2005 The ion transport table can not be directly calculated in Garfield++. In the Garfield++
2006 source code (version v1r0), ion tables for argon, carbon dioxide, helium, and neon gases at
2007 temperature 300 K are provided. While unneeded in this study, transport of other ions is
2008 possible by providing the necessary table.

2009 In a Monte Carlo step, a drift length $\Delta \mathbf{s} = \mathbf{v}_d \Delta t$ is computed. A Δt of 0.01 ns was used
2010 in this study. The drift speed \mathbf{v}_d at local electric field is calculated using Eq. (2.4). Then,
2011 a random diffusion step is sampled from three uncorrelated, Gaussian distributions with
2012 standard deviation $\sigma_L = D_L \sqrt{|\Delta \mathbf{s}|}$ for the component parallel to \mathbf{v}_d and standard deviation
2013 $\sigma_T = D_T \sqrt{|\Delta \mathbf{s}|}$ for the two transverse components. D_L and D_T are the corresponding diffu-
2014 sion coefficients. The drift and diffuse steps are added to construct the traveling length. The

2015 simulation of the diffusion process can be turned off using the `DisableDiffusion` function,
2016 which may be useful to analyze its effects on the induced current.

2017 In a Monte Carlo step, a drift length $\Delta \mathbf{s} = \mathbf{v}_d \Delta t$ is computed. A Δt of 0.01 ns was used
2018 in this study. The drift speed \mathbf{v}_d at local electric field is calculated using Eq. (2.4). Then, a
2019 random diffusion step is sampled from three uncorrelated Gaussian distributions with stan-
2020 dard deviation $\sigma_L = D_L \sqrt{|\Delta \mathbf{s}|}$ for the component parallel to \mathbf{v}_d and standard deviation
2021 $\sigma_T = D_T \sqrt{|\Delta \mathbf{s}|}$ for the two transverse components. D_L and D_T are the corresponding diffu-
2022 sion coefficients. The drift and diffuse steps are added to construct the traveling length. The
2023 simulation of the diffusion process can be turned off using the `DisableDiffusion` function,
2024 which may be useful to analyze its effects on the induced current.

2025 In this work, the Monte Carlo integration method was only used in the parallel plate
2026 example shown in Appendix C and to examine the parallelization scheme based on a coarse
2027 electron transport table.

2028 **Microscopic Tracking**

2029 The microscopic method can only track electrons. This method simulates the electron trans-
2030 port in gas using the Monte Carlo method based on the electron-molecule scattering cross
2031 sections provided by the Magboltz program. Hence, the electron transport table as used in
2032 the Monte Carlo integration method is not necessary. The statistical error introduced by
2033 use of the pre-generated table is avoided in the microscopic tracking method, which makes
2034 it more accurate than the Monte Carlo integration method.

2035 The detailed physics of the microscopic tracking method is not specified in the Garfield++
2036 user guide [82]. From the source code, the algorithm implemented by this method is like
2037 the Monte Carlo flow to transport neutrons, as stated in Section 3.2. Specifically, based on
2038 the cross section, the collision type of a colliding electron is sampled to be elastic, ioniza-
2039 tion, attachment, inelastic, excitation, super-elastic, one of several possible phonon-related
2040 scatterings, or coulomb scattering. The electron condition after a collision is sampled ac-
2041 cordingly. Therefore, more interactions are simulated in the microscopic tracking method,

2042 which is another contribution that makes it more accurate than the Monte Carlo integration
2043 method. The microscopic method was used to evaluate the MPFD.

2044 **7.5.5 Parallelization Scheme**

2045 A fission fragment deposits a few MeV energy in the gas volume of MPFD, which creates
2046 about 10^5 - 10^6 electron/ion pairs grouped into clusters. To track 1% of these electrons us-
2047 ing the time-consuming microscopic tracking method is beyond the capability of the serial
2048 Garfield++ code. Hence, an application parallelized by hybrid Message Passing Interface
2049 (MPI) and OpenMP was developed. The pseudo-code of the parallelization scheme is shown
2050 in Algorithm 1. Two thousand fission fragments were distributed among the computing
2051 nodes using MPI. On each node, the transport of the 1% ionized electrons was simulated
2052 by the cores using OpenMP. Each computing node was initialized with its own random seed
2053 automatically by the underlying ROOT program.

2054 In the code, after the MPI initialization, a set of `MediumMagboltz`, `ComponentElmer`,
2055 `Sensor`, and `TrackSrim` class objects is initialized. These utilities are owned by one core on
2056 the node and used to simulate the ionization of the fission fragments. The `MediumMagboltz`
2057 object defines the argon gas at 30 psig and 50 °C. The `ComponentElmer` object imports the
2058 field map computed by the Elmer program and assigns the defined `MediumMagboltz` object
2059 to fill the gas volume, i.e., `body 1` defined in `ElmerSolver`. In addition, the `ComponentElmer`
2060 objects enables the optimized element searching algorithm. The `MediumMagboltz` and the
2061 `ComponentElmer` objects define the material and geometry and complete the model descrip-
2062 tion. The `ComponentElmer` object is linked to a `Sensor` instance, which connects the model
2063 to the `TrackSrim` class instances. Two `TrackSrim` instances are initialized reading the SRIM
2064 energy loss tables of Sr and Xe, respectively.

2065 The `ncluster` and `nsignal` C++ vectors are used to store the computed cluster infor-
2066 mation and induced current by the assigned fission fragments on the node, respectively.

2067 Another set of thread-private class objects is initialized inside an OpenMP parallel con-
2068 struct to transport the electrons via the `AvalancheMicroscopic` class object. This set is

Algorithm 1 Pseudo-code of the Garfield++ parallelization scheme.

```
1: Initialize MPI
2: Initialize MediumMagboltz, ComponentElmer, Sensor, and TrackSrim class objects
3: Initialize ncluster, nsignal          ▷ vectors to store cluster and signal on the node
4: #pragma omp parallel
5: Initialize thread-private MediumMagboltz, ComponentElmer, Sensor, and
   AvalancheMicroscopic class objects
6: end omp parallel
7: for ff ← [0, 2000) do
8:   if ff % number of nodes == rank then          ▷ assign ff to MPI rank
9:     Initialize fcluster, fsignal          ▷ vectors to store ff cluster and signal
10:    Determine ff is Sr or Xe
11:    while true do          ▷ track ff to create electron clusters
12:      fcluster → clear
13:      Sample position and direction of ff
14:      TrackSrim → NewTrack(position, direction)
15:      fcluster ← (TrackSrim → GetCluster)
16:      if fcluster.size > 2 then
17:        break
18:      end if
19:    end while
20:    Adjust cluster time considering flight of fission fragment
21:    Initialize cmap          ▷ construct cluster map for 1% electrons
22:    #pragma omp parallel
23:    iSensor → ClearSignal          ▷ isensor: thread-private Sensor objects
24:    #pragma omp for
25:    for i ← [0, cmap.size) do
26:      AvalancheMicroscopic → AvalancheElectron(cmap[i])
27:    end for
28:    #pragma omp critical
29:    fsignal += isignal → GetSignal
30:    end omp critical
31:  end omp parallel
32:  Append fcluster to ncluster
33:  Append fsignal to nsignal
34: end if
35: end for
36: Print ncluster, nsignal×100
37: Finalize MPI
```

2069 static and exists until the simulation ends. Therefore, this utility set only needs to be initial-
2070 ized for once. Each core has the same utility set between two OpenMP parallel constructs,
2071 e.g., between the simulation of two successive fission fragments. The `AvalancheMicroscopic`

2072 object links to the **Sensor** object to reads the material and geometry. In addition, the calcu-
2073 lated induced current by the **AvalancheMicroscopic** object is also retrieved via the **Sensor**
2074 instance. The induced current between time zero and 1 μ s was calculated with a time bin
2075 of 0.01 ns.

2076 Simulation of the two thousand fission fragment histories is distributed among the MPI
2077 ranks, i.e., computing nodes. Half of the histories are $^{95}_{38}\text{Sr}$, and the other are $^{139}_{54}\text{Xe}$. Inside
2078 the loop, the **fcluster** and the **fsignal** C++ vectors are initialized to store the cluster
2079 information and induced current of this fission fragment. The fission fragment is sampled
2080 to be born uniformly in the fissile layer with an isotropic direction towards the gas volume.
2081 The **TrackSrim** object is used to track the fission fragment with the sampled position and
2082 direction. The process is repeated until the number of electron clusters created by the fission
2083 fragment is larger than two, as stated in Section 7.5.3. The sampled cluster information is
2084 stored in the **fcluster** vector. Then, the cluster time is adjusted according to the method
2085 presented in Section 7.5.3. A **cmap** C++ vector is initialized to store the cluster identification
2086 numbers of those 1% of electrons tracked.

2087 A team of cores on the node is formed in an OpenMP parallel construct to simulate the
2088 transport of electrons. The signal stored in the thread-private **Sensor** object is first cleared.
2089 Transport of the electrons is distributed to the cores using the OpenMP loop construct. The
2090 initial condition of the electron is read from the **cmap** vector using the cluster identification
2091 number, e.g., the *xyz* coordinates and the birth time. The electrons are assumed to begin
2092 with zero initial energy and random directions.

2093 The electrons are transported using the **AvalancheElectron** function defined in the
2094 **AvalancheMicroscopic** class. When the transport of the electrons is finished, the induced
2095 current in each core is accumulated to the **fsignal** vector in an OpenMP critical construct to
2096 compute the induced current of this fission fragment. Then, the **fcluster** and the **fsignal**
2097 vectors are appended to the **ncluster** and the **nsignal** vectors, respectively. When a node
2098 finishes the simulation of the assigned fission fragments, it prints out the cluster information
2099 and signal (re-factored by 100) of each fission fragment for post processing.

2100 To examine the correctness of the parallelization scheme, a particular MPFD calculation

2101 was performed using one core and 10 ten-core nodes. In this calculation, 500 fission fragments
2102 were simulated, half of which were Sr ions, while the remainder were Xe ions. The Monte
2103 Carlo integration method was used to track 0.5% of the electrons in each cluster. The
2104 diffusion process was not simulated.

2105 The computed induced currents of the two runs are shown in Fig. 7.7. The small difference
2106 may be explained by the facts that 1) the systematic error introduced by tracking only 0.5%
2107 electrons per cluster was not included; 2) the 500 fission fragments were born uniformly
2108 in the fissile layer and had isotropic directions, and 3) electron clusters were created with
2109 statistics. In the future work, a rigid comparison is warranted that the same set of random
2110 numbers was used by the serial and parallel runs to examine whether the two results are
2111 identical.

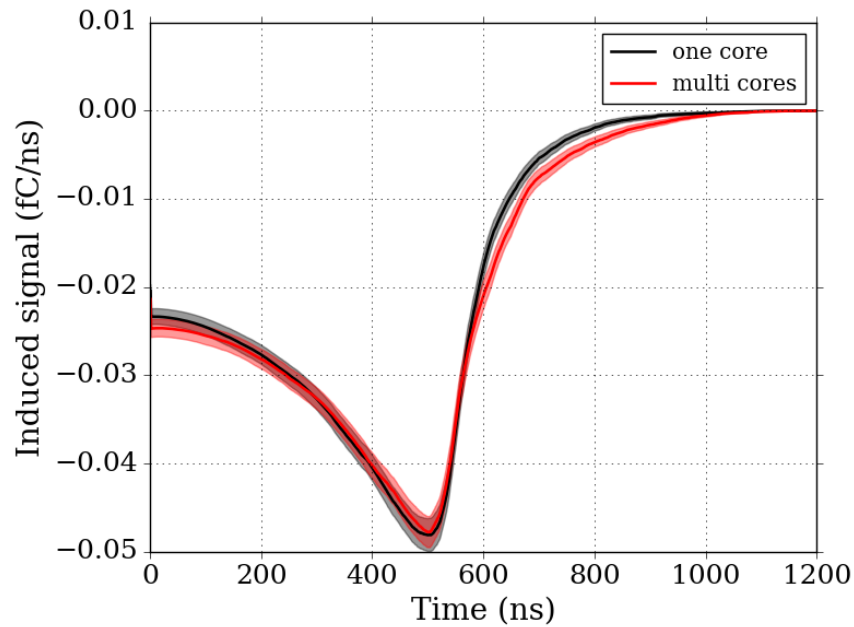


Figure 7.7: The computed induced current using one and 10×10 cores.

2112 7.6 MPFD Results

2113 Two thousand fission fragments were simulated using the microscopic tracking method.
2114 The averaged deposited energy per fission fragment to create electron clusters was $7.15 \pm$

2115 0.14 MeV. Along the path of a fission fragment, on average, 118.41 ± 2.34 electron clus-
 2116 ters were created. The average number of electrons created by a fission fragment was
 2117 $2.65 \times 10^5 \pm 5.12 \times 10^3$.

2118 Shown in Fig. 7.8 are the induced currents by three fission fragments, and shown in
 2119 Fig. 7.9 is the average induced current of the two thousand fission fragments. A peak exists
 2120 at about 0.3 ns, which may be due to the diffusion of the electrons born near the boundary.

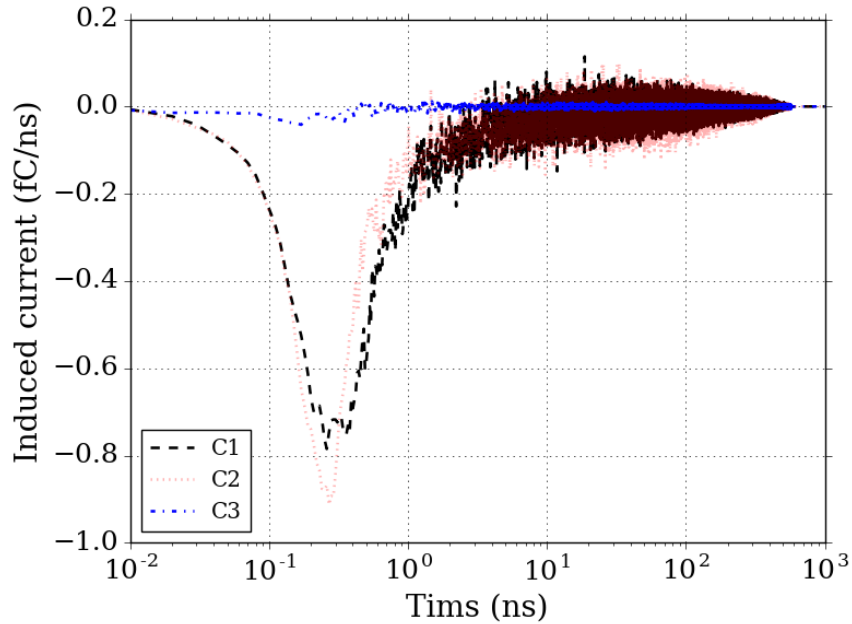


Figure 7.8: Induced currents by three fission fragments.

2121 For each fission fragment, the collected charge Q by the induced current i can be calcu-
 2122 lated by

$$Q = \int_0^{t_e} i(t)dt, \quad (7.3)$$

2123 where t_e is the end time of the integration. In practice, t_e represents an ideal RC circuit
 2124 setting in the experimental measurement to truncate the signal after the majority of the
 2125 electrons are collected. If t_e was set to the maximum of the tally window, i.e., $1 \mu s$, the
 2126 total charge can be computed. It is shown in Fig. 7.8 and Fig. 7.9 that $1 \mu s$ is sufficient
 2127 to collect the electrons in the MPFD. Then, the time necessary to collect 95% of the total
 2128 charge can be located. The total charge and the time to collect 95% of the total charge of

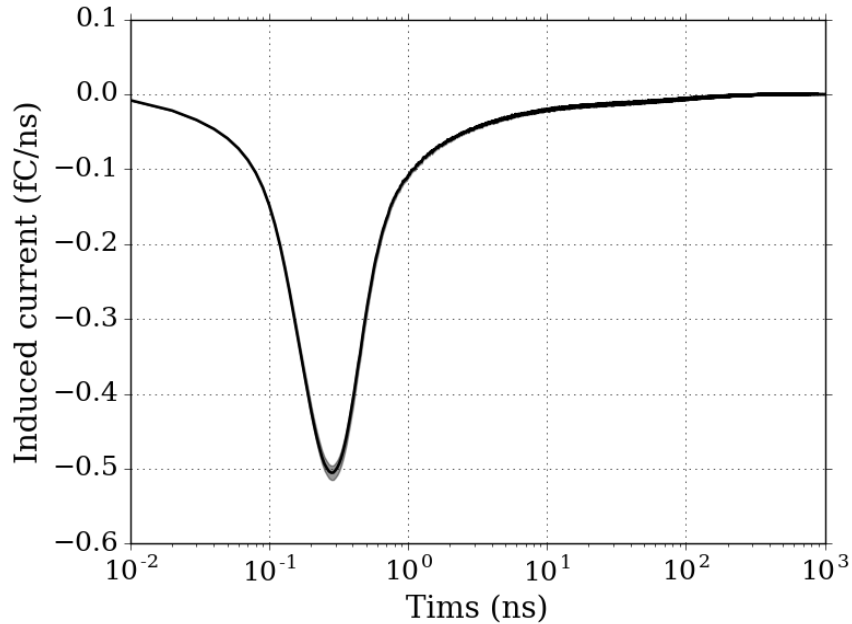


Figure 7.9: The averaged induced currents by two thousands fission fragments.

2129 the two thousand fission fragments are shown in Fig. 7.10. 57% of the fission fragments can
 2130 generate total charges larger than 2 fC, and 98.5% of the two thousand ionization events
 2131 need less than 400 ns to collect 95% of the total charge. The collected charges are in the fC
 2132 scale, and, hence, the signal from the MPFD needs to be amplified in the external circuit to
 2133 be measured.

2134 Shown in Fig. 7.11 is the distribution of the time to collect 95% of the total charge of the
 2135 two thousands fission fragments. The majority of the induced currents are within 400 ns.

2136 The distribution of the deposited energy by the fission fragments to create electron clus-
 2137 ters is shown in Fig. 7.12, and the distributions of the collected charges integrated to 400 ns
 2138 and 1 μ s are shown in Fig. 7.13. The shapes of the two charge distributions agree well, i.e.,
 2139 an integration time of 400 ns is sufficient to collect the majority of the electrons. The charge
 2140 distributions reveal the shape of the deposited energy distribution, because the electron re-
 2141 combination was not simulated. The integration time of 400 ns is sufficient to collect the
 2142 majority of the electrons.

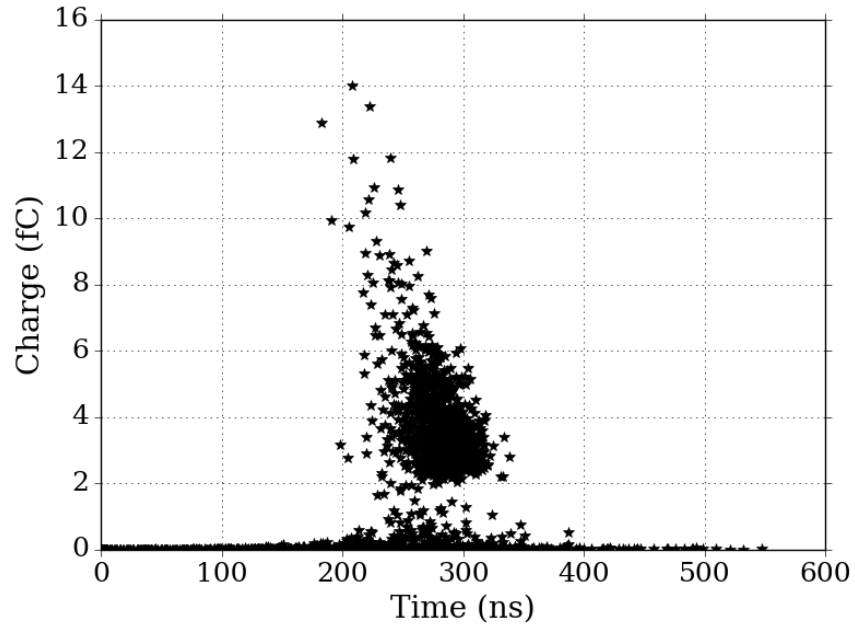


Figure 7.10: Correlated total charge and time to collect 95% of the charge.

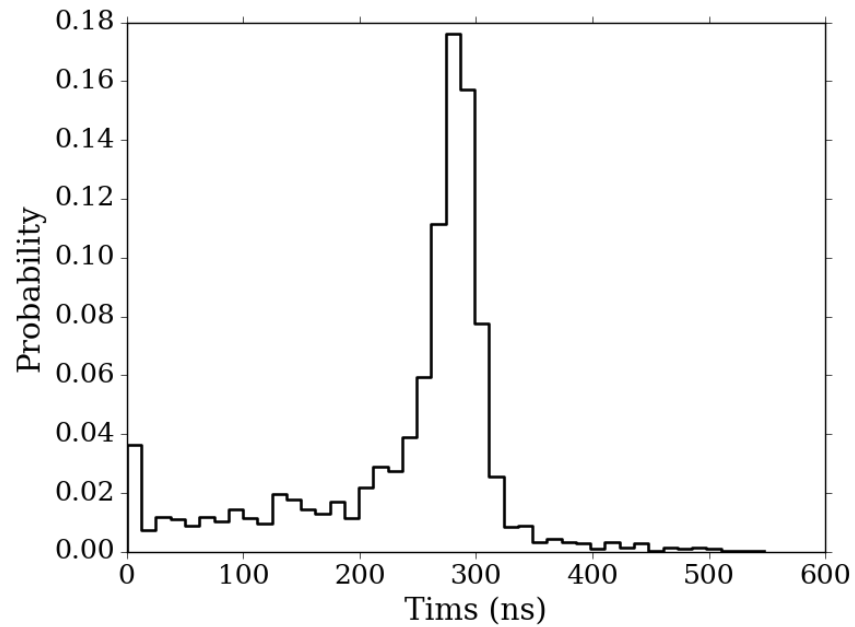


Figure 7.11: Distribution of the time to collect 95% of the total charge.

2143 **7.7 Summary**

2144 A computational tool to evaluate the electron collection process in MPFDs was developed.

2145 Gmsh and Elmer were used to calculate the electric field map in the gas volume of MPFD

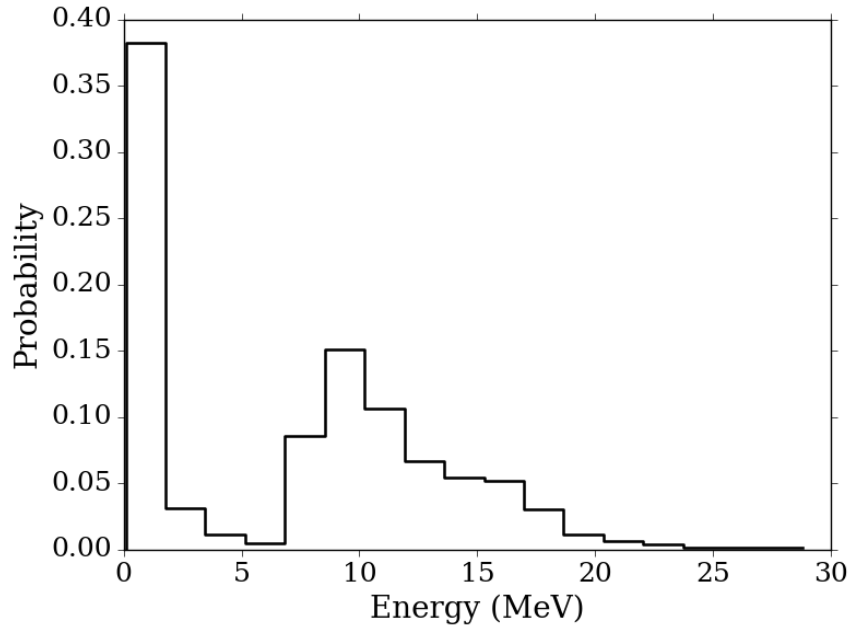


Figure 7.12: Distribution of the deposited energy to create electron clusters.

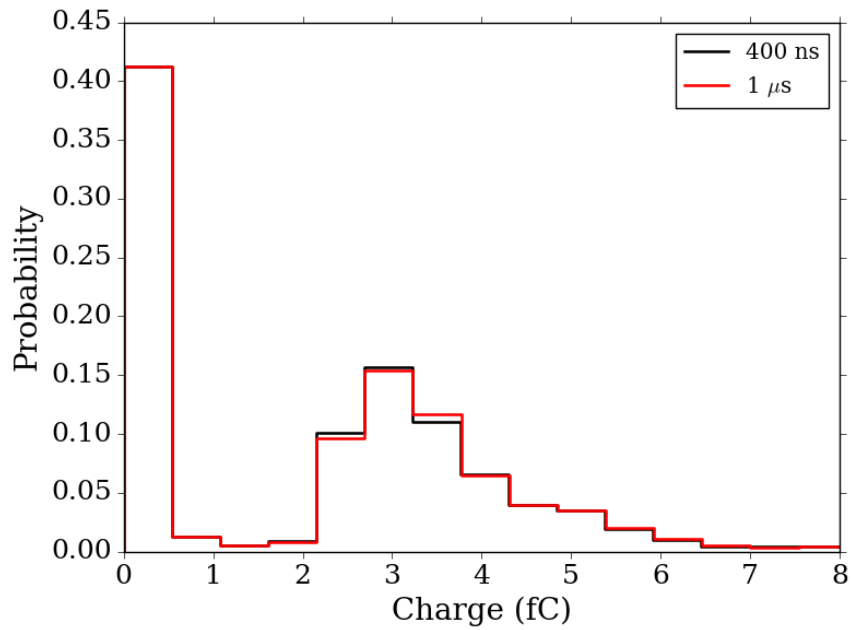


Figure 7.13: Distribution of the collected charge.

2146 using the finite-element method. The energy losses of the representative Sr and Xe fission
 2147 fragment pair were calculated by SRIM. With the Elmer and SRIM outputs, Garfield++ was
 2148 used to simulate the ionization of fission fragments, transportation of electrons, and compu-

2149 tation the induced current. In particular, the built-in optimized element search techniques
2150 and the developed parallelization scheme by hybrid MPI and OpenMP allowed simulation
2151 of 1% of the ionized electrons per cluster by the fission fragments using the most-accurate
2152 microscopic tracking method. According to the results, the fission fragments deposited an
2153 average of 7.15 MeV energy in the gas by ionizing electrons, which were collected within
2154 400 ns. The results suggest that the MPFD as designed can provide a fast response for
2155 in-core applications. Indeed, the results presented are preliminary, and the merit of this
2156 chapter is to explore a promising method to model the MPFD. As part of future work,
2157 the computational tool should be verified and validated to assist the development of the
2158 MPFD technology and to understand its response from the initial signal creation through
2159 the electronics system.

2160 Chapter 8

2161 Conclusion and Future Work

2162 8.1 Conclusions

2163 The restart of the TREAT facility brought back the transient test capability for nuclear fuels
2164 and materials to U.S.. After the restart, the facility will be first used to test the accident
2165 tolerant fuels used in contemporary nuclear reactor cores to improve safety. While the
2166 facility has been restarted, alternative neutron-detection techniques used in the hodoscope
2167 and in the TREAT core are under development at Kansas State University. In this work, the
2168 ZnS(Ag) scintillation detectors and fast-sensitive MSNDs for the hodoscope, and the MPFDs
2169 to measure in-core neutrons were evaluated using different computational tools to simulate
2170 the underlying physics. The calculations span the simulation of scintillation, semiconductor,
2171 and gas-filled detectors, which are the three common categories of neutron detectors.

2172 8.1.1 Hornyak Button

2173 The ZnS(Ag) scintillation detectors were modeled using Geant4 to simulate the coupled
2174 nuclear and optical physics. The Hornyak button fast-neutron detector used in the origi-
2175 nal TREAT hodoscope was first evaluated to validate the computational methodology and
2176 physics models. Under a hodoscope-like radiation environment, a neutron-detection effi-
2177 ciency of 0.35% was predicted at an S/N ratio of 100 consideration the scintillation noise

2178 generated by gamma rays. The efficiency agrees relatively well with the reported experimen-
2179 tal value of 0.4%, where the pulse-shape discrimination was applied. The strong gamma-
2180 induced Cherenkov noise was also observed in the simulation.

2181 **8.1.2 Hornyak Button Variants**

2182 To reduce the gamma-induced Cherenkov noise and to improve the neutron-detection effi-
2183 ciency, the layered and the homogenized Hornyak button variants were proposed. The new
2184 detectors use SiPMs to collect light, which is more efficient and reduces the Cherenkov noise
2185 generated in the combination of Lucite light guides and the PMT used in the Hornyak but-
2186 ton. The improved light-collection method allows a higher concentration of ZnS(Ag) in the
2187 scintillation volumes of the new detectors to increase the neutron-detection efficiency.

2188 Using the same methodology to evaluate the Hornyak button, it was predicted that
2189 the Cherenkov noises in the new detectors were reduced. To reject the gamma-induced
2190 scintillation and Cherenkov noises using the pulse-height discrimination, at the LLD settings
2191 that achieved an S/N ratio of 100, the optimized, 5-cm layered and homogenized detectors
2192 yielded neutron-detection efficiencies of 3.3% and 1.3%, respectively. By increasing the
2193 detector length along the mono-direction neutron path, the neutron-detection efficiencies
2194 were shown to saturate at about 5.9% and 2.2% for the layered and the homogenized devices,
2195 respectively. For more intense gamma-ray background (gamma-to-neutron ratios above 50),
2196 the homogenized detector exhibited better performance than the layered detector due to the
2197 less insensitivity of the homogenized scintillation volume to the incident gamma rays.

2198 **8.1.3 Fast-Sensitive MSNDs**

2199 The fast-sensitive MSNDs use fast-neutron converters to replace ${}^6\text{LiF}$ loaded in the well-
2200 established thermal-sensitive devices. The neutron converters considered were ${}^{237}\text{Np}$, ${}^{235}\text{U}$,
2201 natural uranium, and ${}^{232}\text{Th}$ for actinide MSNDs and paraffin wax for hydrogenous MSNDs.
2202 Paraffin wax has a larger fission-spectrum-weighted macroscopic cross section (0.32 cm^{-1})
2203 than the actinide materials (the best being 0.067 cm^{-1} for ${}^{237}\text{Np}$). However, the actinide

2204 reactants allow higher LLD settings due to the large energy of fission fragments.

2205 Using the fission fragment generator in Geant4 to evaluate the actinide MSNDs, at the
2206 5-MeV LLD setting, the intrinsic neutron-detection efficiency of the ^{235}U -filled MSND was
2207 1.2% for a 2-cm device length, and the efficiency saturated at 2.6% for lengths beyond 14 cm.
2208 The trench and wall widths in the ^{235}U -filled MSNDs were 20 and 10 μm , respectively, which
2209 is the current configuration of thermal-sensitive devices. For the 2-cm ^{235}U -filled MSND, the
2210 Geant4-computed, total deposited energy in the trenches differed from the MCNP6-predicted
2211 value by about 0.7%. The efficiencies of the ^{235}U -filled MSNDs acted as the lower limits of
2212 the ^{237}Np -loaded devices, which are preferred due to their insensitivity to the slow neutrons.
2213 The ^{237}Np -filled MSNDs were not evaluated in Geant4 due to the absence of neutron data
2214 library.

2215 Geant4 and MCNP6 were used to calculate the neutron event pulse height distributions
2216 of the hydrogenous MSNDs, and the results of the two codes agreed well. At 300-keV LLD
2217 setting, the intrinsic neutron-detection efficiencies of the hydrogenous MSNDs were 10% and
2218 26% at the device lengths of 2 and 20 cm, respectively, where the 20- μm trench and 10- μm
2219 wall widths were assumed.

2220 Geant4 was used to compute the pulse height distributions of the hydrogenous MSNDs
2221 irradiated by the hodoscope-like gamma rays. Based on the predicted gamma noises, at the
2222 LLD settings that achieve an S/N ratio of 100, the neutron-detection efficiencies were about
2223 2.5% and 9.6% for the hydrogenous MSNDs with device lengths of 2 and 20 cm, respectively,
2224 where the optimized 60- μm trench and 40- μm wall widths were applied.

2225 **8.1.4 MPFD**

2226 To evaluate the electron-collection process under applied electric field in MPFD, a compu-
2227 tational routine that consists of Gmsh, Elmer, SRIM, and Garfield++ was developed. The
2228 electric field in the MPFD gas volume was calculated by Gmsh and Elmer using a finite-
2229 element method. The energy loss tables of the representative Sr and Xe fission fragment pair
2230 were computed by SRIM. With the Elmer and SRIM results, Garfield++ was used to simu-

2231 late the ionization of fission fragments, transport of electrons in the argon gas, and calculate
2232 the induced current as a function of time. In particular, the built-in, optimized element
2233 search techniques and the developed hybrid MPI and OpenMP parallelization scheme were
2234 used to build the Garfield++ application, which allowed the simulation of 1% electrons ion-
2235 ized by 2000 fission fragments using the microscopic tracking algorithm. In the simulation,
2236 100-V voltage was applied to the anode, and the cathode was grounded. The temperature
2237 and pressure of the argon gas inside the MPFD were 50 °C and 30 psig, respectively. Under
2238 such condition, the averaged deposited energy to ionize electrons was about 7.15 MeV, and
2239 for the majority of the simulated neutron events, the induced current occurred within 400 ns.

2240 **8.2 Future Work**

2241 **8.2.1 Testing of the Hodoscope Detectors**

2242 While the modeling results of the hodoscope detectors are promising, they need to be tested
2243 to validate the computational results. Ideally, the detectors need to be tested in the ho-
2244 doscope which is not currently available. As a compromise, the piercing beam at the Kansas
2245 State University TRIGA Mark II reactor can be used to test the detectors. However, the
2246 beam is not fully characterized and known to be dominated by sub-fast neutrons and gamma
2247 rays. Ongoing efforts are to design appropriate filters used at the beam port to mimic the
2248 hodoscope radiation environment [86]. Upon completion of this characterization the con-
2249 struction of suitable filters, the beam can be a good facility to test the fast-neutron devices,
2250 and the detector performance under the characterized beam radiation can be calculated
2251 using the existing models.

2252 As a first demonstration, the prototypes of the layered Hornyak button variants were
2253 fabricated and irradiated using a ^{252}Cf source, and a neutron-detection efficiency of 9.2%
2254 was observed for a device length of 4 cm [87, 88].

2255 8.2.2 Expanding the MPFD Modeling

2256 Due to the time consideration, the MPFD modeling results are preliminary, and the method-
2257 ology can be considered *explored* and neither verified completely nor validated yet against
2258 experimental data. It is not convenient to navigate the underlying codes to make any changes
2259 because each code has its own syntax. Hence, a governing application should be developed
2260 that integrates the underlying codes and gives access to set the input parameters easily.

2261 A rigid verification of the parallelization scheme is necessary, where the same set of
2262 random numbers are used by the serial and parallel runs. The scaling performance of the
2263 parallelization scheme needs to be evaluated.

2264 The modeling results of MPFD were calculated using the most-accurate microscopic
2265 tracking method. In the future work, the Monte Carlo integration method needs to be
2266 explored, in which the simulation of the diffusion process can be turned off. This feature
2267 can be used to evaluate the effects of the diffusion process on the induced current.

2268 It is difficult to compare the calculated MPFD results against in-core measurements con-
2269 sidering the complexity of in-core radiation environment. Therefore, an out-of-core MPFD
2270 prototype might be necessary for the validation purpose.

Bibliography

2271

2272 [1] John D. Bess and Mark D. DeHart. Baseline assessment of TREAT for modeling and
2273 analysis needs. Technical report, Idaho National Laboratory (INL), 2015.

2274 [2] Theodore H. Bauer, Arthur E. Wright, William R. Robinson, John W. Holland, and
2275 Edgar A. Rhodes. Behavior of modern metallic fuel in TREAT transient overpower
2276 tests. *Nuclear Technology*, 92(3):325–352, 1990.

2277 [3] John D. Bess, Nicolas E. Woolstenhulme, Cliff B. Davis, Louis M. Dusanter, Charles P.
2278 Folsom, James R. Parry, Tate H. Shorthill, and Haihua Zhao. Narrowing transient
2279 testing pulse widths to enhance LWR RIA experiment design in the TREAT facility.
2280 *Annals of Nuclear Energy*, 124:548–571, 2019.

2281 [4] G. R. Imel and P. R. Hart. The performance of hafnium and gadolinium self powered
2282 neutron detectors in the TREAT reactor. *Nucl. Instr. Meth. Phys. Res. B*, 111(3-4):
2283 325–336, 1996.

2284 [5] John Bumgardner and Lee Nelson. Restart of the transient reactor test facility (TREAT)
2285 and resumption of transient testing. [https://docs.google.com/viewer?url=
2286 http%3A%2F%2Fwww.cab.cnea.gov.ar%2Ffigorr2014%2Fimages%2Fpresentations%
2287 2F18thNovTuesday%2FCondorRoom%2F1stBlock%2F01JohnBUMGARDNER.pdf](https://docs.google.com/viewer?url=http%3A%2F%2Fwww.cab.cnea.gov.ar%2Ffigorr2014%2Fimages%2Fpresentations%2F18thNovTuesday%2FCondorRoom%2F1stBlock%2F01JohnBUMGARDNER.pdf).

2288 [6] Jeremy A. Roberts, Mark J. Harrison, Wenkai Fu, Priyarshini Ghosh, and Douglas S.
2289 McGregor. Fast-neutron detector developments for the TREAT hodoscope. *Radiation
2290 Physics and Chemistry*, 155:184–190, 2019.

2291 [7] Nicholas Tsoulfanidis and Sheldon Landsberger. *Measurement and detection of radia-
2292 tion*. CRC Press, Third edition, 2011.

- 2293 [8] Douglas S. McGregor. Materials for gamma-ray spectrometers: inorganic scintillators.
2294 *Annual Review of Materials Research*, 48:245–277, 2018.
- 2295 [9] B. Dolgoshein, V. Balagura, P. Buzhan, M. Danilov, L. Filatov, E. Garutti, M. Groll,
2296 A. Ilyin, V. Kantserov, V. Kaplin, et al. Status report on silicon photomultiplier devel-
2297 opment and its applications. *Nucl. Instr. Meth. Phys. Res. A*, 563(2):368–376, 2006.
- 2298 [10] Douglas S. McGregor and J. Kenneth Shultis. *Radiation detection and measurement:
2299 concepts, methods and devices*. In press.
- 2300 [11] A. De Volpi, R. J. Pecina, R. T. Daly, D. J. Travis, R. R. Stewart, and E. A. Rhodes.
2301 Fast-neutron hodoscope at TREAT: development and operation. *Nuclear Technology*,
2302 27(3):449–487, 1975.
- 2303 [12] M. B. Chadwick, M. Herman, P. Obložinský, Michael E. Dunn, Y. Danon, A. C. Kahler,
2304 Donald L. Smith, B. Pritychenko, Goran Arbanas, R. Arcilla, et al. ENDF/B-VII.1
2305 nuclear data for science and technology: cross sections, covariances, fission product
2306 yields and decay data. *Nuclear Data Sheets*, 112(12):2887–2996, 2011.
- 2307 [13] D. Devin Imholte and Fatih Aydogan. Comparison of nuclear pulse reactor facilities
2308 with reactivity-initiated-accident testing capability. *Progress in Nuclear Energy*, 91:
2309 310–324, 2016.
- 2310 [14] Clint Baker. TREAT sodium loop: status update. [https://docs.google.com/
2311 viewer?url=http%3A%2F%2Fresearch.egr.oregonstate.edu%2Ftreat-irp%
2312 2Fsites%2Fresearch.egr.oregonstate.edu.treat-irp%2Ffiles%2F14._desired_
2313 stakeholder_outcomes_task_2_baker.pdf](https://docs.google.com/viewer?url=http%3A%2F%2Fresearch.egr.oregonstate.edu%2Ftreat-irp%2Fsites%2Fresearch.egr.oregonstate.edu.treat-irp%2Ffiles%2F14._desired_stakeholder_outcomes_task_2_baker.pdf), October 2015.
- 2314 [15] Sedat Goluoglu and Mark D. DeHart. On the effects of pre-and post-transient rod posi-
2315 tions for treat temperature-limited transient powers. *Nuclear Engineering and Design*,
2316 331:97–102, 2018.
- 2317 [16] Live chart of nuclides, nuclear structure and decay data. [https://www-nds.iaea.org/
2318 relnsd/vcharthtml/VChartHTML.html](https://www-nds.iaea.org/relnsd/vcharthtml/VChartHTML.html).

- 2319 [17] Office of Nuclear Energy. Resumption of transient testing. <https://www.energy.gov/ne/articles/resumption-transient-testing>, April 2013. U.S. Department of
2320 Energy.
2321
- 2322 [18] Steven J. Zinkle, Kurt A. Terrani, Jess C. Gehin, Larry J. Ott, and Lance Lewis Snead.
2323 Accident tolerant fuels for LWRs: A perspective. *Journal of Nuclear Materials*, 448
2324 (1-3):374–379, 2014.
- 2325 [19] Idaho Operations Office. Environmental assessment for the resumption of transient
2326 testing of nuclear fuels and materials. Technical report, U.S. Department of Energy,
2327 February 2014.
- 2328 [20] G. A. Freund, H. P. Iskenderian, and D. Okrent. TREAT, a pulsed graphite-moderated
2329 reactor for kinetic experiments. In *Proc. 2nd United Nations Int. Conf. on the Peaceful
2330 Uses of Atomic Energy*, volume 10, pages 461–475, Geneva, Switzerland, 1958.
- 2331 [21] R. G. Sachs. Reactor safety audit report of ANL-W reactor. Technical Report ANL-
2332 NN-128, Argonne National Laboratory, June 1974.
- 2333 [22] C. J. Parga, I. J. van Rooyen, and E. P. Luther. Fuel-clad chemical interaction evaluation
2334 of the TREAT reactor conceptual low-enriched-uranium fuel element. *Journal of Nuclear
2335 Materials*, 2018.
- 2336 [23] J. Kenneth Shultis and Richard E. Faw. *Fundamentals of Nuclear Science and Engi-
2337 neering*. CRC press, Third edition, 2016.
- 2338 [24] H. D. Warren and N. H. Shah. Neutron and gamma-ray effects on self-powered in-core
2339 radiation detectors. *Nuclear Science and Engineering*, 54(4):395–415, 1974.
- 2340 [25] M. A. Lampert and P. Mark. *Current injection in solids*. Academic Press, New York
2341 City, 1970. page 40.
- 2342 [26] D. C. Wade, S. K. Bhattacharyya, W. C. Lipinski, and C. C. Stone. Core design of the
2343 upgraded treat reactor. Technical report, Argonne National Lab., 1982.

- 2344 [27] Thermal neutron capture γ 's (CapGam). [https://www-nds.iaea.org/capgam/byn/](https://www-nds.iaea.org/capgam/byn/page058.html)
2345 [page058.html](https://www-nds.iaea.org/capgam/byn/page058.html).
- 2346 [28] G. R. Keepin. Neutron scintillation counting by the $S(n, p)P^{32}$ process in ZnS(Ag)
2347 phosphors. *Review of Scientific Instruments*, 25(1):30–32, 1954.
- 2348 [29] A. De Volpi and K. G. Porges. Rejection of gamma background radiation pulses in
2349 Hornyak buttons. *IRE Transactions on Nuclear Science*, 9(3):320–326, 1962.
- 2350 [30] K. G. Porges, A. De Volpi, and P. Polinski. Fast cancellation of gamma radiation
2351 background pulses in Hornyak buttons with an active circuit. *Review of Scientific*
2352 *Instruments*, 35(11):1602–1604, 1964.
- 2353 [31] Robley D. Evans. *The atomic nucleus*. McGraw-Hill Book Company, 1955.
- 2354 [32] S. Agostinelli, J. Allison, K. Amako, et al. GEANT4-a simulation toolkit. *Nucl. Instr.*
2355 *Meth. Phys. Res. A*, 506(3):250–303, 2003.
- 2356 [33] T. Goorley, M. James, T. Booth, F. Brown, J. Bull, L. J. Cox, J. Durkee, J. Elson,
2357 M. Fensin, R. A. Forster, et al. Initial MCNP6 release overview. *Nuclear Technology*,
2358 180(3):298–315, 2012.
- 2359 [34] J. Allison, K. Amako, J. Apostolakis, P. Arce, M. Asai, T. Aso, E. Bagli, A. Bagulya,
2360 S. Banerjee, G. Barrand, et al. Recent developments in Geant4. *Nucl. Instr. Meth.*
2361 *Phys. Res. A*, 835:186–225, 2016.
- 2362 [35] D. Pelowitz, J. Goorley, M. Fensin, et al. *MCNP6 User's Manual*, May 2013. Version
2363 1.0.
- 2364 [36] Garfield++, simulation of tracking detectors. [http://garfieldpp.web.cern.ch/](http://garfieldpp.web.cern.ch/garfieldpp/)
2365 [garfieldpp/](http://garfieldpp.web.cern.ch/garfieldpp/).
- 2366 [37] Christophe Geuzaine and Jean-François Remacle. Gmsh: A 3-D finite element mesh
2367 generator with built-in pre-and post-processing facilities. *International journal for nu-*
2368 *merical methods in engineering*, 79(11):1309–1331, 2009.

- 2369 [38] Elmer, open source multiphysical simulation software. [https://www.csc.fi/web/](https://www.csc.fi/web/elmer/elmer)
2370 [elmer/elmer](https://www.csc.fi/web/elmer/elmer).
- 2371 [39] James F. Ziegler, Matthias D. Ziegler, and Jochen P. Biersack. SRIM—the stopping and
2372 range of ions in matter (2010). *Nucl. Instr. Meth. Phys. Res. B*, 268(11-12):1818–1823,
2373 2010.
- 2374 [40] Richard T. Kouzes, Azaree T. Lintereur, and Edward R. Siciliano. Progress in alterna-
2375 tive neutron detection to address the helium-3 shortage. *Nucl. Instr. Meth. Phys. Res.*
2376 *A*, 784:172–175, 2015.
- 2377 [41] Steven L. Bellinger, Ryan G. Fronk, Timothy J. Sobering, and Douglas S. McGregor.
2378 High-efficiency microstructured semiconductor neutron detectors that are arrayed, dual-
2379 integrated, and stacked. *Applied Radiation and Isotopes*, 70(7):1121–1124, 2012.
- 2380 [42] T. R. Ochs, S. L. Bellinger, R. G. Fronk, L. C. Henson, R. M. Hutchins, and D. S.
2381 McGregor. Improved manufacturing and performance of the dual-sided microstructured
2382 semiconductor neutron detector (DS-MSND). *Nucl. Instr. Meth. Phys. Res. A*. <https://doi.org/10.1016/j.nima.2018.12.011>.
2383
- 2384 [43] Priyarshini Ghosh, Wenkai Fu, Ryan Fronk, Douglas S. McGregor, and Jeremy A.
2385 Roberts. Evaluation of MSNDs for fast-neutron detection and the TREAT hodoscope.
2386 In *Transactions of the American Nuclear Society*, volume 115, pages 1009–1012, 2016.
- 2387 [44] B. M. van der Ende, E. T. Rand, A. Erlandson, and L. Li. Use of SRIM and Garfield
2388 with Geant4 for the characterization of a hybrid $^{10}\text{B}/^3\text{He}$ neutron detector. *Nucl. Instr.*
2389 *Meth. Phys. Res. A*, 894:138–144, 2018.
- 2390 [45] S. F. Biagi. Monte carlo simulation of electron drift and diffusion in counting gases
2391 under the influence of electric and magnetic fields. *Nucl. Instr. Meth. Phys. Res. A*,
2392 421:234–240, 1999.
- 2393 [46] Vishal K. Patel, Michael A. Reichenberger, Jeremy A. Roberts, Troy C. Unruh, and
2394 Douglas S. McGregor. MCNP6 simulated performance of Micro-Pocket Fission Detec-

- 2395 tors (MPFDs) in the Transient REActor Test (TREAT) facility. *Annals of Nuclear*
2396 *Energy*, 104:191–196, 2017.
- 2397 [47] Xiaodong Zhang, Jason P. Hayward, and Mitchell A. Laubach. New method to remove
2398 the electronic noise for absolutely calibrating low gain photomultiplier tubes with a
2399 higher precision. *Nucl. Instr. Meth. Phys. Res. A*, 755:32–37, 2014.
- 2400 [48] R. Mirzoyan, Mustapha Laatiaoui, and M. Teshima. Very high quantum efficiency
2401 PMTs with bialkali photo-cathode. *Nucl. Instr. Meth. Phys. Res. A*, 567(1):230–232,
2402 2006.
- 2403 [49] G. Bondarenko, P. Buzhan, B. Dolgoshein, et al. Limited geiger-mode microcell silicon
2404 photodiode: new results. *Nucl. Instr. Meth. Phys. Res. A*, 442:187–192, 2000.
- 2405 [50] Claudio Piemonte and Alberto Gola. Overview on the main parameters and technology
2406 of modern Silicon Photomultipliers. *Nucl. Instr. Meth. Phys. Res. A*, 2018. <https://doi.org/10.1016/j.nima.2018.11.119>.
2407
- 2408 [51] D. S. McGregor, S. L. Bellinger, R. G. Fronk, L. Henson, D. Huddleston, T. Ochs,
2409 J. K. Shultis, T. J. Sobering, and R. D. Taylor. Development of compact high efficiency
2410 microstructured semiconductor neutron detectors. *Radiation Physics and Chemistry*,
2411 116:32–37, 2015.
- 2412 [52] Introduction to Geant4. [http://geant4-userdoc.web.cern.ch/geant4-userdoc/](http://geant4-userdoc.web.cern.ch/geant4-userdoc/Welcome/IntroductionToGeant4/html/introductionToGeant4.html)
2413 [Welcome/IntroductionToGeant4/html/introductionToGeant4.html](http://geant4-userdoc.web.cern.ch/geant4-userdoc/Welcome/IntroductionToGeant4/html/introductionToGeant4.html), .
- 2414 [53] K. Hartling, B. Ciungu, G. Li, G. Bentoumi, and B. Sur. The effects of nuclear data
2415 library processing on Geant4 and MCNP simulations of the thermal neutron scattering
2416 law. *Nucl. Instr. Meth. Phys. Res. A*, 891:25–31, 2018.
- 2417 [54] B. M. van der Ende, J. Atanackovic, A. Erlandson, and G. Bentoumi. Use of GEANT4
2418 vs. MCNPX for the characterization of a boron-lined neutron detector. *Nucl. Instr.*
2419 *Meth. Phys. Res. A*, 820:40–47, 2016.

- 2420 [55] Geant4 reference physics lists. [http://geant4-userdoc.web.cern.ch/
2421 geant4-userdoc/UsersGuides/PhysicsListGuide/html/reference_PL/index.
2422 html](http://geant4-userdoc.web.cern.ch/geant4-userdoc/UsersGuides/PhysicsListGuide/html/reference_PL/index.html), .
- 2423 [56] CERN writing guidelines. [https://writing-guidelines.web.cern.ch/tags/
2424 spelling](https://writing-guidelines.web.cern.ch/tags/spelling).
- 2425 [57] Jenny Nilsson, Vesna Cuplov, and Mats Isaksson. Identifying key surface parameters
2426 for optical photon transport in GEANT4/GATE simulations. *Applied Radiation and
2427 Isotopes*, 103:15–24, 2015.
- 2428 [58] A. Levin and C. Moisan. A more physical approach to model the surface treatment
2429 of scintillation counters and its implementation into DETECT. In *1996 IEEE Nuclear
2430 Science Symposium. Conference Record*, volume 2, pages 702–706. IEEE, 1996.
- 2431 [59] *Geant4 User's guide for application developers*. Geant4 collaboration, Geant4 10.2 edi-
2432 tion, December 2015.
- 2433 [60] *Geant4 user's guide for application developers*. Geant4 collaboration, Geant4 10.3 edi-
2434 tion, December 2016.
- 2435 [61] W. F. Hornyak. A fast neutron detector. *Review of Scientific Instruments*, 23(6):
2436 264–267, 1952.
- 2437 [62] X-5 Monte Carlo team. *MCNP - A general Monte Carlo n-particle transport code*, 5
2438 edition, 2003.
- 2439 [63] Jerome M. Verbeke, Chris Hagmann, and Doug Wright. Simulation of neutron and
2440 gamma ray emission from fission and photofission. *Lawrence Livermore National Labo-
2441 ratory, Livermore CA, UCRL-AR-228518*, 3:25–35, 2010.
- 2442 [64] C. L. Fink. Optimization of a hornyak-button detector for fast-neutron detection. *IEEE
2443 Transactions on Nuclear Science*, 29(1):718–721, 1982.

- 2444 [65] PMMA refractive index. [http://refractiveindex.info/?shelf=organic&book=](http://refractiveindex.info/?shelf=organic&book=poly(methyl_methacrylate)&page=Szczurowski)
2445 [poly\(methyl_methacrylate\)&page=Szczurowski](http://refractiveindex.info/?shelf=organic&book=poly(methyl_methacrylate)&page=Szczurowski).
- 2446 [66] ZnS(Ag) scintillation material. [www.hep.ph.ic.ac.uk/fets/pepperpot/docs+](http://www.hep.ph.ic.ac.uk/fets/pepperpot/docs+papers/zns_602.pdf)
2447 [papers/zns_602.pdf](http://www.hep.ph.ic.ac.uk/fets/pepperpot/docs+papers/zns_602.pdf), 2002.
- 2448 [67] Saint-Gobain Crystals scintillation products. [http://www-eng.lbl.gov/~shuman/](http://www-eng.lbl.gov/~shuman/NEXT/MATERIALS&COMPONENTS/WLS_materials/Organics-Brochure.pdf)
2449 [NEXT/MATERIALS&COMPONENTS/WLS_materials/Organics-Brochure.pdf](http://www-eng.lbl.gov/~shuman/NEXT/MATERIALS&COMPONENTS/WLS_materials/Organics-Brochure.pdf), .
- 2450 [68] BC702 data sheet. [http://www.crystals.saint-gobain.com/sites/imdf.](http://www.crystals.saint-gobain.com/sites/imdf.crystals.com/files/documents/sgc-bc702-data-sheet_70148.pdf)
2451 [crystals.com/files/documents/sgc-bc702-data-sheet_70148.pdf](http://www.crystals.saint-gobain.com/sites/imdf.crystals.com/files/documents/sgc-bc702-data-sheet_70148.pdf), .
- 2452 [69] Heather J. MacLean Chichester. Advanced fuels campaign in-reactor instrumen-
2453 tation overview. [https://www.energy.gov/sites/prod/files/2015/11/f27/7.](https://www.energy.gov/sites/prod/files/2015/11/f27/7.%20Advanced%20Fuels%20Program%20In-Reactor%20Instrumentation%20Overview.pdf)
2454 [%20Advanced%20Fuels%20Program%20In-Reactor%20Instrumentation%20Overview.](https://www.energy.gov/sites/prod/files/2015/11/f27/7.%20Advanced%20Fuels%20Program%20In-Reactor%20Instrumentation%20Overview.pdf)
2455 [pdf](https://www.energy.gov/sites/prod/files/2015/11/f27/7.%20Advanced%20Fuels%20Program%20In-Reactor%20Instrumentation%20Overview.pdf), Oct. 28, 2015.
- 2456 [70] Ryan G. Fronk, Steven L. Bellinger, Luke C. Henson, et al. Advancements on dual-
2457 sided microstructured semiconductor neutron detectors (DSMSNDs). In *Proc. IEEE*
2458 *Nucl. Sci. Symp. Med. Imag. Conf. (NSS/MIC)*, pages 1–4, 2015.
- 2459 [71] Ryan G. Fronk, Steven L. Bellinger, Luke C. Henson, Taylor R. Ochs, Colten T. Smith,
2460 J. Kenneth Shultis, and Douglas S. McGregor. Dual-sided microstructured semicon-
2461 ductor neutron detectors (DSMSNDs). *Nucl. Instr. Meth. Phys. Res. A*, 804:201–206,
2462 2015.
- 2463 [72] Ronald J. McConn, Christopher J. Gesh, Richard T. Pagh, Robert A. Rucker, and
2464 Robert Williams III. Compendium of material composition data for radiation transport
2465 modeling. Technical report, Pacific Northwest National Laboratory (PNNL), Richland,
2466 WA (US), 2011.
- 2467 [73] T. Koi, D. H. Wright, and L. Desorgher. Simulation of the production
2468 of radionuclides using Geant4. <https://public.ornl.gov/neutrons/conf/>

- 2469 [aria2015/presentations/04%20Simulation%20of%20the%20Production%20of%20Radionuclides%20Using%20Geant4.pdf](#).
- 2470
- 2471 [74] M. B. Chadwick, P. Obložinský, M. Herman, N. M. Greene, R. D. McKnight, D. L.
2472 Smith, P. G. Young, R. E. MacFarlane, G. M. Hale, S. C. Frankle, et al. ENDF/B-
2473 VII.0: next generation evaluated nuclear data library for nuclear science and technology.
2474 *Nuclear data sheets*, 107(12):2931–3060, 2006.
- 2475 [75] Taylor R. Ochs, Steven L. Bellinger, Ryan G. Fronk, Luke C. Henson, David E. Huddle-
2476 ston, Zoairia I. Lyric, J. Kenneth Shultis, Colten T. Smith, Timothy J. Sobering, and
2477 Douglas S. McGregor. Present status of the microstructured semiconductor neutron
2478 detector (MSND)-based direct helium-3 replacement. *IEEE Transactions on Nuclear*
2479 *Science*, 2017.
- 2480 [76] Josh Renner. Detector simulation in Garfield++ with open-source finite el-
2481 ement electrostatics. [https://garfieldpp.web.cern.ch/garfieldpp/examples/
2482 elmer/garfield_elmer_doc.pdf](https://garfieldpp.web.cern.ch/garfieldpp/examples/elmer/garfield_elmer_doc.pdf).
- 2483 [77] Fast light toolkit (FLTK). <http://www.fltk.org/index.php>.
- 2484 [78] Open Cascade Technology. <https://www.opencascade.com/>.
- 2485 [79] Christophe Geuzaine and Jean-François Remacle. *Gmsh reference manual*, Gmsh 3.0
2486 edition, November 2017.
- 2487 [80] G. W. Fraser and E. Mathieson. Monte Carlo calculation of electron transport coeffi-
2488 cients in counting gas mixtures: I. argon-methane mixtures. *Nucl. Instr. Meth. Phys.*
2489 *Res. A*, 247(3):544–565, 1986.
- 2490 [81] O. Bouhali, A. Sheharyar, and T. Mohamed. Accelerating avalanche simulation in gas
2491 based charged particle detectors. *Nucl. Instr. Meth. Phys. Res. A*, 901:92–98, 2018.
- 2492 [82] H. Schindler. *Garfield++ user guide*, 2017.2 edition, February 2017.

- 2493 [83] I. B. Smirnov. Modeling of ionization produced by fast charged particles in gases. *Nucl.*
2494 *Instr. Meth. Phys. Res. A*, 554(1-3):474–493, 2005.
- 2495 [84] National nuclear data center. <https://www.nndc.bnl.gov/>.
- 2496 [85] P. Filliatre, C. Jammes, B. Geslot, and R. Veenhof. A monte carlo simulation of the
2497 fission chambers neutron-induced pulse shape using the Garfield suite. *Nucl. Instr.*
2498 *Meth. Phys. Res. A*, 678:139–147, 2012.
- 2499 [86] John C. Boyington, Richard L. Reed, Ryan M. Ullrich, and Jeremy A. Roberts. Gamma-
2500 ray and thermal-neutron filter design for a TRIGA penetrating beam port. *Transactions*
2501 *of the American Nuclear Society*, 117:1162–1165, 2017.
- 2502 [87] Priyarshini Ghosh, Wenkai Fu, Patrick K. Doyle, Nathaniel S. Edwards, Mark J. Har-
2503 rison, Jeremy A. Roberts, and Douglas S. McGregor. A high-efficiency, low-Cherenkov
2504 micro-layered fast neutron detector for the TREAT hodoscope. *Nucl. Instr. Meth. Phys.*
2505 *Res. A*, 904:100–106, 2018.
- 2506 [88] Priyarshini Ghosh, Wenkai Fu, Mark J. Harrison, Patrick K. Doyle, Jeremy A. Roberts,
2507 and Douglas S. McGregor. Factors affecting performance of the micro-layered fast-
2508 neutron detector. *Nucl. Instr. Meth. Phys. Res. A*. [https://doi.org/10.1016/j.](https://doi.org/10.1016/j.nima.2018.12.040)
2509 [nima.2018.12.040](https://doi.org/10.1016/j.nima.2018.12.040).

2510 Appendix A

2511 MCNP and Geant4 Inputs

2512 An example problem was modeled in MCNP and Geant4 to compare the inputs. The details
2513 of the problem are shown in Fig. A.1. The global volume is a cube with 20-cm length filled
2514 with dry air. At the center of the global volume is a cubic tank filled with paraffin wax. The
2515 tank has 10-cm length and spans from -5 to 5 cm in the xyz axes. A point source is located
2516 at $(-6, 0, 0)$ cm, i.e., 1-cm away from the tank, and shoots neutrons with 1-MeV energy into
2517 the tank along the x axis. The tally is the total deposited energy in the tank. The problem
2518 was modeled in Geant4 10.3.1 and MCNP6.1.

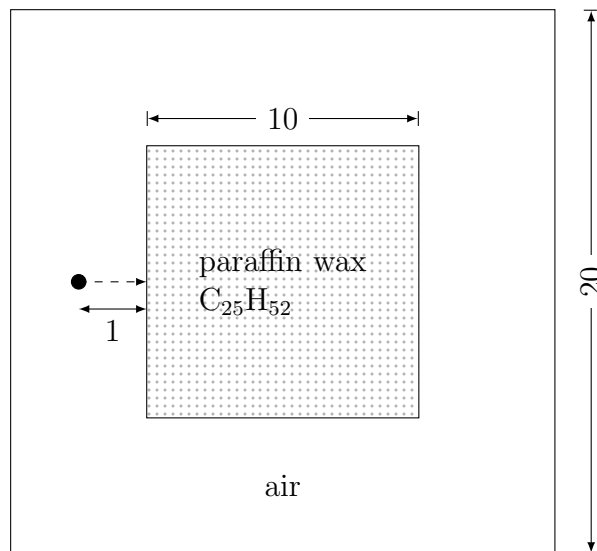


Figure A.1: An example problem was modeled in Geant4 and MCNP to compare the inputs. All dimensions are in cm.

2519 **A.1 MCNP Input**

2520 The MCNP input is shown in Fig. A.2, which consists of cell, surface, and several data cards.

2521 **A.1.1 Surface Cards**

2522 In the surface cards, surface 1 is a rectangular parallelepiped macrobody (with keyword
2523 `rpp`), which spans from -10 to 10 cm in the xyz axes. Surface 1 is used to describe the global
2524 volume. Surface 2 is defined in the same way as surface 1, and surface 2 is used to model
2525 the tank filled with paraffin wax.

2526 **A.1.2 Cell Cards**

2527 A cell card consists of the cell number, filled material, and bounding surfaces to describe the
2528 volume. Specially, cell 1 is void (indicated by 0) and defines the volume outside surface 1.
2529 The volume outside a macrobody is positive with respect to the surface number. Cell 2 is
2530 filled with material 1 (dry air) with density of 0.001205 g/cm^3 . The negative density value
2531 indicates the unit of g/cm^3 . The cell is inside surface 1 and outside surface 2. Cell 3 is filled
2532 with material 2 (paraffin wax) with density of 0.93 g/cm^3 , and it is inside surface 2.

2533 **A.1.3 Data Cards**

2534 **Material Cards**

2535 A material card consists of material number, nuclide identifiers and corresponding fractions.
2536 A nuclide identifier is formed by the ZA number and the data table identification number.
2537 The fraction can be specified by mass fraction using negative value or by atom fraction as
2538 positive.

2539 Material 1 defines the dry air and consists of natural abundance carbon (6000), ^{14}N
2540 (7014), ^{16}O (8016), and natural abundance argon (18000), and the mass fraction of these
2541 nuclides are specified. In the data table identification number, 70 represents the Endf70a
2542 library at 293.6 K, and `c` stands for continuous-energy neutron tables. The Endf70a library

```

A simple MCNP example
c cell card
1 0          1    $ outside world
2 1 -0.001205 -1 2 $ air surrounding tank
3 2 -0.93     -2   $ in tank

c surface card
1 rpp -10 10 -10 10 -10 10 $ world
2 rpp  -5 5 -5 5 -5 5      $ tank

c data card
c material cards
c dry air, rho = 0.001205
m1 6000.70c  -0.000124 &
    7014.70c  -0.755268 &
    8016.70c  -0.231781 &
    18000.59c -0.012827
c paraffin wax, C25H52, density = 0.93 g/cm3
m2 1001.70c  52 &
    6000.70c  25

c importance cards
imp:n 0 1 1
imp:h 0 1 1
imp:p 0 1 1
imp:# 0 1 1
imp:e 0 1 1
c mode card
mode p h # n e
c cut off card
cut:h j 0 $ default = 1 MeV
cut:# j 0 $ default = 5 MeV
c neutron physics
phys:n 6j 4
c tally card
+f6 3
sd6 1
c source card
sdef par=n erg=1 x=-6 y=0 z=0 vec=1 0 0 dir=1
nps 1000
print 110

```

Figure A.2: MCNP input of the simple model.

2543 for natural abundance argon (18000) is not available, and, thus, the Misc5xs library (with
2544 identification number 59) at 293.6 K is used. The available data libraries are listed at
2545 Appendix G, Volume I of the MCNP5 manual [62]. Material 2 defines the paraffin wax
2546 ($C_{25}H_{52}$) using atom fractions.

2547 **Importance and Mode Cards**

2548 In the mode card, neutron (n), proton (h), photon (p), ion (#), and electron (e) are tracked
2549 for best accuracy. The importances for these particles in cell 1 to 3 are zero, one, and one,
2550 respectively.

2551 **Cutoff Cards**

2552 The default low kinetic-energy cutoffs for proton and ion are 1 and 5 MeV, respectively,
2553 which are too high for this problem. Hence, the cutoffs are lowered to zero for best accuracy.
2554 In practice, MCNP6 adjusts these zero cutoffs to the minimum value of 1 keV. The default
2555 cutoffs for neutron (0), photon (1 keV), and electron (1 keV) are used and not specified.

2556 **Neutron Physics Card**

2557 The first 6 input parameters in the neutron physics card are skips by the 6j shortcut. The
2558 7th parameter, `coilf`, is set to 4, which generates one ion from neutron elastic scattering
2559 and uses the neutron capture ion algorithm (NCIA) to sample the capture reaction with ^3He ,
2560 ^6Li and ^{10}B (though these nuclides are not present in this problem). The NCIA preserves
2561 the correlation of the secondary particles, e.g., ^3H and ^4He in the ^6Li reaction. This `coilf`
2562 value is recommended in the MCNP6 manual [35].

2563 **Tally Cards**

2564 The `+f6` collision heating tally is used to compute the deposited energy in cell 3. In default,
2565 this tally applies to all tracked particles, and, thus, no particle designator is needed. The
2566 unit of `+f6` tally is MeV/g. For convenience, the mass of the tally cell 3 is set to 1 g using the

2567 segment divisor (`sd`) card. Then, the magnitude of the `+f6` tally gives the history-averaged
2568 deposited energy in MeV.

2569 **Source Card**

2570 Neutrons (`par=n`) with 1-MeV energy (`erg=1`) are born at position $(-6, 0, 0)$ cm and travel
2571 along the x axis, i.e., the cosine value with respect to the reference vector $(1, 0, 0)$ is one
2572 (`dir=1`). One thousand such neutrons are simulated (`nps 1000`), and table 110 is printed to
2573 verify the source sampling.

2574 The computed deposited energy in paraffin wax is $0.917 \pm 1.94\%$, or between 0.899 to
2575 0.935, MeV per source neutron.

2576 **A.2 Geant4 Input**

2577 **A.2.1 Main Function**

2578 Inputs of the Geant4 application for the example problem consist of customized C++ classes
2579 coordinated by a main function, which is shown in Listing [A.1](#). In the included headers,
2580 `globals.hh` contains the Geant4-derived basic data types, e.g., `G4double` and `G4int`, to
2581 replace the standard C++ counterparts, e.g., `double` and `int`, which ensures value-range
2582 consistency for different compilers and platforms. `G4SystemOfUnits` defines the units.

2583 In the function body, an instance of the `G4MTRunManager` class is initialized, which is
2584 used in a multi-thread run. The number of cores to run the simulation is set to the available
2585 cores on the node. Instances of the `DetectorConstruction`, `ActionInitialization`, and
2586 `QGSP BERT HP` reference physics list classes are registered to run manager. The singleton
2587 object of the `G4UImanager` class reads the macro commands from the command-line file. In
2588 the end, the memory of the run manager class instance is freed, which implicitly deletes the
2589 registered class objects.

Listing A.1: main.cc

```

#include "globals.hh"
#include "G4SystemOfUnits.hh"
#include "G4MTRunManager.hh"
#include "DetectorConstruction.hh"
#include "QGSP_BERT_HP.hh"
#include "ActionInitialization.hh"
#include "G4UImanager.hh"
int main(int argc, char** argv)
{ // initialize multi-thread run manager
  G4MTRunManager* runManager = new G4MTRunManager();
  runManager -> SetNumberOfThreads(G4Threading::G4GetNumberOfCores());
  // register detector construction, physics list, and action
  // initialization
  runManager -> SetUserInitialization(new DetectorConstruction());
  runManager -> SetUserInitialization(new QGSP_BERT_HP());
  runManager -> SetUserInitialization(new ActionInitialization());
  // UI manager
  G4UImanager* UImanager = G4UImanager::GetUIpointer();
  // batch mode + macro file
  G4String command = "/control/execute ";
  G4String fileName = argv[1];
  UImanager -> ApplyCommand(command + fileName);
  // run manager frees the memory for the registered classes
  if (runManager)
    delete runManager;
  return 0;}

```

2590 A.2.2 Detector Construction

2591 The `DetectorConstruction` class is defined in Listing [A.2](#) and Listing [A.3](#). This class
 2592 inherits the `Construct` function from the `G4VUserDetectorConstruction` base class to pass
 2593 the defined materials and geometry of the model into Geant4 kernel. Dry air and paraffin
 2594 wax have been predefined in the internal material database, `G4NistManager`.

2595 The world and the paraffin tank are defined in the same way. A Geant4 box solid is first
 2596 defined with four parameters, which are name and half lengths in xyz axes. The solid is

2597 filled with material to construct the logical volume. The logical volume is placed into the
2598 tracking geometry via the physical volume, definition of which contains rotation matrix and
2599 translation vector with respect to the mother logical volume. No rotation and coordinate
2600 translation is needed for this model. The world physical volume has no mother volume,
2601 and, thus, a null pointer is entered. The world physical volume is returned to complete the
2602 construct.

Listing A.2: DetectorConstruction.hh

```
#ifndef DetectorConstruction_h
#define DetectorConstruction_h 1
#include "globals.hh"
#include "G4SystemOfUnits.hh"
#include "G4VUserDetectorConstruction.hh"
#include "G4NistManager.hh"
#include "G4Material.hh"
#include "G4Box.hh"
#include "G4LogicalVolume.hh"
#include "G4VPhysicalVolume.hh"
#include "G4PVPlacement.hh"
class DetectorConstruction : public G4VUserDetectorConstruction
{public:
    DetectorConstruction();
    virtual ~DetectorConstruction();
    G4VPhysicalVolume* Construct();
};
#endif
```

2603 **A.2.3 Action Initialization**

2604 Shown in Listing [A.4](#) and Listing [A.5](#) is the definition of the `ActionInitialization` class,
2605 which inherits the `G4VUserActionInitialization` class. In the `BuildForMaster` function,
2606 which is only called by the master thread, an instance of the self-developed `Runaction`
2607 class is initialized, which collects tallies from the local `RunAction` class objects. In the
2608 `Build` function, which is called by all the working threads, instances of the mandatory

Listing A.3: DetectorConstruction.cc

```

#include "DetectorConstruction.hh"
DetectorConstruction::DetectorConstruction()
:G4VUserDetectorConstruction() {}
DetectorConstruction::~~DetectorConstruction() {}
G4VPhysicalVolume* DetectorConstruction::Construct()
{ // internal material database
  G4NistManager* nist = G4NistManager::Instance();
  G4Material* air = nist -> FindOrBuildMaterial("G4_AIR");
  G4Material* wax = nist -> FindOrBuildMaterial("G4_PARAFFIN");
  G4double len = 10.0 * cm;
  // cubic world solid, half lengths in xyz axes are specified
  G4Box* world_solid = new G4Box("world_solid", len, len, len);
  G4LogicalVolume* world_lv = new G4LogicalVolume(world_solid, air,
"world_lv"); // logical volume consists of solid and material
  G4VPhysicalVolume* world_pv = new G4PVPlacement(
0, // rotation matrix
G4ThreeVector(), // translation vector
world_lv, // logical volume
"world_pv", // physical volume name
0, // mother logical volume
false, // future use
0, // copy number
true); // surface check
  // cubic tank solid, half lengths are specified
  G4Box* tank_solid = new G4Box("tank_box", len*0.5, len*0.5, len*0.5);
  G4LogicalVolume* tank_lv = new G4LogicalVolume(tank_solid,
wax, "tank_lv");
  G4VPhysicalVolume* tank_pv = new G4PVPlacement(
0, // rotation matrix
G4ThreeVector(), // translation vector
tank_lv, // logical volume
"tank_pv", // physical volume name
world_lv, // mother logical volume
false, // future use
0, // copy number
true); // surface check
  return world_pv;}

```

2609 `PrimaryGeneratorAction` and three optional user action classes are initialized, which are
2610 `RunAction`, `EventAction` and `SteppingAction`. The `PrimaryGeneratorAction` class de-
2611 fines source particles. The user action classes are linked to accumulate tally, which was used
2612 in the neutron detector models. Other tally methods are also provided, e.g., multi-functional
2613 detector, primitive scorer, and command-based scoring [60].

Listing A.4: `ActionInitialization.hh`

```
#ifndef ActionInitialization_h
#define ActionInitialization_h 1
#include "G4VUserActionInitialization.hh"
#include "PrimaryGeneratorAction.hh"
#include "RunAction.hh"
#include "EventAction.hh"
#include "SteppingAction.hh"
class ActionInitialization : public G4VUserActionInitialization
{ public:
    ActionInitialization();
    virtual ~ActionInitialization();
    virtual void BuildForMaster() const;
    virtual void Build() const;
};
#endif
```

2614 **Primary Generation**

2615 Shown in Listing A.6 and Listing A.7 is the `PrimaryGeneratorAction` class to define source
2616 particles via the `G4GeneralParticleSource` (GPS) class. The GPS class provides a rela-
2617 tively comprehensive macro commands to avoid hard coding.

2618 The macro commands are listed in a macro file, as shown in Listing A.8. This macro file
2619 is read by the executable via command line, as indicated in Listing A.1.

Listing A.5: ActionInitialization.cc

```
#include "ActionInitialization.hh"
ActionInitialization::ActionInitialization():G4VUserActionInitialization()
{}
ActionInitialization::~~ActionInitialization()
{}
void ActionInitialization::BuildForMaster() const
{ RunAction* runAction = new RunAction();
  SetUserAction(runAction);}
void ActionInitialization::Build() const
{ SetUserAction(new PrimaryGeneratorAction());
  RunAction* runAction = new RunAction();
  SetUserAction(runAction);
  EventAction* eact = new EventAction(runAction);
  SetUserAction(eact);
  SteppingAction* sact = new SteppingAction(eact);
  SetUserAction(sact);}
```

Listing A.6: PrimaryGeneratorAction.hh

```
#ifndef PrimaryGeneratorAction_h
#define PrimaryGeneratorAction_h 1
#include "G4VUserPrimaryGeneratorAction.hh"
#include "G4GeneralParticleSource.hh"
class PrimaryGeneratorAction : public G4VUserPrimaryGeneratorAction
{public:
  PrimaryGeneratorAction();
  virtual ~PrimaryGeneratorAction();
  virtual void GeneratePrimaries(G4Event*);
private:
  G4GeneralParticleSource* generator;};
#endif
```

2620 Run Action

2621 Shown in Listing [A.9](#) and Listing [A.10](#) is the customized RunAction class. The variables
 2622 `rerg` and `rerg2` accumulate tally and tally square from events, respectively, to compute the

Listing A.7: PrimaryGeneratorAction.cc

```
#include "PrimaryGeneratorAction.hh"
PrimaryGeneratorAction::PrimaryGeneratorAction() :
G4VUserPrimaryGeneratorAction()
{ generator = new G4GeneralParticleSource();}
PrimaryGeneratorAction::~~PrimaryGeneratorAction()
{if (generator)
    delete generator;}
void PrimaryGeneratorAction::GeneratePrimaries(G4Event* anEvent)
{ generator -> GeneratePrimaryVertex(anEvent);}
```

Listing A.8: Macro file

```
# Initialize kernel
/run/initialize
# verbose setting
/control/verbose 0
/run/verbose 0
/event/verbose 0
/tracking/verbose 0
# GPS definition
# neutron
/gps/particle neutron
# position sampling
/gps/pos/centre -6 0 0 cm
# direction sampling
/gps/direction 1 0 0
/gps/ene/mono 1 MeV
/run/beamOn 1000
```

2623 average and variance. The type of these variables instantiates the `G4Accumulable` template
2624 class using the `G4double` type, and, hence, the master instance of the run action class can
2625 merge tallies from local threads. The `add_event_energy` function is called at the end of
2626 each event to accumulate the event-specific tallies (shown in Listing [A.12](#)), and the `cal_ave`
2627 function computes the average and relative error. The computed results are printed at the
2628 end of the run by the master thread.

Listing A.9: Runaction.hh

```
#ifndef RunAction_h
#define RunAction_h 1
#include "G4UserRunAction.hh"
#include "globals.hh"
#include "G4SystemOfUnits.hh"
// global run action accumulates tally from local run actions
#include "G4AccumulableManager.hh"
#include "G4Accumulable.hh"
#include "G4Run.hh"
#include <cmath>
typedef std::vector<G4double> vec_double;
class RunAction : public G4UserRunAction
{public:
    RunAction();
    virtual ~RunAction();
    void BeginOfRunAction(const G4Run*);
    void EndOfRunAction(const G4Run*);
    vec_double cal_ave(G4double, G4double, G4int);
    void add_event_energy(G4double);
private:
    G4Accumulable<G4double> rerg;
    G4Accumulable<G4double> rerg2;};
#endif
```

2629 **Event Action**

2630 The `EventAction` class is shown in Listing [A.11](#) and Listing [A.12](#). It has a data member,
2631 `event_erg`, to accumulate tally from steps via the `add_step_energy` function. At the begin-
2632 ning of an event, this variable is set to zero, and at the end of an event, non-zero event tally
2633 is accumulated via the `add_event_energy` function in the run action.

2634 **Step Action**

2635 Shown in Listing [A.13](#) and Listing [A.14](#) is the `SteppingAction` class. The `UserSteppingAction`
2636 function is called at the end of every Monte Carlo step to extract the tally. Each step has

Listing A.10: Runaction.cc

```

#include "RunAction.hh"
RunAction::RunAction() : G4UserRunAction(), rerg(0.0), rerg2(0.0){
    // register accumulable
    auto accumulableManager = G4AccumulableManager::Instance();
    accumulableManager -> RegisterAccumulable(rerg);
    accumulableManager -> RegisterAccumulable(rg2);}
RunAction::~RunAction() {}
void RunAction::BeginOfRunAction(const G4Run* run) {}
void RunAction::EndOfRunAction(const G4Run* run) {
    // merge accumulables
    auto accumulableManager = G4AccumulableManager::Instance();
    accumulableManager -> Merge();
    // get value
    G4double verg = rerg.GetValue();
    G4double verg2 = rerg2.GetValue();
    // Print
    if (IsMaster()){
        G4cout << "\n-----End of Global Run-----\n";
        G4int nofEvents = run -> GetNumberOfEvent();
        vec_double ans = cal_ave(verg, verg2, nofEvents);
        G4cout << "Ave. total deposited energy in tank, relative error = "
        << ans[0] / MeV << " MeV, " << ans[1] << G4endl;}}
vec_double RunAction::cal_ave(G4double var, G4double var2, G4int n){
    vec_double ans(2);
    G4double ave = var / n, ave2 = var2 / n;
    ans[0] = ave;
    G4double std_dev = sqrt((ave2 - ave * ave) / (n - 1));
    if (fabs(ave) < 1.0e-20)
        // if no tally, set the relative error to 1
        ans[1] = 1.0;
    else
        ans[1] = std_dev / ave;
    return ans;}
void RunAction::add_event_energy(G4double eerg){
    rerg += eerg;
    rerg2 += eerg * eerg;}

```

Listing A.11: EventAction.hh

```

#ifndef INCLUDE_EVENTACTION_HH_
#define INCLUDE_EVENTACTION_HH_
#include "G4UserEventAction.hh"
#include "globals.hh"
#include "RunAction.hh"
class EventAction : public G4UserEventAction
{public:
    EventAction(RunAction*);
    ~EventAction();
    void BeginOfEventAction(const G4Event*);
    void EndOfEventAction(const G4Event*);
    void add_step_energy(G4double);
private:
    G4double event_erg;
    RunAction* ract;};
#endif

```

Listing A.12: EventAction.cc

```

#include "EventAction.hh"
EventAction::EventAction(RunAction* tmp)
: G4UserEventAction() {ract = tmp;}
EventAction::~~EventAction() {}
void EventAction::add_step_energy(G4double input) {event_erg += input;}
void EventAction::BeginOfEventAction(const G4Event* anEvent)
{ event_erg = 0.0;}
void EventAction::EndOfEventAction(const G4Event* anEvent){
    if (erg > 1.0e-20)
        ract -> add_event_energy(event_erg);}

```

2637 pre- and post-step points. The steps with pre-step points inside the wax tank (the tally
2638 region) are selected, and the total deposited energy in these steps are accumulated to the
2639 event tally using the `add_step_energy` function defined in Listing [A.12](#).

2640 The Geant4 executable was compiled using the `cmake` utility. The calculated deposited
2641 energy in the paraffin tank is $0.938 \pm 1.20\%$, or between 0.927 to 0.949, MeV, which overlaps

Listing A.13: SteppingAction.hh

```
#ifndef INCLUDE_STEPPINGACTION_HH_
#define INCLUDE_STEPPINGACTION_HH_
#include "EventAction.hh"
#include "G4UserSteppingAction.hh"
#include "G4Step.hh"
#include "G4StepPoint.hh"
#include "globals.hh"
class SteppingAction : public G4UserSteppingAction
{public:
    SteppingAction(EventAction*);
    virtual ~SteppingAction();
    void UserSteppingAction(const G4Step*);
private:
    EventAction* eact;};
#endif
```

2642 with the MCNP result of between 0.899 to 0.935 MeV.

Listing A.14: SteppingAction.cc

```

#include "SteppingAction.hh"
SteppingAction::SteppingAction(EventAction* tmp)
:G4UserSteppingAction()
{ eact = tmp;}
SteppingAction::~~SteppingAction() {}
void SteppingAction::UserSteppingAction(const G4Step* astep)
{ // get step point
  G4StepPoint* pre_point = astep -> GetPreStepPoint();
  G4StepPoint* post_point = astep -> GetPostStepPoint();
  // get physical volume
  G4VPhysicalVolume* pre_pv = pre_point -> GetPhysicalVolume();
  G4VPhysicalVolume* post_pv = post_point -> GetPhysicalVolume();
  // get physical volume name
  G4String pre_name = "";
  G4String post_name = "";
  if (post_pv){
    pre_name = pre_pv -> GetName();
    post_name = post_pv -> GetName();
  }
  else
    return;
  // accumulate the deposited energy in the tank
  if (pre_name == "tank_pv"){
    G4double step_erg = astep -> GetTotalEnergyDeposit();
    if (step_erg > 1.0e-20)
      eact -> add_step_energy(step_erg);
  }
}}

```

2643 Appendix B

2644 ElmerSolver Input

2645 Shown below is a template ElmerSolver input written in a text `sif` file to calculate the
2646 electric field inside the MPFD gas volums. Much of the contents are based on an official
2647 Garfield++ example [76]. While the inputs are self-explained, several notes are followed.

2648 Check Keywords Warn

2649 ! mesh and output folder

2650 Header

2651 Mesh DB "." "FOLDER"

2652 End

2653 ! Details of the calculation and output files.

2654 Simulation

2655 Coordinate System = Cartesian 3D

2656 Simulation Type = Steady State

2657 Steady State Max Iterations = 1

2658 Output File = "FILE.result"

2659 Post File = "FILE.ep"

2660 End

2661 ! Define constants.

2662 Constants

```

2663     Permittivity Of Vacuum = 8.8542e-12
2664 End
2665 ! Specify equation and material for gas.
2666 Body 1
2667     Equation = 1
2668     Material = 1
2669 End
2670 ! Define the ar gas
2671 Material 1
2672     Relative Permittivity = 1.000516
2673 End
2674 ! west wire
2675 Boundary Condition 1
2676     Target Boundaries = 1
2677     Potential = 100
2678 End
2679 ! east wire
2680 Boundary Condition 2
2681     Target Boundaries = 2
2682     Potential = 0
2683 End
2684 ! Details of the calculation procedure
2685 Equation 1
2686     Active Solvers(1) = 1
2687     Calculate Electric Energy = True
2688 End
2689 Solver 1
2690     Equation = Stat Elec Solver
2691     Variable = Potential

```

```
2692     Variable DOFs = 1
2693     Procedure = "StatElecSolve" "StatElecSolver"
2694     Calculate Electric Field = True
2695     Calculate Electric Flux = False
2696     Linear System Solver = Iterative
2697     Linear System Iterative Method = BiCGStab
2698     Linear System Max Iterations = 1000
2699     Linear System Abort Not Converged = True
2700     Linear System Convergence Tolerance = 1.0e-10
2701     Linear System Preconditioning = ILU1
2702     Steady State Convergence Tolerance = 5.0e-7
2703 End
```

2704 In the Header section, the folder with name `FOLDER` at current path that contains the
2705 `ElmerGrid` output files is specified. The `ElmerSolver` output `result` file is put into the
2706 same folder.

2707 `Body 1` is the physical gas volume defined in `Gmsh`. The governing equation 1 and
2708 material 1 (argon gas) are applied to this `body`. The governing equation and material are
2709 defined in the corresponding sections. The electrostatics solver for the governing equation is
2710 specified in the `Solver` section.

2711 The applied voltages at the electrodes are specified in the boundary condition sections.
2712 The `Target Boundaries` keyword specifies the re-numbered physical surface identification
2713 number to which the boundary condition should apply. The `Potential` keyword specifies
2714 the applied voltage, i.e., 100-V voltage on anode and grounded cathode.

2715 Appendix C

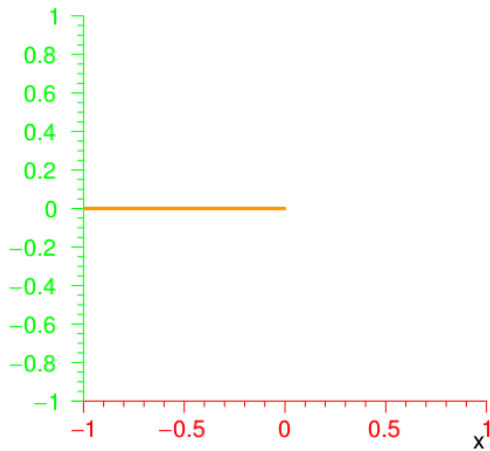
2716 Electron Tracking in Parallel Plate

2717 To examine the electron tracking simulation in Garfield++, a parallel-plate example was
2718 developed. A $2 \times 100 \times 100$ cm³ box filled with argon gas at 1-atm pressure and 20 °C
2719 was modeled. A 100 V/cm constant electric field was applied in the gas volume along the
2720 positive x direction. A 0.5 V/cm weighting electric field along the positive x direction was
2721 set. Electrons were born at the center of the box. The Monte Carlo and the microscopic
2722 tracking algorithms were used to simulate the electron motion.

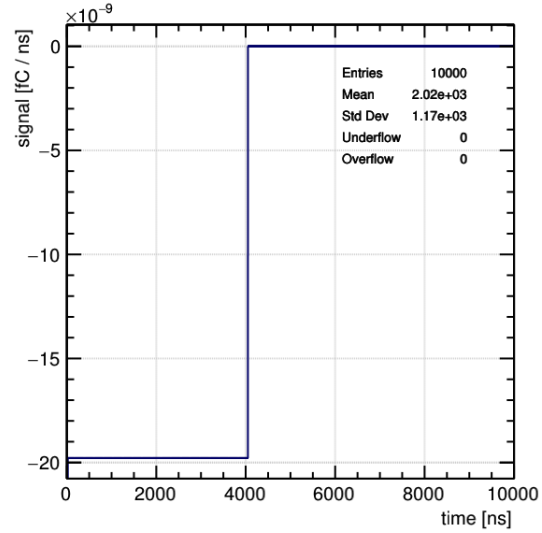
2723 The electron trajectory and the induced current simulated by the Monte Carlo integra-
2724 tion method are shown in Fig. C.1. The diffusion process was not considered. Under such
2725 conditions, the electron travels along the x axis and traverses the 1-cm distance in approxi-
2726 mately 4 μ s. Thus, the electron drift velocity is about 0.25 cm/ μ s. It was reported that the
2727 mean drift speed for electrons in pure argon gas under an electric field \mathbf{E} and gas pressure
2728 P can be approximated by [10]

$$v_e = \frac{3.64(\mathbf{E}/P) + 114.6(\mathbf{E}/P)^2}{1 + 12.7(\mathbf{E}/P) + 304.33(\mathbf{E}/P)^2} = 0.36 \text{ cm}/\mu\text{s} \quad (\text{C.1})$$

2729 for 100 V/s electric field and 1 atm (760 Torr) pressure. The difference may due to the facts
2730 that the mobility used in the Monte Carlo integration method was from a coarse electron
2731 transport table, and Eq. (C.1) is an approximation of the mean value. In the future work,
2732 the reason for this difference needs to be investigated.



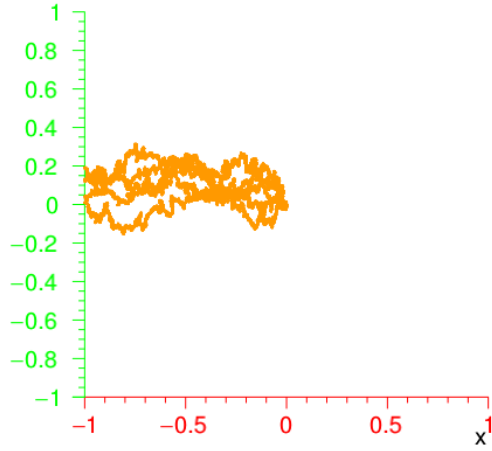
(a) Drift line.



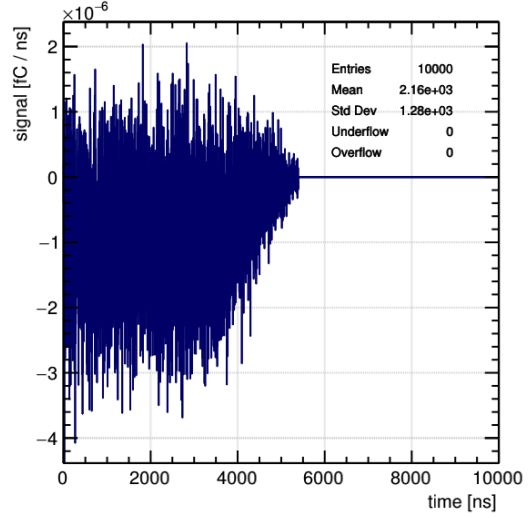
(b) Induced current.

Figure C.1: Drift line and induced current of one electron simulated by the Monte Carlo integration method. Diffusion was not simulated.

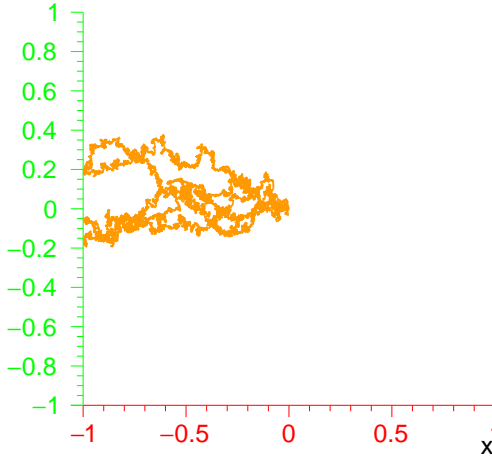
2733 To illustrate the effects of diffusion, the trajectories of five electrons and the induced
 2734 current by tracking 50 electrons were simulated using the Monte Carlo integration and the
 2735 microscopic tracking methods, and the results are shown in Fig. C.2. The results of these two
 2736 methods are similar. The trajectories are much more random, and as a result, the induced
 2737 current fluctuates.



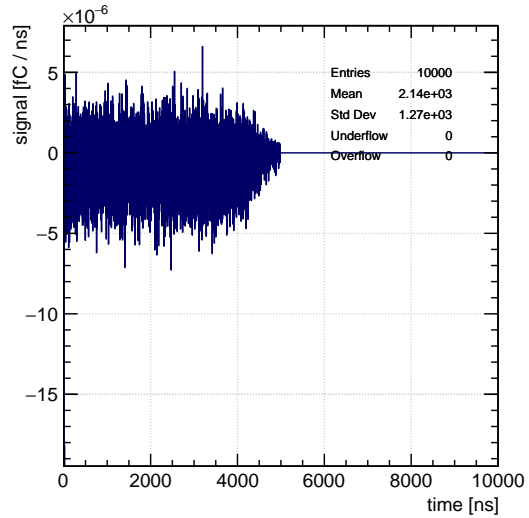
(a) Trajectories, Monte Carlo.



(b) Induced current, Monte Carlo.



(c) Trajectories, microscopic.



(d) Induced current, microscopic.

Figure C.2: Trajectories of five electrons (a) and induced current of 50 electrons (b) simulated by the Monte Carlo integration method taking into consideration of the diffusion process. Using the microscopic tracking method, the trajectories of five electrons (c) and induced current by 50 electrons (d) are similar with the Monte Carlo integration results.